

e-ISSN: 2148-4171

11 3 2024
volume issue june

HITTITE JOURNAL OF SCIENCE AND ENGINEERING



HİTİT
ÜNİVERSİTESİ
YAYINLARI

HITTITE JOURNAL OF SCIENCE AND ENGINEERING

e-ISSN: 2148-4171

Volume: 11

June 2024

Issue 3

OWNER ON BEHALF OF HITIT UNIVERSITY

Prof. Dr. Ali Osman ÖZTÜRK
Rector of Hitit University

RESPONSIBLE MANAGER

Dr. Hüseyin Taha TOPALOĞLU
Hitit University

EDITOR-IN-CHIEF

Prof. Dr. Ali KILIÇARSLAN
Hitit University

ASSOCIATE EDITORS

Prof. Dr. Dursun Ali KÖSE
Hitit University

Assoc. Prof. Dr. Öncü AKYILDIZ
Hitit University

LANGUAGE OF PUBLICATION

English

CONTACT ADDRESS

Hitit Üniversitesi Mühendislik Fakültesi, ÇORUM, TÜRKİYE
Tel: 0090 364 2274533 Fax: 0090 364 2274533
hjse@hitit.edu.tr | <https://www.hjse.hitit.edu.tr>

PUBLISHER

Hitit University Press

EDITOR-IN-CHIEF

Ali KILIÇARSLAN, Prof. Dr.
Hitit University, TR

ASSOCIATE EDITORS

Dursun Ali KÖSE, Prof. Dr.
Hitit University, TR

Öncü AKYILDIZ, Assoc. Prof. Dr.
Hitit University, TR

SECTION EDITORS

Murat HOŞÖZ, Prof. Dr.
Kocaeli University, TR

Dursun Ali KÖSE, Prof. Dr.
Hitit University, TR

Kazım Savaş BAHÇECİ, Prof. Dr.
Hitit University, TR

Cengiz BAYKASOĞLU, Prof. Dr.
Hitit University, TR

Akif AKGÜL, Prof. Dr.
Hitit University, TR

Öncü AKYILDIZ, Assoc. Prof. Dr.
Hitit University, TR

BOARD OF EDITORS

Iftikhar AHMAD, Prof. Dr.
University of Malakand, PK

Mike BECKETT, Prof. Dr.
Bangor University, UK

İbrahim DİNÇER, Prof. Dr.
University of Ontario Institute of
Technology, CA

Ali El KAMEL, Prof. Dr.
University of Waterloo, CA

Mohamad S QATU, Prof. Dr.
Eastern Michigan University, USA

Saffa RIFFAT, Prof. Dr.
University of Nottingham, UK

Thanos SALIFOĞLU, Prof. Dr.
Aristotle University of Thessaloniki, GR

Yuehong SU, Prof. Dr.
University of Nottingham, UK

Wojciech NOGALA, Dr.
Polish Academy of Sciences, POL

Metin GÜRÜ, Prof. Dr.
Gazi University, TR

Murat HOŞÖZ, Prof. Dr.
Kocaeli University, TR

Sadık KAKAÇ, Prof. Dr.
TOBB University of Economics and
Technology, TR

Tarık Ömer OĞURTANI, Prof. Dr.
Middle East Technical University, TR

Ender SUVACI, Prof. Dr.
Eskişehir Technical University, TR

Ali TOPÇU, Prof. Dr.
Hacettepe University, TR

Kazım Savaş BAHÇECİ, Prof. Dr.
Hitit University, TR

Cengiz BAYKASOĞLU, Prof. Dr.
Hitit University, TR

Vedat DENİZ, Prof. Dr.
Hitit University, TR

Bülent KABAK, Prof. Dr.
Hitit University, TR

Ali KILIÇARSLAN, Prof. Dr.
Hitit University, TR

İrfan KURTBAŞ, Prof. Dr.
Hitit University, TR

İbrahim SÖNMEZ, Prof. Dr.
Hitit University, TR

Seyfi ŞEVİK, Assoc. Prof. Dr.
Hitit University, TR

REFeree BOARD

Hittite Journal of Science and Engineering uses a single-blind review. Referee names are kept strictly confidential.

Layout Editors

Ömer Faruk TOZLU, Res. Asst.
Hitit University, TR

Harun Emre KIRAN, Res. Asst.
Hitit University, TR

Hayati TÖRE, Res. Asst.
Hitit University, TR

LOCKSS: <http://dergipark.org.tr/hjse/lockss-manifest>

OAI: https://dergipark.org.tr/api/public/oai/hjse/?verb=ListRecords&metadataPrefix=oai_dc

Dear Readers,

Summer ended, fall comes and hardworking time starts again for students, researchers and academicians. As the Editor-in-Chief, I hope that people studying in the education and research will have a full of successful time in the semesters of fall and winter in 2024. With this new issue of Hittite journal of Science and Engineering (HJSE) (2024 - Volume: 11 issue:3) I would like to express my gratitude to the president of Hitit University for his support, the associate editors, section editors, reviewers, Hitit University Publishing Office and Production Team of HJSE for their devoted efforts and sacrifices. We have a good news from our sister journal, Hitit Journal of Science, it has published the first issue. I would like also thank for the previous members of editorial board members, some of them are now placed in the Editorial Board of Hitit Journal of Science.

In the new issue of HJSE, we published five original papers from five disciplines of engineering, namely biomedical, geological, geomatics, mechanical and chemical engineering. The paper from biomedical engineering is mainly based on a novel computer-assisted sperm analysis (CASA) system designed to evaluate sperm motility through digital micrographs, utilizing 14 distinct kinematic parameters. The second paper from geological engineering deals with the structures showing tectonic lineaments (fault, fracture, fold axis) observed in the Eocene-aged units in Demirci (Aksaray, Türkiye) and its vicinity with the satellite-based lineaments. The work from geomatics engineering is related to the derivation of an up-to-date high-spatial-resolution Global Navigation Satellite Systems (GNSS) velocity field for the central NAFZ and to correlate with the strain accumulations along the faults. As for the article in mechanical engineering, by using finite element method, the effects of the defect presence, defect volume fraction, defect position, and random distribution of defects at the adhesive layer on the durability of the butt joint was investigated. In the last paper (from the discipline of chemical engineering), various properties of the activated carbons produced using various characterization methods, such as surface porosity, were investigated. I hope that the researchers studying in the mentioned disciplines will benefit from these papers.

It is my pleasure to invite the researchers and scientists from all branches of engineering to join us by sending their best papers for publication in Hittite Journal of Science and Engineering.

Dr. Ali Kılıçarslan
Editor-in-Chief

CONTENTS

From Editor

Research Articles

Synthesis and Characterization of Porous Materials from Waste Wheat Bran

Canan Şamdan, İlkur Demiral, Fatma Betül Kuş..... 95

Investigation of the Defect Effects on the Durability of the Butt Joints: A Numerical Study

Hamza Taş 105

Geodetic Studies on Active Faults in and surroundings of Çorum: Initial Results

Mehmet Nurullah Alkan, Kayhan Aladoğan, İbrahim Tiryakioğlu, Hasan Hakan Yavaşoğlu, Halil İbrahim Solak, Cemil Gezgin, Ali Özkan, Eda Esmâ Eyübagil, Furkan Şahiner, Ece Bengünaz Çakanşimşek, Zafer Köse 115

Comparison of Geological Structures and Satellite-Based Tectonic Lineaments in Gulagac (Aksaray) and Its Surroundings

Ramazan Demircioğlu 123

Assessment of human sperm kinematic parameters using computer-assisted semen analysis

Hüseyin Kurtuldu 131

HITTITE JOURNAL OF SCIENCE AND ENGINEERING

e-ISSN: 2148-4171
Volume: 11 • Number: 3
September 2024

Synthesis and Characterization of Porous Materials from Waste Wheat Bran

Ilknur Demiral  | Canan Samdan*  | Fatma Betül Kus 

Eskişehir Osmangazi University, Faculty of Engineering and Architecture, Department of Chemical Engineering, 26480 Eskişehir, Türkiye.

Corresponding Author

Canan Samdan

E-mail: caydin@ogu.edu.tr Phone: +90222 239 37 50-3664 Fax: +90222 239 36 13

RORID: <https://ror.org/01dzjez04>

Article Information

Article Type: Research Article

Doi: <https://doi.org/10.17350/HJSE19030000336>

Received: 08.12.2023

Accepted: 13.06.2024

Published: 30.09.2024

Cite As

Demiral I, et al. Synthesis and Characterization of Porous Materials from Waste Wheat Bran. Hittite J Sci Eng. 2024;11(3):95-104.

Peer Review: Evaluated by independent reviewers working in at least two different institutions appointed by the field editor.

Ethical Statement: Not available.

Plagiarism Checks: Yes - iThenticate

Conflict of Interest: Authors declare no conflict of interest.

CRedit AUTHOR STATEMENT

Ilknur Demiral: Conceptualization, Data curation, Formal Analysis, Investigation, Methodology, Resources, Supervision, Writing – review and editing. **Canan Samdan:** Conceptualization, Data curation, Formal Analysis, Investigation, Methodology, Supervision, Visualization, Writing – original draft & editing. **Fatma Betül Kus:** Conceptualization, Data Curation, Formal Analysis, Methodology, Validation, Writing.

Copyright & License: Authors publishing with the journal retain the copyright of their work licensed under CC BY-NC 4.

Synthesis and Characterization of Porous Materials from Waste Wheat Bran

Ilknur Demiral | Canan Samdanı | Fatma Betül Kus

Eskişehir Osmangazi University, Faculty of Engineering and Architecture, Department of Chemical Engineering, 26480 Eskişehir, Türkiye.

Abstract

The purpose of this study was to investigate how the amount of $ZnCl_2$ and temperature affect the process of converting waste wheat bran, known for its hemicellulose structure, into porous material. The characterization of the wheat bran was done using proximate and primary component analysis, and Thermogravimetric analysis (TG) test, Fourier Transform Infrared Spectroscopy (FT-IR) spectra, Energy-dispersive X-ray spectroscopy (EDS) results, and Scanning electron microscopy (SEM) images. The influence of temperature on the surface areas of activated carbons is more significant than the impact of varying the amount of $ZnCl_2$. When the carbonization temperature reached 500 °C, porous structures developed, and the highest surface areas achieved for all impregnation ratios (1:1, 2:1, and 3:1) were 1234, 1478, and 1422 m^2/g , respectively. Activated carbon was found to have acidic (0.88 mmol/g) and basic (0.54 mmol/g) functional groups on its surface, after being synthesized through carbonization at 500 °C using $ZnCl_2$ at a 2:1 impregnation ratio in accordance with Boehm titration. This promising activated carbon made from wheat bran, activated by $ZnCl_2$, is efficient and environmentally friendly, and it is a potential solution for water pollution treatment.

Keywords: Activated carbon, surface characterization, biomass (wheat bran), chemical activation, characterization

INTRODUCTION

Activated carbon is a porous material obtained by increasing the carbon content of various materials such as wood, coal, polymer, and biomass at high temperatures through different activation processes. Activated carbons contain hydrogen, nitrogen, sulfur, and oxygen in their internal structure and functional groups attached to their external surfaces. The quality of porous material varies depending on the raw material and synthesis method used (Daoud et al. 2019; Azam et al. 2022). The traditional synthesis of activated carbon consists of two basic steps: carbonization and activation. Carbonization is a process that involves the thermal decomposition of volatile elements from the raw material in an environment without oxygen. This process leads to the removal of components other than carbon and results in the production of materials with a high carbon content. Essentially, cross-links in raw materials are broken down, and the volatile substance content is reduced. During carbonization, the lignocellulosic contents are broken down, which removes elements such as nitrogen, oxygen, and hydrogen (Mahmoud Amer and Ahmed Elwardany 2020).

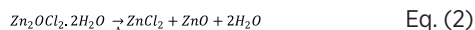
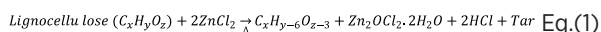
Chemical activation is a process that doesn't involve a different carbonization level. The completely dehydrated sample reacts by coming into contact with dehydrating agents such as NaOH, KOH, $ZnCl_2$ and H_3PO_4 (Reza et al. 2020). Activated carbon with well-developed porous areas can be produced in a single step, reducing the production of volatile matter during pyrolysis and minimizing particle shrinkage and damage to the raw material surface. This results in the production of activated carbon with high efficiency and carbon content (Świątkowski 1999). Biomass and waste materials can be used to produce activated carbon cost-effectively. These materials often have no economic value, and waste disposal poses a problem. Converting them into activated carbon can provide economic value but can also reduce the cost of waste disposal. The use of biomass as a raw material in the production of activated carbon can provide a cheap alternative to commercial activated carbons. Many materials, palm kernels, olive pits, waste sludge and tires, bamboo powder, coconut shells, rice husks and straw, jute fibers, zeolite, sugars, Chinese jujube seeds, wood shavings, tropical trees, palm shells, corn cobs, walnut shells, tobacco stalks, bean pods, hazelnut shells, banana peels,

mangosteen shells are used in the production of activated carbon (Rafatullah et al. 2010; Tadda et al. 2016).

Wheat is a crucial crop globally, and its production reached 790198 tonnes in 2022. In Turkey, the 10th largest wheat producer, 15000 tonnes of wheat were planted (FAOSTAT 2024). Wheat bran, a by-product of wheat (approximately 25% by weight), amounts to around 3750 tons per year in Turkey and is a renewable biomass source. It is derived from wheat milling industries and is a readily available natural material, suitable for producing an effective adsorbent. For this reason, wheat bran has been seen as a suitable raw material for the production of activated carbon as an environmentally friendly and renewable resource and was chosen as the carbon source in this study. Zhang and his team utilized wheat bran as a renewable and less enduring source to create carbon electrodes in supercapacitors. According to their research, during the production of carbon via alkali activation, the NaOH/precursor bulk mass was at the 4 state, resulting in durable hexagon pores of carbon from wheat bran with a visible surface area of 2562 m^2/g (Zhang).

Koli et al., prepared activated carbons from wheat bran which were mixed with H_2SO_4 and carried out under a one-step chemical activation under N_2 flow at 773K for 2 h. The maximum Brunauer-Emmett-Teller (BET) surface area was found 757 m^2/g (Koli et al. 2024). Wang et al., reported on wheat bran activated carbon which impregnated with KOH (1:2) as activating agent under nitrogen gas flow rate of 60 cm^3/min in a horizontal tubular furnace at 800 °C for 1 h and had obtained a maximum BET surface area of 2189 m^2/g (Wang et al. 2015). Hu et al., prepared activated carbons from wheat bran by chemical activation with $ZnCl_2$, KOH and $ZnCl_2$ -KOH as activating agents in a reactor under argon flow. They report that two-step $ZnCl_2$ -KOH activation process was developed to produce wheat bran-derived biocarbon with an high specific surface area of 3200.8 m^2/g (Hu et al. 2024). Around 80% of activated carbons are utilized in liquid-phase applications and are recognized for their excellent performance in eliminating contaminants from different environments (Ioannidou and Zabaniotou 2007; Reza et al. 2020). When $ZnCl_2$ is used, it plays a crucial role as a dehydration agent during activation. Ma's report suggests that the production of ZnO may be explained by the following

equations (1) and (2) (Ma 2017):



At elevated temperatures, molten ZnCl₂ can facilitate dehydration processes that result in the breakdown of the polymer chains in lignocellulosic biomass, producing H₂O and a carbonaceous phase with thermoplastic properties (Kierzek and Gryglewicz 2020; Zhao et al. 2022). ZnCl₂ can then react with H₂O to create Zn₂OCl₂·2H₂O. Subsequently, the decomposition of Zn₂OCl₂·2H₂O can generate ZnCl₂ vapor. The presence of ZnCl₂ vapor and its diffusion can contribute to the development of the final porous carbon structure (Ma et al. 2009; Morali et al. 2018). Also, ZnCl₂ helps to inhibit the production of tar and facilitates the development of a high surface area and porous structure (Demiral and Gündüzoğlu 2010; Zhao et al. 2022). ZnCl₂ was chosen as the chemical activation agent in our study. In this study, activated carbons, which have a wide range of usage areas, were produced from wheat bran, which is a large mass of waste. Various properties of the activated carbons produced using various characterization methods, such as surface porosity, were investigated. Activated carbon is a material that is used as an important component in many industries. Our research, which explores the creation of a substance that can generate economic value from leftover wheat bran while also cutting waste disposal expenses, can serve as a valuable model in the literature.

MATERIALS AND METHOD

Devices and Chemicals

The raw material was ground using a Retsch SK-100 mill and then sieved into different particle sizes using an ISO 3310-1 sieve set. For the chemical activation of the raw material, zinc chloride (ZnCl₂) obtained from Merck was used. DAIHAN's SMH-6 Model heated magnetic stirrer was used for heating and mixing during the impregnation processes of the raw material. The carbonization process was carried out in a Carbolite TZF 12/75/700 tube furnace. The surface properties of the activated carbons obtained from wheat bran through the chemical activation method, using ZnCl₂, were measured by N₂ adsorption. The measurements were performed by changing the relative pressure (P/P₀) in the range of 10⁻⁶-1 at 77 K, using the Quantchrome Autosorb 1C device. FT-IR analysis of raw materials and activated carbons was carried out on the Perkin Elmer Spectrum device at Eskişehir Osmangazi University Central Research Laboratory Research and Application Center (ARUM). SEM photographs of the raw material were taken at Eskişehir Osmangazi University Central Research Laboratory Research and Application Center (ARUM) with a Hitachi Refulus 8230 FE-SEM brand device. A controlled temperature program (up to 1000 °C at a heating rate of 10 °C/min) was applied to wheat bran in a nitrogen atmosphere using the thermal analysis system (STA-TG/DTA), and the mass change was measured as a function of temperature. The amount of acidic-basic functional group was determined by Boehm titration method of the activated carbon produced at 500 °C at a 2:1 impregnation ratio.

Production of Activated Carbons

Activated carbon was produced using the chemical activation

method, wherein ZnCl₂ was selected as the chemical agent for impregnation. The impregnation ratios (IRs) of the chemical agent were determined as 1:1, 2:1, and 3:1, after which it was mixed with 20 g of wheat bran and refluxed in a heated magnetic stirrer at 80°C for 6 hours. Once the impregnation process was completed, the sample was filtered, and the water contained in the filtered product was completely removed from the structure by drying it in the oven. To produce activated carbon, wheat bran was treated with ZnCl₂ and subjected to simultaneous carbonization and activation processes. 10 g samples that had been impregnated with ZnCl₂ were placed in a reactor. The process was carried out for a duration of 1 hour in a vertical tube furnace at temperatures ranging from 400 to 600 °C, starting from laboratory temperature. The carbonization process was carried out in an inert environment, with nitrogen gas flowing at a rate of 100 ml/min. After cooling, the samples were weighed and washed in 0.5 M HCl solution, filtered, and then washed again with boiling distilled water having a pH value of 6-7. Finally, the washed samples were dried in an oven and weighed again. The activated carbons that were created were given names in the format of WB/temperature-/IR.

RESULTS AND DISCUSSION

Characterization of Wheat Bran

Wheat bran was characterized using proximate analysis results, structural components, physical properties, thermogravimetric analysis, FT-IR analysis, elemental analysis and SEM analysis results.

Proximate analysis of wheat bran

The results of moisture, volatile matter, ash, fixed carbon results of wheat bran are given in Table 1. Wheat bran's low ash content of 7.5% makes it a suitable material for producing activated carbon. Ghodrat et al.'s study investigated the in vitro binding capacity of manganese (Mn), zinc (Zn), copper (Cu), and iron (Fe) in wheat and barley. Their proximate analysis findings for wheat bran are similar to our own proximate analysis results. Ghodrat and colleagues found that wheat bran comprises 4.6 wt% ash, 9.55 wt% moisture, and 68.18 wt% volatile matter (Ghodrat et al. 2015). Ghodrat et al. stated that wheat bran can be a suitable source of raw materials for the production of activated carbon. In our study, we thought that wheat bran with wt 7.5% ash content could be a suitable carbon source.

Table 1 Proximate analysis of wheat bran

Proximate Analysis, %	
Moisture	9.6 (ASTM D 4442 - 92)
Ash	7.5 (ASTM D 1102 - 84)
Volatile matter	67.4 (ASTM E 897-82)
Fixed carbon*	15.5

*Bydifference

Results of thermogravimetric analysis of wheat bran

TGA is a thermal analysis technique that observes the mass change of a substance as it is exposed to controlled

temperature and atmospheric environments, either as a function of temperature or time (Escalante, 2022). The TGA graph in Figure 1 shows how organic compounds in wheat bran undergo thermal degradation. In the graph, the primary Y-axis shows the % mass loss observed in the sample based on the applied temperature (green line), the secondary Y-axis shows the differential of the mass loss over time (orange line), and the x-axis shows the temperature applied to the sample.

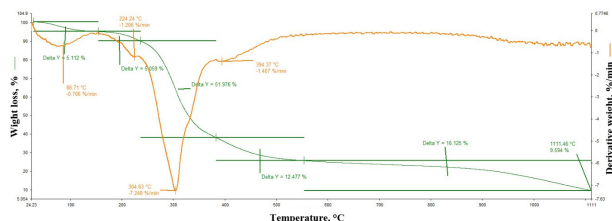


Figure 1 TGA-DTG curve representing the thermal decomposition of wheat bran

The TGA chart of wheat bran showed the first peak at 86.71°C, with a weight loss of 5.11%. This could be due to the evaporation of water present in the bran. The next weight loss occurred at 224.24°C, with a weight loss of 5.05%. This is because the hemicellulose present in bran begins to decompose at this temperature. According to a study by Li et al. (2021), the hemicellulose in the structure of wheat bran decomposes at 299°C. At 304.63°C, the wheat bran TGA plot shows a faster weight loss (51.97%) (Li et al. 2021). It is believed that this weight loss is due to the continued decomposition of hemicellulose, as well as the decomposition of cellulose. Cellulose decomposes at higher temperatures and is slower than hemicellulose. It can be inferred that the mass loss that continues from 394°C until 1111°C is due to the lignin present in the bran (Escalante et al. 2022). The TGA curve of wheat bran, which was studied by Pooladi et al., exhibits very similar characteristics to the TGA curve we acquired in our own research. Pooladi and colleagues noted in their research that the decomposition of wheat bran occurs in three distinct stages at temperature intervals of 50-180 °C, 200-800 °C, and 800-1000 °C like our study results (Pooladi et al. 2021) the uptake process of methylene blue (MB)

FT-IR analysis results of wheat bran

Infrared spectroscopy (IR) is a technique that relies on the vibrations of atoms in the chemical composition of materials. With FT-IR, researchers can detect the presence of many functional groups in commonly used materials such as adsorbents. For example, an adsorbent such as activated carbon may contain various functional groups such as carboxylic acids, quinones, phenolic groups, lactones, ketones, ethers, pyridine-like groups, amides, and amines (Kabdaşlı et al. 2009; Shafeeyan et al. 2010; Pellenz et al. 2023) application of electrocoagulation using common electrode materials (aluminum and stainless steel). The FT-IR image of wheat bran is shown in Figure 2.

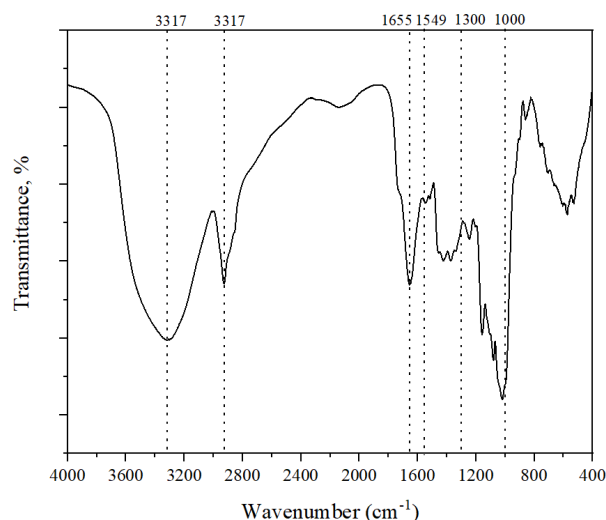


Figure 2 FT-IR image of wheat bran

FT-IR spectroscopy provides detailed information about the chemical bonds of organic components in wheat bran. According to the analysis results, hydroxyl groups, methyl and methylene groups, carboxylic acid groups, aldehyde or ketone groups, aromatic ring vibrations, vibrations of hydroxyl groups of cellulose, vibrations of glycosidic bonds of cellulose were detected in the bran. The band at 3317 cm^{-1} indicates the presence of hydroxyl (-OH) groups (Fanning and Vannice 1993; Shafeeyan et al. 2011; Hoseinzadeh Hesas et al. 2013). The peak at 2924 cm^{-1} indicates the presence of methyl (-CH₃) and methylene (-CH₂-) groups (Shen et al. 2010; Kaouah et al. 2013). The peak at 1736 cm^{-1} indicates the presence of carboxylic acid (-C=O) groups (Jia et al. 2001; Gulnaz et al. 2006; Biniak et al. 2013; Barroso-Bogeat et al. 2014). The peak at 1655 cm^{-1} indicates the presence of aldehyde (R-CHO) or ketone (R-CO-R') (Cagniant et al. 1998; Boonamnuayvitaya et al. 2005; El-Hendawy 2006). The peak at 1549 cm^{-1} indicates the presence of aromatic ring (-C=C-) vibrations (Guo and Rockstraw 2007; Momcilovic et al. 2011). The peaks at 1000-1300 cm^{-1} are assigned to C=O stretching in acids, alcohols, phenols, ethers, and esters (Gurten et al. 2012; Xu et al. 2014). In a study by Silva et al., Fourier transform infrared (FTIR) analysis of wheat bran was performed. Similar to the results in our study, their analysis identified specific bond structures indicating the presence of aromatic and organic compounds such as hemicellulose and cellulose in wheat bran (Silva et al. 2022).

Results of elemental analysis of wheat bran

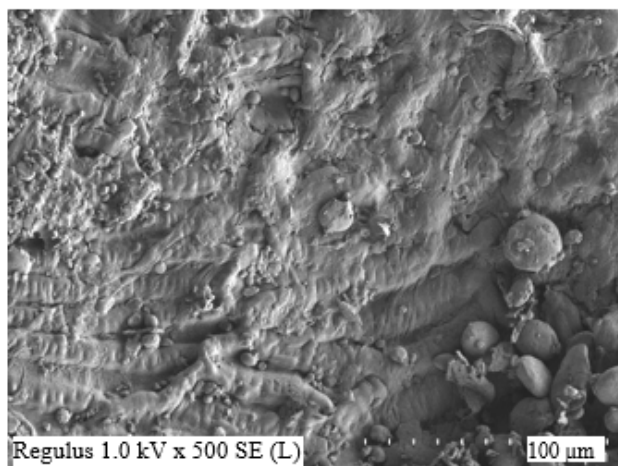
Table 2 shows the EDS analysis results of wheat bran. Based on these data, it appears that wheat bran has a high carbon content. The presence of nitrogen indicates that wheat bran contains nitrogenous compounds such as proteins, amino acids, and other organic compounds (Chaquilla-Quilca et al. 2016). A high percentage of oxygen indicates that wheat bran contains largely carbohydrates, oxygenated organic compounds such as cellulose and lignin (Chaquilla-Quilca et al. 2016).

Table 2 EDS analysis results of wheat bran

%C	%N	%O
52,61	3,79	43,59

SEM image of wheat bran

The SEM image of wheat bran is given in Figure 3. According to the images taken with the SEM device, raw wheat bran, which has not been subjected to any chemical/physical effects, has a non-porous structure (Figure 3). This shows that the raw material has a very small surface area before activation and carbonization.


Figure 3 SEM image of wheat bran

Activated Carbon Characterisation

The physical properties of activated carbons produced from wheat bran with $ZnCl_2$ at different IRs by mass and at different carbonization temperatures are given under this heading.

Physical properties of activated carbon

The properties of the surface pores of activated carbon vary depending on the ratio of chemicals used in the production process to the raw material and the temperature at which carbonization is carried out. This process reveals the carbonaceous structure and removes volatile components from it. We synthesized activated carbons under various conditions and have provided the properties of their porous

Table 3 Pore properties of carbonaceous structures synthesized under various conditions.

ID	S_{BET} (m ² /g)	V_{mic} (cm ³ /g)	V_{mez} (cm ³ /g)	V_{tot} (cm ³ /g)	V_{mic}/V_{tot}	V_{mez}/V_{tot}	D_p (Å)
WB/400/1	427	0.163	0.189	0.352	0.46	0.54	33.05
WB/500/1	1234	0.477	0.257	0.734	0.65	0.35	23.75
WB/600/1	1056	0.425	0.216	0.641	0.66	0.34	23.4
WB/400/2	685	0.251	0.233	0.484	0.52	0.48	28.23
WB/500/2	1487	0.538	0.632	1.17	0.46	0.54	23.54
WB/600/2	1439	0.526	0.298	0.824	0.64	0.36	22.92
WB/400/3	681	0.251	0.188	0.439	0.57	0.43	25.81
WB/500/3	1422	0.493	0.396	0.889	0.55	0.45	33.07
WB/600/3	1369	0.476	0.521	0.997	0.48	0.52	29.13

structures in Table 3.

When the surface areas of the samples are compared according to the carbonization temperatures after chemical impregnation at 1:1, 2:1 and 3:1 $ZnCl_2$ /raw material ratios, it shows that the carbonization process at 500 °C is effective in increasing the surface area. In all IRs, micropore volumes first increased from 400 °C to 500 °C and then were adversely affected by the temperature increase. As the temperature increased from 400 °C to 600 °C in 1:1 and 2:1 IRs, the V_{mic}/V_{tot} ratio changed in direct proportion to the temperature increase, while the V_{mez}/V_{tot} ratio was adversely affected. Mean pore diameters contracted from 33.05 Å to 23.40 Å for 1:1 and from 28.23 Å to 22.92 Å for 2:1 IRs, respectively. In the 3:1 IR, the opposite results were encountered. When the chemical impregnation process was carried out with a $ZnCl_2$ /raw material ratio of 3, the increase in the temperature at which carbonization took place (400 °C-600 °C) caused changes in the micro and meso pore ratios. The change in temperature caused V_{mic}/V_{tot} to change from 0.57 to 0.48 and V_{mez}/V_{tot} to change from 0.43 to 0.52. With the increasing temperature at the high impregnation ratio, the micropores expanded and turned into meso pores.

When the surface areas covered by the porous structures of the synthesized carbon-structured materials are compared to the IR at 500 °C, the highest surface area and pore volume were obtained as 1487m²/g and 1.17 cm³/g respectively at a 2:1 IR. As the amount of $ZnCl_2$ used in activation increased at all temperatures, both micro and mesopores first increased for IR 1:1 to 2:1 and then were adversely affected when the IR increased from 2:1 to 3:1. Similar to our study findings, Zhang et al. discovered that excessive chemical use leads to the degradation of pore structures. They observed that the activated carbons they produced from wheat bran with NaOH displayed underdeveloped pore structures at a low impregnation rate (IR; 3:1). Furthermore, they noted that the pores were damaged when they employed high amounts of alkali (IR: 5/:1) (Zhang et al. 2019).

These results highlight the effect of impregnation ratio and temperature parameters on surface properties in the synthesis of porous carbonaceous structures. It was concluded that the study in the production of activated carbon by $ZnCl_2$ activation from wheat bran at 600 °C and at an IR of 3:1 adversely affects the surface area. It has been determined that the highest surface area can be achieved with activated

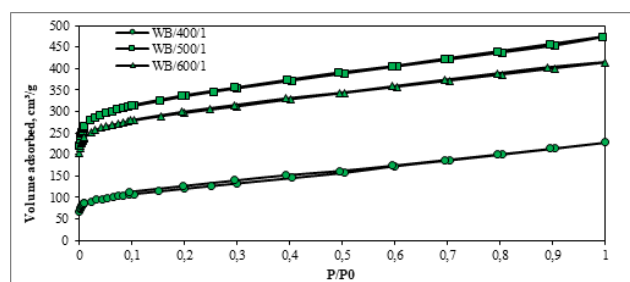
carbon production at 500 °C IR of 2:1. Examples of surface areas of activated carbons produced from various sources are given in Table 4.

Table 4 Production methods and surface areas of activated carbons produced from various biomass sources.

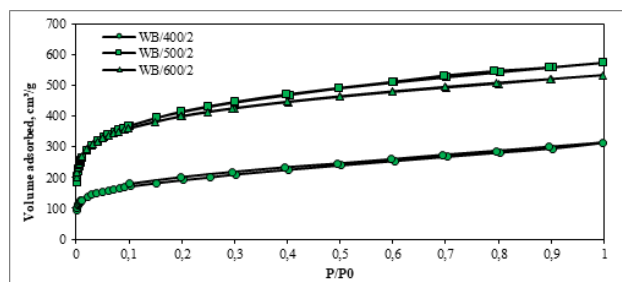
Raw materials	Activation Method	Surface Area	Reference
Wheat Bran	NaOH /Chemical activation	2543 m ² /g	(Zhang et al. 2004)
Date Palm	H ₃ PO ₄ / Chemical activation	1283 m ² /g	(Daoud et al. 2019)
Jujube beans	H ₃ PO ₄ / Chemical activation	1896 m ² /g	they applied to eliminate a commercial reactive dye BEZAKTIV Red S-Max (BRSM)
Barley stalk	CO ₂ / Physical activation	789 m ² /g	(Pallares et al. 2018)
Barley stalk	Steam / Physical activation	553 m ² /g	
Cherry stone	ZnCl ₂ / Chemical activation	1704 m ² /g	(Angin 2014)
Wheat Bran	ZnCl ₂ / Chemical activation	1487 m ² /g	in this study

Volumetric changes of N₂ gas adsorbed on the surface of synthesized porous materials with relative pressure

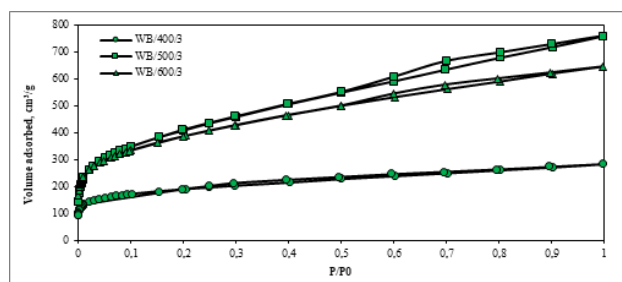
Adsorption-desorption isotherm are graphs that show the relationship between the relative pressure applied at constant temperature and the amount of gas adsorbed or desorbed. Classified by the International Union of Pure and Applied Chemistry (IUPAC), these isotherms are divided into six different categories. Figure 4 presents the N₂ adsorption-desorption isotherm graphs of porous materials synthesized at three different temperatures when impregnation was made using chemicals with the ZnCl₂/raw material ratio of 1:1, 2:1 and 3:1 in the chemical activation stage.



(a)



(b)



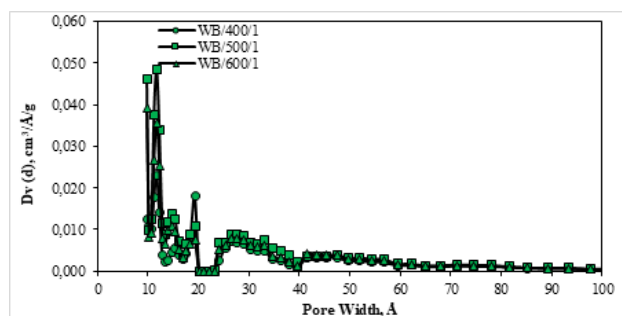
(c)

Figure 4 N₂ adsorption-desorption isotherm graphs of porous materials synthesized at three different temperatures at (a) 1:1 IR, (b) 2:1 IR, and (c) 3:1 IR.

As shown in Figure 4 (a) and (b), our activated carbon samples have been rigorously tested and found to comply with Type I isotherms as classified by IUPAC. This confirms that the pore structures of our product have more micro-sized pore diameters. Type I isotherms exhibit a rapid rise at low pressures, which then slows down as saturation is reached (Leong et al. 2019). The WB/400/3 conformed to Type I isotherms, while the WB/500/3 and WB/600/3 samples conformed to Type I and Type IV isotherms (Figure 4 (c)). Type IV isotherms are characterized by hysteresis resulting from intrapore condensations at high relative pressures. They are commonly found in porous materials with narrow-mouth pore structures containing mesopores (Meng et al. 2019).

Pore size distributions of synthesized porous materials

The pore structures of various adsorbents may vary in different widths, lengths and diameters. Figure 5 shows the diversity of pore sizes for each sample.



(a)

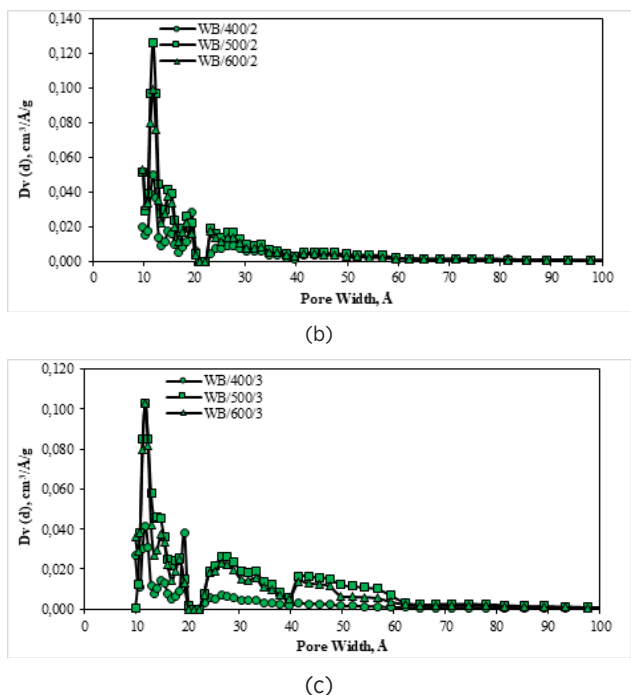


Figure 5 Pore size distributions of porous materials synthesized at three different temperatures at (a) 1:1 IR, (b) 2:1 IR, and (c) 3:1 IR

Figure 5 shows the pore size distributions of activated carbons produced at different IRs and carbonization temperatures. As a result of the examination, it is seen that the vast majority of these activated carbons have micropores between 10-20 Å (1-2 nm). However, meso pore peaks between 20-60 Å were also detected in some samples.

Acidic groups and basic groups amounts of synthesized porous materials determined by Boehm method

Among the activated carbons produced in this study, the highest surface area was obtained in WB/500/2. Acidic groups and basic groups amounts of WB/500/2 is given in Table 5.

Table 5 Acidic groups and basic groups amounts of WB/500/2.

Total acidic group (mmol/g)	Total basic group (mmol/g)	Lactonic (mmol/g)	Phenolic (mmol/g)	Carboxylic (mmol/g)
0.88	0.54	0.1	0.44	0.3

Boehm titration is a widely used method for determining the organic structural functionality of carbonaceous materials. This method separates various surface functional groups from each other using NaOH, Na₂CO₃, and NaHCO₃ compounds. NaHCO₃ detects carboxylic groups, Na₂CO₃ detects lactonic groups, and NaOH detects phenolic groups. The method is very effective in determining the functional groups in the structure, especially in adsorption studies (Liu et al. 2018). The total acidity and alkalinity values of the WB/500/2 sample were determined to be 0.88 and 0.54 mmol/g, respectively. It can be said that the sample contains lactonic, phenolic, and carboxylic groups on its surface. Activated carbon has an

amphoteric structure with both acidic and basic functional groups on its surface.

FT-IR analysis results of synthesized porous materials

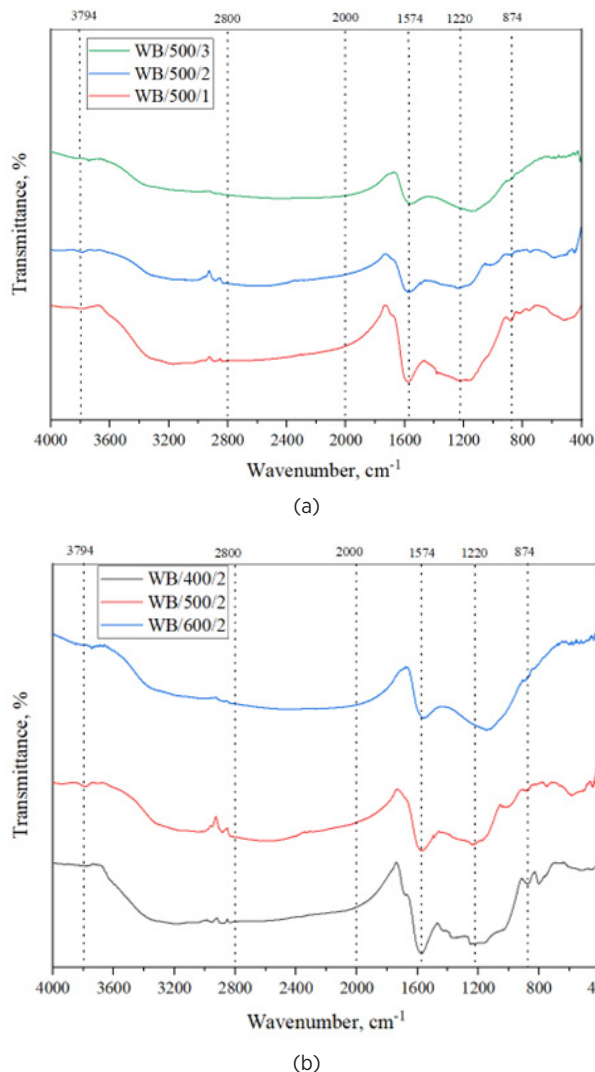


Figure 6 (a) shows FT-IR images of samples WB/500/1, WB/500/2 and WB/500/3 while Figure 6 (b) displays FT-IR images of samples WB/400/2, WB/500/2 and WB/600/2.

The IR spectra seen in Figure 6 shows peaks at 2885, 1574, 1220, 1157 and 874, 816 cm⁻¹. The peak at 3794 cm⁻¹ in the spectra of WB/500/2 and WB/600/2 may indicate the presence of hydroxyl (-OH) groups (Fanning and Vannice 1993; Shafeeyan et al. 2011; Hoseinzadeh Hesas et al. 2013). The peaks seen between 2800-2000 cm⁻¹ are generally attributed to ν(C≡C) vibration in alkyne groups and ν(C-H) bond vibrations in aldehydes (Boonamnuayvitaya et al. 2005; Deng et al. 2009; Hoseinzadeh Hesas et al. 2013). The broad band seen at 1574 cm⁻¹ indicates the presence of ν(C=C) bonds in aromatic functional groups (Baccar et al. 2009; Kaouah et al. 2013). This indicates that there are aromatic components in the structure of activated carbon. The band at 1220 cm⁻¹ may indicate the presence of ν(C-O) bonds (Guo and Rockstraw 2007; Liu et al. 2010). The peak at 874 cm⁻¹ may indicate the presence of C-Cl

bonds. In the structure of this activated carbon, chlorinated components from $ZnCl_2$ can be found (Mahapatra et al. 2012).

Elemental analysis results of synthesized porous materials

The elemental analysis results of the samples WB/500/1, WB/500/2 and WB/500/3 are given in Table 6. According to the results, when the IR value increased from 1:1 to 2:1 at 500 °C, the carbon composition of the activated carbon first increased slightly. When the IR value increased to 3:1, the carbon amount decreased. This indicates that large amounts of $ZnCl_2$ result in a lower carbon yield. Moreover, as the impregnation ratio increased, there was a decrease in the nitrogen composition and an increase in the oxygen composition. This suggests that on the synthesized porous materials, the number of N-containing functional groups decreased while oxygen-containing groups increased.

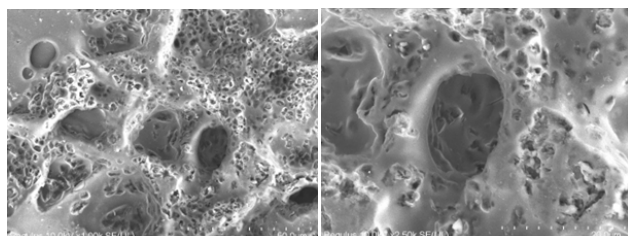
Table 6 The elemental analysis results of the samples WB/500/1, WB/500/2 and WB/500/3.

	%C	%N	%O
WB/500/1	86.43	5.76	6.93
WB/500/2	88.41	4.17	6.89
WB/500/3	73.21	0.67	26.12

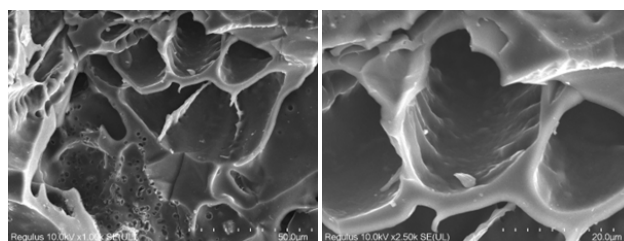
SEM (Scanning Electron Microscope) images of synthesized porous materials

The SEM images of the WB/400/2, WB/500/2 and WB/600/2 examples are given Figure 7. From Figure 7, the change in the pore structure of the activated carbon according to the production temperature can be seen in the 2:1 IR. When the images are examined, it can be seen that the pores of the WB/400/2 sample have started to form, the WB/500/2 sample has more prominent and larger pores, and the WB/600/2 has a less porous structure.

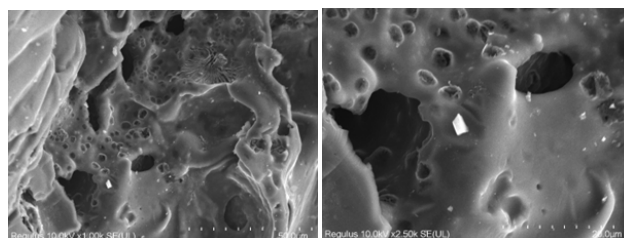
These results show that production temperature conditions have a significant effect on the pore structure of activated carbon. Activated carbons produced at 500 °C tend to have larger and more prominent pores. However, when the temperature is raised to 600 °C, the structure of the pores can be disrupted and adversely affect the surface area of the activated carbon.



(a)

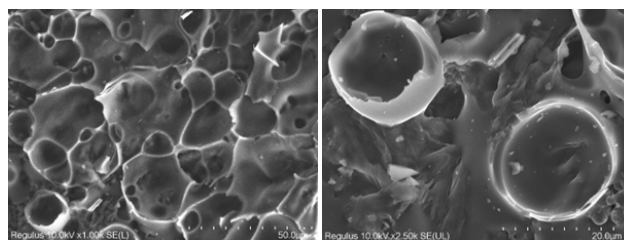


(b)

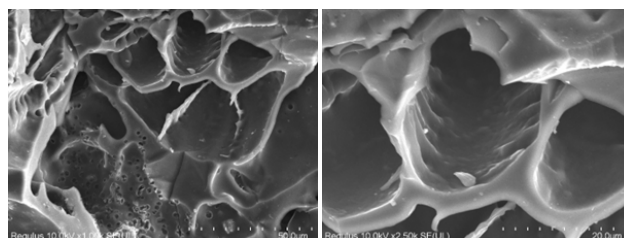


(c)

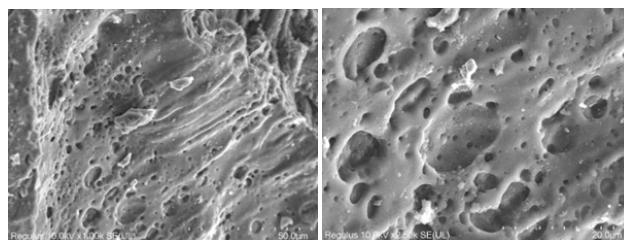
Figure 7 SEM images of synthesized porous materials at 1000 and 25000 magnifications, (a) WB/400/2, (b) WB/500/2 and, (c) WB/600/2



(a)



(b)



(c)

Figure 8 SEM images of synthesized porous materials at 1000 and 25000 magnifications, (a) WB/500/1, (b) WB/500/2 and, (c) WB/500/3

The SEM images presented in Figure 8 illustrate the impact of the impregnation ratio on the pore structure of synthesized porous materials during its production process. Synthesized

porous material with a 1:1 ZnCl₂/raw material has very small and densely packed pores, while synthesized porous material with a 2:1 ZnCl₂/raw material has wider and less dense pores. However, the synthesized porous material with a 3:1 ZnCl₂/raw material has a less porous structure as the very high impregnation ratio has closed the pores.

CONCLUSION

In this study, activated carbon was produced from wheat bran by the chemical activation method. WB has low ash content (7.05%), carbon (52.61%) and oxygen (43.59%). The increase in the amount of chloride salt used in the chemical activation phase caused a decrease in the carbon content of active carbons and an increase in the oxygen content. The influence of temperature on the surface areas of activated carbons is more significant than the impact of varying the amount of ZnCl₂. When the surface areas of the samples were compared according to the carbonization temperatures after the chemical impregnation process performed at ZnCl₂/raw material ratios as 1:1, 2:1 and 3:1, the highest surface area was obtained at 500 °C as 1234, 1478, and 1422 m²/g, respectively. The highest surface area was obtained as 1487 m²/g in the WB/500/2 sample. The temperature increases in 1:1 and 2:1 impregnation ratio (from 400 °C to 600 °C) led to a decrease in the average pore diameters of the activated carbons.

Acknowledgment

This study was prepared within the scope of the Master's Thesis studies conducted by Fatma Betül Kuş, a student of Eskişehir Osmangazi University, Institute of Natural and Applied Sciences, Department of Chemical Engineering.

References

- Daoud M, Benturki O, Girods P, Donnot A, Fontana S. Adsorption ability of activated carbons from Phoenix dactylifera rachis and Ziziphus jujube stones for the removal of commercial dye and the treatment of dyestuff wastewater. *Microchem J.* 2019 Jul;148:493–502.
- Azam K, Shezad N, Shafiq I, Akhter P, Akhtar F, Jamil F, et al. A review on activated carbon modifications for the treatment of wastewater containing anionic dyes. *Chemosphere.* 2022 Nov 1;306:135566.
- Mahmoud Amer, Ahmed Elwardany. Biomass Carbonization. In: Mansour Al Qubeissi, Ahmad El-kharouf, Hakan Serhad Soyhan, editors. *Renewable Energy* [Internet]. Rijeka: IntechOpen; 2020 [cited 2024 May 25]. p. Ch. 11. Available from: <https://doi.org/10.5772/intechopen.90480>
- Reza MS, Yun CS, Afroze S, Radenahmad N, Bakar MSA, Saidur R, et al. Preparation of activated carbon from biomass and its' applications in water and gas purification, a review. *Arab J Basic Appl Sci.* 2020 Jan 1;27(1):208–38.
- Świątkowski A. Industrial carbon adsorbents. In: *Adsorption and its Applications in Industry and Environmental Protection.* 1999. (Studies in Surface Science and Catalysis; vol. 179).
- Rafatullah Mohd, Sulaiman O, Hashim R, Ahmad A. Adsorption of methylene blue on low-cost adsorbents: A review. *J Hazard Mater.* 2010 May;177(1–3):70–80.
- Tadda MA, Ahsan A, Shitu A, ElSergany M, Arunkumar T, Jose B, et al. A review on activated carbon: process, application and prospects. *J Adv Civ Eng Pract Res.* 2016;2(1):7–13.
- FAOSTAT. Value of Agricultural Production [Internet]. 2024. Available from: <https://www.fao.org/faostat/en/#data/QV>
- Zhang Y. Preparation of Hierarchical Porous Carbon from Wheat Bran for Free-Standing Electrode of High Areal Capacitance Supercapacitor.
- Koli A, Kumar A, Pattanshetti A, Supale A, Garadkar K, Shen J, et al. Hierarchical Porous Activated Carbon from Wheat Bran Agro-Waste: Applications in Carbon Dioxide Capture, Dye Removal, Oxygen and Hydrogen Evolution Reactions. *ChemPlusChem.* 2024 Mar;89(3):e202300373.
- Wang D, Min Y, Yu Y. Facile synthesis of wheat bran-derived honeycomb-like hierarchical carbon for advanced symmetric supercapacitor applications. *J Solid State Electrochem.* 2015 Feb;19(2):577–84.
- Hu X, Li Y, Du J, Sun J, He C, Xiong Y, et al. Waste Biomass-Derived Carbon with Ultrahigh Adsorption Capacity for Anionic and Cationic Dyes and Antibiotics in a Wide pH Range. *Ind Eng Chem Res.* 2024 Mar 13;63(10):4702–13.
- Ioannidou O, Zabaniotou A. Agricultural residues as precursors for activated carbon production—A review. *Renew Sustain Energy Rev.* 2007 Dec;11(9):1966–2005.
- Ma Y. Comparison of Activated Carbons Prepared from Wheat Straw via ZnCl₂ and KOH Activation. *Waste Biomass Valorization.* 2017 Apr;8(3):549–59.
- Kierzek K, Gryglewicz G. Activated Carbons and Their Evaluation in Electric Double Layer Capacitors. *Molecules.* 2020 Sep 16;25(18):4255.
- Zhao H, Zhong H, Jiang Y, Li H, Tang P, Li D, et al. Porous ZnCl₂-Activated Carbon from Shaddock Peel: Methylene Blue Adsorption Behavior. *Materials.* 2022 Jan 25;15(3):895.
- Ma J, Yang H, Li L, Xie X, Liu B, Zhang L. Synthesis of Aligned ZnO Submicron Rod Arrays by Heating Zinc Foil Covered with ZnCl₂ Solution. *Acta Chim Sin.* 2009 Jul 14;67:1515–22.
- Moralı U, Demiral H, Şensöz S. Optimization of activated carbon production from sunflower seed extracted meal: Taguchi design of experiment approach and analysis of variance. *J Clean Prod.* 2018 Jul;189:602–11.
- Demiral H, Gündüzoğlu G. Removal of nitrate from aqueous solutions by activated carbon prepared from sugar beet bagasse. *Bioresour Technol.* 2010 Mar;101(6):1675–80.
- Ghodrat A, Yaghobfar A, Ebrahimnezhad Y, Aghdam Shahryar H, Gorbani A. In vitro Binding Capacity of Wheat and Barley for Mn, Zn, Cu and Fe. *Int J Life Sci.* 2015 Sep 26;9:56.
- Li C, Wang L, Chen Z, Li Y, Luo X, Zhao F. Ozonolysis of wheat bran in subcritical water for enzymatic saccharification and polysaccharide recovery. *J Supercrit Fluids.* 2021 Feb;168:105092.
- Escalante J, Chen WH, Tabatabaei M, Hoang AT, Kwon EE, Andrew Lin KY, et al. Pyrolysis of lignocellulosic, algal, plastic, and other biomass wastes for biofuel production and circular bioeconomy: A review of thermogravimetric analysis (TGA) approach. *Renew Sustain Energy Rev.* 2022 Nov;169:112914.
- Pooladi H, Foroutan R, Esmaeili H. Synthesis of wheat bran sawdust/Fe₃O₄ composite for the removal of methylene blue and methyl violet. *Environ Monit Assess.* 2021 Apr 16;193(5):276.
- Kabdaşlı I, Vardar B, Arslan-Alaton I, Tünay O. Effect of dye auxiliaries on color and COD removal from simulated reactive dye bath effluent by electrocoagulation. *Chem Eng J.* 2009 May;148(1):89–96.
- Shafeeyan MS, Daud WMAW, Houshmand A, Shamiri A. A review on surface modification of activated carbon for carbon dioxide adsorption. *J Anal Appl Pyrolysis.* 2010 Nov;89(2):143–51.

26. Pellenz L, De Oliveira CRS, Da Silva Júnior AH, Da Silva LJS, Da Silva L, Ulson De Souza AA, et al. A comprehensive guide for characterization of adsorbent materials. *Sep Purif Technol.* 2023 Jan;305:122435.
27. Fanning PE, Vannice MA. A DRIFTS study of the formation of surface groups on carbon by oxidation. *Carbon.* 1993;31(5):721-30.
28. Shafeeyan MS, Daud WMAW, Houshmand A, Arami-Niya A. Ammonia modification of activated carbon to enhance carbon dioxide adsorption: Effect of pre-oxidation. *Appl Surf Sci.* 2011 Feb;257(9):3936-42.
29. Hoseinzadeh Hesas R, Arami-Niya A, Wan Daud WMA, Sahu JN. Preparation and Characterization of Activated Carbon from Apple Waste by Microwave-Assisted Phosphoric Acid Activation: Application in Methylene Blue Adsorption. *BioResources.* 2013 Apr 30;8(2):2950-66.
30. Shen DK, Gu S, Bridgwater AV. Study on the pyrolytic behaviour of xylan-based hemicellulose using TG-FTIR and Py-GC-FTIR. *J Anal Appl Pyrolysis.* 2010 Mar;87(2):199-206.
31. Kaouah F, Boumaza S, Berrama T, Trari M, Bendjama Z. Preparation and characterization of activated carbon from wild olive cores (oleaster) by H₃PO₄ for the removal of Basic Red 46. *J Clean Prod.* 2013 Sep;54:296-306.
32. Jia Y, Xiao B, Thomas K. Adsorption of metal ions on nitrogen surface functional groups in activated carbons. *Langmuir.* 2001 Dec;18.
33. Gulnaz O, Kaya A, Dincer S. The reuse of dried activated sludge for adsorption of reactive dye. *J Hazard Mater.* 2006 Jun;134(1-3):190-6.
34. Biniak S, Świątkowski A, Pakula M, Sankowska M, Kuśmierk K, Trykowski G. Cyclic voltammetric and FTIR studies of powdered carbon electrodes in the electrosorption of 4-chlorophenols from aqueous electrolytes. *Carbon.* 2013 Jan;51:301-12.
35. Barroso-Bogeat A, Alexandre-Franco M, Fernandez-Gonzalez C, Gomez-Serrano V. FT-IR Analysis of Pyrone and Chromene Structures in Activated Carbon. *Energy Fuels.* 2014 Jun;28(6):4096-103.
36. Cagniant D, Gruber R, Boudou JP, Bilem C, Bimer J, Salbut PD. Structural Characterization of Nitrogen-Enriched Coals. *Energy Fuels.* 1998 Jul 1;12(4):672-81.
37. Boonamnuayvitaya V, Sae-ung S, Tanthapanichakoon W. Preparation of activated carbons from coffee residue for the adsorption of formaldehyde. *Sep Purif Technol.* 2005 Mar;42(2):159-68.
38. El-Hendawy ANA. Variation in the FTIR spectra of a biomass under impregnation, carbonization and oxidation conditions. *J Anal Appl Pyrolysis.* 2006 Mar;75(2):159-66.
39. Guo Y, Rockstraw DA. Activated carbons prepared from rice hull by one-step phosphoric acid activation. *Microporous Mesoporous Mater.* 2007 Mar;100(1-3):12-9.
40. Momcilovic M, Purenovic M, Bojic A, Zarubica A, Randelovic M. Removal of lead(II) ions from aqueous solutions by adsorption onto pine cone activated carbon. *Desalination.* 2011 Aug;276(1-3):53-9.
41. Gurten II, Ozmak M, Yagmur E, Aktas Z. Preparation and characterisation of activated carbon from waste tea using K₂CO₃. *Biomass Bioenergy.* 2012 Feb;37:73-81.
42. Xu J, Chen L, Qu H, Jiao Y, Xie J, Xing G. Preparation and characterization of activated carbon from reedy grass leaves by chemical activation with H₃PO₄. *Appl Surf Sci.* 2014 Nov;320:674-80.
43. Silva TP, Ferreira AN, De Albuquerque FS, De Almeida Barros AC, Da Luz JMR, Gomes FS, et al. Box-Behnken experimental design for the optimization of enzymatic saccharification of wheat bran. *Biomass Convers Biorefinery.* 2022 Dec;12(12):5597-604.
44. Chaquilla-Quilca G, Balandrán-Quintana RR, Azamar-Barrios JA, Ramos-Clamont Montfort G, Mendoza-Wilson AM, Mercado-Ruiz JN, et al. Synthesis of tubular nanostructures from wheat bran albumins during proteolysis with V8 protease in the presence of calcium ions. *Food Chem.* 2016 Jun;200:16-23.
45. Zhang Y, Song X, Xu Y, Shen H, Kong X, Xu H. Utilization of wheat bran for producing activated carbon with high specific surface area via NaOH activation using industrial furnace. *J Clean Prod.* 2019 Feb;210:366-75.
46. Zhang T, Walawender W, Fan L, Fan M, Daugaard D, Brown R. Preparation of activated carbon from forest and agricultural residues through CO activation. *Chem Eng J.* 2004 Dec 15;105(1-2):53-9.
47. Pallares J, González-Cencerrado A, Arauzo I. Production and characterization of activated carbon from barley straw by physical activation with carbon dioxide and steam. *Biomass Bioenergy.* 2018 Aug;115:64-73.
48. Angin D. Production and characterization of activated carbon from sour cherry stones by zinc chloride. *Fuel.* 2014 Jan;115:804-11.
49. Leong ZY, Lu G, Yang HY. Three-dimensional graphene oxide and polyvinyl alcohol composites as structured activated carbons for capacitive desalination. *Desalination.* 2019 Feb;451:172-81.
50. Meng H shan, Chen C, Yan Z run, Li X yan, Xu J, Sheng G ping. Co-doping polymethyl methacrylate and copper tailings to improve the performances of sludge-derived particle electrode. *Water Res.* 2019 Nov;165:115016.
51. Liu Z, Zhao C, Wang P, Zheng H, Sun Y, Dionysiou DD. Removal of carbamazepine in water by electro-activated carbon fiber-peroxydisulfate: Comparison, optimization, recycle, and mechanism study. *Chem Eng J.* 2018 Jul;343:28-36.
52. Deng H, Yang L, Tao G, Dai J. Preparation and characterization of activated carbon from cotton stalk by microwave assisted chemical activation—Application in methylene blue adsorption from aqueous solution. *J Hazard Mater.* 2009 Jul 30;166(2-3):1514-21.
53. Baccar R, Bouzid J, Feki M, Montiel A. Preparation of activated carbon from Tunisian olive-waste cakes and its application for adsorption of heavy metal ions. *J Hazard Mater.* 2009 Mar;162(2-3):1522-9.
54. Liu QS, Zheng T, Wang P, Guo L. Preparation and characterization of activated carbon from bamboo by microwave-induced phosphoric acid activation. *Ind Crops Prod.* 2010 Mar;31(2):233-8.
55. Mahapatra K, Ramteke DS, Paliwal LJ. Production of activated carbon from sludge of food processing industry under controlled pyrolysis and its application for methylene blue removal. *J Anal Appl Pyrolysis.* 2012 May;95:79-86.

HITTITE JOURNAL OF SCIENCE AND ENGINEERING

e-ISSN: 2148-4171
Volume: 11 • Number: 3
September 2024

Investigation of the Defect Effects on the Load-Carrying Capacity of Butt Joints: A Numerical Study

Hamza Taş 

Manisa Celal Bayar University, Hasan Ferdi Turgutlu Faculty of Technology, Department of Mechanical Engineering, 45400, Manisa, Türkiye.

Corresponding Author

Hamza Taş

E-mail: hamza.tas36@gmail.com Phone: +90 236 314 1010

RORID: <https://ror.org/053f2w588>

Article Information

Article Type: Research Article

Doi: <https://doi.org/10.17350/HJSE19030000337>

Received: 06.04.2024

Accepted: 05.07.2024

Published: 30.09.2024

Cite As

Taş, H. Investigation of the Defect Effects on the Load-Carrying Capacity of Butt Joints: A Numerical Study. Hittite J Sci Eng. 2024;11(3):105-113.

Peer Review: Evaluated by independent reviewers working in at least two different institutions appointed by the field editor.

Ethical Statement: Not available.

Plagiarism Checks: Yes - iThenticate

Conflict of Interest: Authors approve that to the best of their knowledge, there is not any conflict of interest or common interest with an institution/organization or a person that may affect the review process of the paper.

CRedit AUTHOR STATEMENT

Hamza Taş: Conceptualization, Investigation, Methodology, Validation, Visualization, Writing- original draft,

Copyright & License: Authors publishing with the journal retain the copyright of their work licensed under CC BY-NC 4.

Investigation of the Defect Effects on the Load-Carrying Capacity of Butt Joints: A Numerical Study

Hamza Taş

Manisa Celal Bayar University, Hasan Ferdi Turgutlu Faculty of Technology, Department of Mechanical Engineering, 45400, Manisa, Türkiye.

Abstract

Determining the behavior of joints under a specific load and estimating the damage potential is essential for ensuring the durability of joints in engineering structures. Defects might occur at the adhesive layer, which causes a reduction in the durability of joints. This work aims to examine the effects of the defect presence, defect volume fraction, defect position, and random distribution of defects at the adhesive layer on the durability of the butt joint. A finite element (FE) model of the butt joint was constructed using the commercially available FE software Abaqus/Standard. The validation of the FE model was conducted by comparing its results with experimental finding reported in existing literature. Numerical and experimental results showed strong agreement, with relative errors of 2.46% and 2.95% at peak force and displacement at peak force, respectively. Defect presence significantly influences the durability of the butt joint. Defect volume fraction and defect location are the dominant parameters affecting the durability of the butt joint. The square defects at the center of the bonding layer, with volume fractions of 0.05, 0.10, and 0.15, lowers the peak force by 5.08%, 10.56%, and 15.73%, respectively. When the defect is positioned at the center of the bonding layer, adhesive failure starts at the edges of the defects. However, relocating the defect from the center to the left or upper side of the bonding layer results in adhesive failure initiation at the corresponding edges of the adhesive. Random defect distribution in the adhesive layer doesn't affect joint durability.

Keywords: Finite element analysis, Butt joint, Adhesive, Defect, Cohesive zone model

INTRODUCTION

In the last eighty years, the use of adhesively bonded joints has grown due to their advantages over the traditional mechanical fasteners, welding, and brazing [1–4]. Conventional joining techniques including bolting and riveting introduce stress concentration around the application area, which severely impairs the mechanical properties of the joints. Besides, mechanical fasteners can raise the weight of the structure. Adhesively bonded joints could potentially overcome these limitations [5,6]. The key benefits of adhesively bonded joints include uniform stress distribution, cost effectiveness, no need for machining, milling, or forming operations, good strength to weight ratio and high fatigue resistance [7–10]. However, considering their manufacturing sensitivity, adhesively bonded joints are susceptible to defects [3]. Every manufacturing process inherently results in some defects because producing defect-free joints, despite strict controls, is nearly impossible. Entrapped air, dirt, foreign objects, and grease may cause defects in the bonded region. Since load cannot be transferred through these defects, stress concentrations occur around these defects [11]. Hence, it is essential to comprehend the effects of defects in the bonded region on the joint durability.

Many research have been conducted to investigate the effects of defect types [3,12–14], locations [3,11,14–17], shapes [8,15], sizes [8,12,14,16–18], and numbers [11,15,17] on joint strength. Geleta et al. [3] conducted experimental tests and finite element analysis (FEA) for inclined joints. Based on the experimental test results, they incorporated the potential production defect locations and types in the FE model. The results showed that defect types and locations play a crucial role on the joint strength. They further determined that the FE results align well with the experimental findings. Xu and Wei [14] considered three defect types: local debonding, weak bonding, and void. The outcomes of the FEA also revealed that joint strength is significantly influenced by the presence of different types of defects. Jamal-Omidi and Mohammadi Suki [12] considered two different types of defects: void modeled as local delamination in varying dimensions, and locally insufficient bonding characterized as an alteration in the properties of adhesive. The results indicated that defects adversely influence the joint durability. Nevertheless, defect existence in the bonding layer does not change stress field in adherends. Luo et al. [13] worked the influences of the

different kinds of flaws (core material flaw, radius floating of the fillet, and debonding defects) on the strength of composite T-joints under bending load through experiments and numerical analysis. They used cohesive elements to simulate the delamination of interface. The outcomes demonstrated that the types of flaws have no influence on the T-joint failure mode. However, they have a notable impact on the T-joint strength. In addition, it has been noted that the most dangerous type of flaw is the debonding defect in the arc region. Fame et al. [17] examined the failure sensitivity of adhesively bonded GFRP joints under uniaxial tensile loading utilizing FE method, while considering flaws at varied positions, numbers, and sizes in the bondline. According to the findings of the finite element analysis, bondline defects cause an increment in out-of-plane displacement of adherends as well as maximum shear and peel stresses at the edges of adhesive. Areas close to the defects also showed high stress concentrations. Heidarpour et al. [8] conducted an experimental study to examine the impacts of shape and size of 2D and 3D flaws on the adhesively bonded single lap joint (SLJ) durability. The findings revealed that for the joint with 3D defects, joint strength drops approximately linearly with the rise of defect area. However, reduction in joint durability for the joint with 2D defect is non-linear. It is also concluded that whereas 2D circular defects result in a lesser strength drop, 2D triangular and square defects cause similar strength reductions. Additionally, compared to 3D circular and square flaws, the strength drop for 3D triangular flaws is higher. Elhannani et al. [15] analyzed the effects of shape, position and number of bonding flaws on the shear stress distribution in the overlap area. Numerical analyzes showed that bonding defects adversely affect the shear stress distribution and that maximum stresses constantly occur at the adhesive edge, without considering the defect size. Dai et al. [16] focused on developing a theoretical model for resolving the multi-failed mechanical problem of an adhesively bonded joint with/without interfacial flaws, and examining the effects of interfacial flaws and hygrothermal conditions on the stress distribution. The results revealed that the effect of the change in defect length is more significant than the effect of defect depth in variations of interfacial stress. Moreover, defects close the edges of the overlap creates a greater risk to the joint. Ribeiro et al. [19] conducted a numerical and experimental investigation into the SLJs with flaws positioned at the center of the adhesive layer for various adhesives and

bonding lengths. According to the findings, the joints bonded with the adhesive 7752 are more influenced by the existence of center-positioned defects in the bonding layer than those bonded with the adhesive AV138.

The existing studies investigating the impact of defect presence, defect volume fraction, defect location, and defect random distribution on the load-carrying capacity of joints, particularly butt joints where normal stress in the adhesive is dominant, remain insufficient. Meanwhile, research efforts predominantly focus on assessing the influence of flaws within the bonding layer specifically for single/double lap joints, T-joints, and inclined joints. This study aims to address the literature gap by primarily investigating the impact of defects within the bonding layer on the load-bearing capacity of butt joints. A three-dimensional FE model was constructed using Abaqus/Standard to investigate the response of the butt joint with/without defect in the bonding layer under uniaxial tensile loading conditions, with a specific emphasis on cohesive failure in the adhesive layer. The accuracy of the numerical model was validated through a comparison with the experimental findings of Ref. [20]. The investigation encompasses an analysis of the effects of defect presence, defect volume fraction, defect position, and random distribution of flaws in the bonding layer on the load-bearing capacity of the butt joint.

NUMERICAL STUDY

In the present study, finite element analysis (FEA) of adhesively bonded butt joints were carried out by using a commercially available FEA software Abaqus/Standard. The 3-D geometric model of butt joint and its dimensions are shown in Fig. 1. The adherend dimensions are 100 mm in length, 25 mm in width, and 5 mm in thickness, while the adhesive layer has a thickness of 0.18 mm. The adherends and adhesive were considered as AA2024-T3 aluminum alloy and DP460 epoxy adhesive. The selection of adherend and adhesive materials was based on practical engineering applications [21]. DP460 adhesive is utilized for adhering metal, porcelain, glass, and a variety of composite materials together [22]. The mechanical characteristics of adherend and adhesive used in this study are presented in Table 1. Despite the non-linear behavior of the AA2024-T3 aluminum alloy, adherends were modeled as a linear-elastic material. Because, as can be seen in the following sections, the maximum strain value of aluminum is still in the elastic region when the adhesive fails.

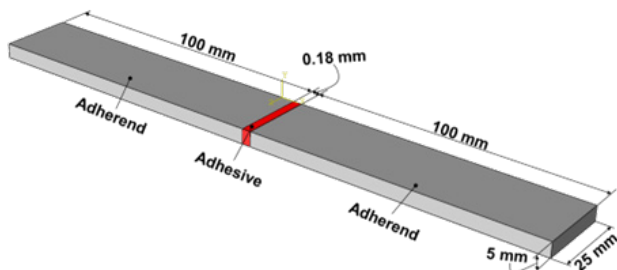


Figure 1 3D geometric model of butt joint (not scaled)

Table 1 Mechanical properties of AA2024-T3 aluminum alloy and DP460 epoxy adhesive [20]

	AA2024-T3 aluminum alloy	DP460 epoxy adhesive
Young's modulus (MPa)	72400±530	2077±47
Poisson's ratio	0.33	0.38
Ultimate tensile strength (MPa)	482±12	44.6±1.2
Ultimate tensile strain (mm/mm)	0.1587	0.0428

The constructed mesh and applied boundary conditions are presented in Fig. 2. The adherends were modeled using 8-nodes linear hex elements (C3D8R) while adhesive layer was meshed with 8-nodes three-dimensional cohesive elements (COH3D8). The adhesive layer's mesh comprised fine elements, whereas coarse elements constituted the mesh of the adherends. 0.6×0.6×0.6 mm³ and 0.2×0.2×0.2 mm³ element dimensions were taken into consideration for adherends and adhesive, respectively. Besides, it is critical to emphasize that the adhesive layer was modeled as a single layer of cohesive element through the thickness. In the opposite case, the calculation doesn't converge [9,23–25]. The surface-to-surface tie constraint was employed to tie adherend and adhesive surfaces with differing mesh structures. As for the boundary conditions, the adhesively bonded butt joint was fixed in all directions at one end, while for the other end, it was fixed in all directions except the x-direction, and a 0.15 mm uniform displacement boundary condition in the x-direction was defined.

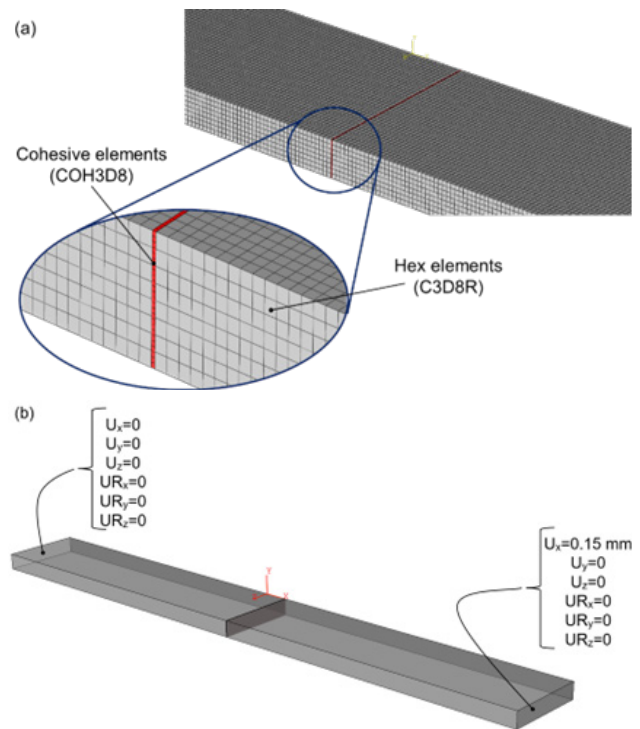


Figure 2 (a) Constructed mesh and (b) Applied boundary conditions

In this work, the adhesive's performance was determined utilizing the Cohesive Zone Model (CZM) integrated into Abaqus/Standard. CZM allows for the comprehensive definition of the fracture process through a traction-separation law, encompassing both tension and shear [1]. In the current study, a bi-linear traction-separation law was applied (Fig. 3). The first section of the traction-separation law is related to linear elastic behavior, whereas the second part refers to linear degradation [1,7]

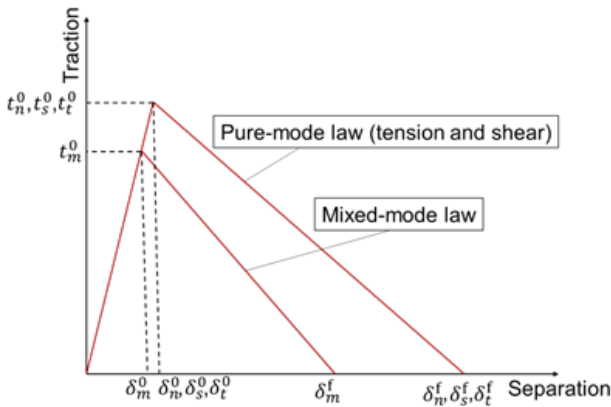


Figure 3 Bi-linear traction-separation law

In the current work, stress-based criterion for damage initiation (MAXS: Maximum nominal stress) was considered. According to the MAXS criterion, damage starts when the one of the maximum nominal stress ratios equals one. The damage initiation criterion, MAXS, can be expressed as follows:

$$\max \left\{ \frac{\langle t_n \rangle}{t_n^0}, \frac{t_s}{t_s^0}, \frac{t_t}{t_t^0} \right\} = 1 \quad (1)$$

where t_n^0 , t_s^0 , and t_t^0 , denote the maximum values of nominal stresses at the direction of normal, first shear, and second shear, respectively. t_n , t_s , and t_t are the predicted stress values at the normal, first shear, and second shear direction, respectively. Moreover, the Macaulay bracket, $\langle a \rangle$, indicates that compressive stress doesn't trigger damage [12].

In CZM, total failure and separation are calculated by a damage evolution law. In the current work, the energy-based Benzeggagh-Kenane (BK) [26] fracture criterion was considered. When the critical fracture energies at the first and second shear directions are identical ($G_{IIc} = G_{IIIc}$), this criterion produces more accurate results. It is expressed by:

$$G_{IC} + (G_{IIc} - G_{IC}) \left\{ \frac{G_S}{G_T} \right\}^\eta = G_C \quad (2)$$

where

$$G_S = G_{II} + G_{III}, \quad G_T = G_I + G_S \quad (3)$$

and η is a material parameter. G_I, G_{II} , and G_{III} denotes the normal and two shear fracture energies, respectively, whereas G_{IC}, G_{IIc} , and G_{IIIc} are their critical values [5]. In this work, η is chosen as 2. Properties of DP460 epoxy adhesive used in this

study for cohesive zone modeling are given in Table 2.

Table 2 Material properties of DP460 epoxy adhesive for cohesive zone modeling [27,28]

Property	Unit	Value
t_n^0	MPa	32.6
t_s^0	MPa	28.5
t_t^0	MPa	28.5
G_{IC}	N/mm	2.56
G_{IIc}	N/mm	11.71
G_{IIIc}	N/mm	11.71

Note: Traction and critical fracture energies in the first and second shear directions are assumed to be the same ($t_n^0 = t_t^0$ and $G_{IIc} = G_{IIIc}$).

Defect Modeling

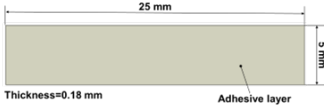
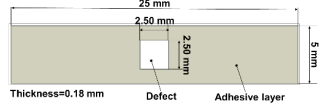
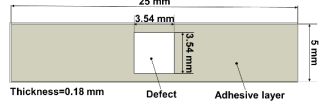
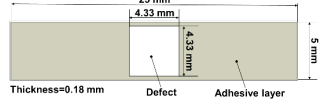
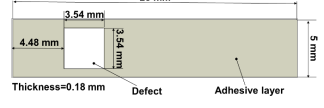

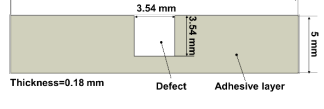

One of the main causes of the defects at the bonded region is the poor adhesive distribution, which could result from human mistakes or adherend surface imperfections. Poor adhesive distribution results in poor bonding which causes 2D (planar) and 3D (volumetric) defects [8]. In this work, the 3D (volumetric) defect was modeled as a blank volume at the adhesive. This study was mainly focused on the influences of flaw presence, volume fraction, location, and random distribution on the load carrying capacity of the butt joint. Defect volume fraction (V_f) is the ratio of defect volume to the total adhesive volume. In order to determine the impacts of the defect existence, a bonding layer with a defect volume fraction of 0.10 and therefore a square-shaped volumetric blank in its center was modeled. The impact of defect volume fraction was investigated considering the defect volume ratio of 0.05, 0.10, and 0.15. Defect ($V_f=0.1$) was shifted to the left and up to determine the effects of defect location. Regarding the influences of the defect random distribution, 3D (volumetric) defects with the dimensions of $0.25 \times 0.25 \times 0.18 \text{ mm}^3$ (7 pieces), $0.50 \times 0.50 \times 0.18 \text{ mm}^3$ (7 pieces), $0.75 \times 0.75 \times 0.18 \text{ mm}^3$ (6 pieces), and $1.00 \times 1.00 \times 0.18 \text{ mm}^3$ (7 pieces) were randomly distributed in the bonding layer. Defect details in the bonding layer are shown in Table 3.

Verification of the Numerical Model

The numerical model was verified by comparing the experimental findings of Ref. [20]. The 3D adhesively bonded SLJ with the 0.18 mm adhesive (DP460) thickness and 3 mm adherend (AA2024-T3) thickness was modeled. The length of the adhesive layer is 12.5 mm, and the length of the adherend is 100 mm. Moreover, the width of the adherend is 25 mm. Geometric details of SLJ can be found in Ref. [20]. As in the butt joint modeling, adherend and adhesive were meshed with 70140 linear hexahedral elements of type C3D8R and 7875 linear hexahedral elements of type COH3D8. For both adhesive and adherend, the same element sizes with the butt joint were considered. Moreover, identical material properties utilized for cohesive zone modeling in the butt joints were employed for SLJ. The adherend and adhesive surfaces with different mesh structures were tied using surface-to-surface tie constraint as in the butt joint. Regarding the boundary conditions, SLJ was fixed at one end in all directions and fixed at the other end in all directions except the longitudinal

direction of adherend. A 0.5 mm uniform displacement boundary condition was applied in the longitudinal direction of the adherend.

Table 3 Graphical representation and configuration of defects in adhesive layer

Configuration	Adhesive layer with/without defect
$V_f=0.00$	
$V_f=0.05$ (Center)	
$V_f=0.10$ (Center)	
$V_f=0.15$ (Center)	
Location-1 ($V_f=0.10$)	
Location-2 ($V_f=0.10$)	
Location-3 ($V_f=0.10$)	
Randomly distributed ($V_f=0.10$)	

In this study, identical boundary conditions, mesh structures, element types, material properties, and adhesive thicknesses were employed for FE modeling of both butt joints and SLJs. Despite different failure behaviors of the two joints, given identical modeling parameters and boundary conditions, SLJ could potentially serve for FE validation. This may be related to the versatility, robustness and effectiveness of the finite element method in capturing various failure mechanisms in various joint types.

The comparison of numerical and experimental findings concerning force-displacement curves is shown in Fig. 4. A good correlation between the experimental and numerical findings were observed. The average experimental failure load and displacement were reported as 8814 ± 202 N and 0.407 ± 0.02 mm, respectively [20]. Based on the FEA

findings, the failure load was estimated at 8597.1 N with a relative error of 2.46%, while the displacement was calculated to be 0.419 mm with a relative error of 2.95%. The strong correlation and minimal relative discrepancies observed between the experimental and numerical outcomes for the single lap joint indicate that material properties (parameters) employed for cohesive zone modeling, element types (C3D8R and COH3D8), and element sizes are applicable for butt joint analysis as well. Furthermore, several studies [21,22,29] have also noted a strong compatibility between experimental and numerical results.

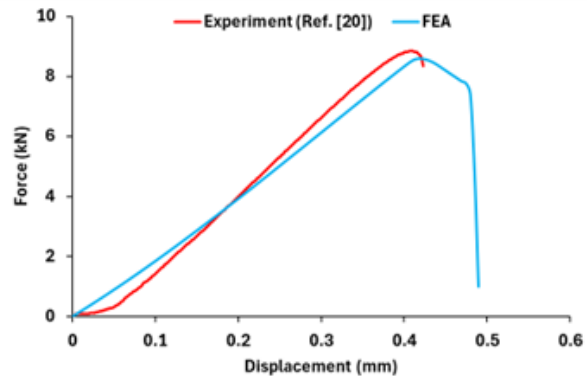


Figure 4 Verification of numerical model

RESULTS AND DISCUSSIONS

Effect of Defect Presence and Defect Volume Fraction

Force-displacement curves for various defect volume fractions in the bonding layer are presented in Fig. 5. As shown, force-displacement curves have three linear sections. In the first section, the force exhibits a linear increase until it reaches the peak load, indicating the adhesive's elastic behavior. Subsequently, in the following section, the force linearly decreases, corresponding to the damage evolution and softening behavior of the adhesive. In the third section, there is a rapid decline in the force, corresponding to abrupt complete failure. It is clear from Fig. 5 that the elasticity of the adhesively bonded butt joint remains unaffected by the presence of defects. This provides evidence that the elasticity of the butt joint is primarily governed by the elasticity of the adherend. Because adhesive's elasticity (2077 MPa) is notably lower in comparison to that of the adherend (72400 MPa).

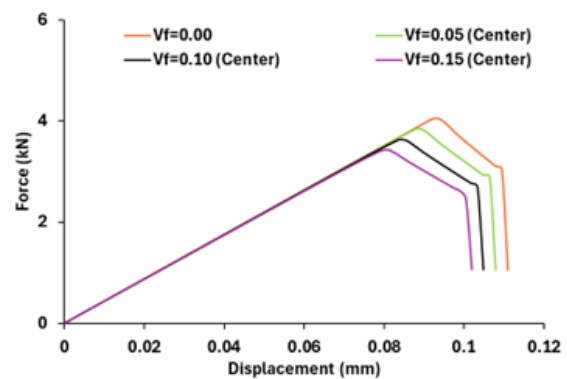


Figure 5 Force-displacement curves for various defect volume fractions

Fig. 6 illustrates the variation in load-bearing capacity (peak force) and displacement at peak force in relation to changes in defect volume fraction. The detrimental impact of defects on the load-bearing capability of the butt joint is evident. With an increment in defect volume fraction, both the peak load and displacement at peak load decrease linearly. The introduction of a square defect at the center of the bonding layer, with volume fractions of 0.05, 0.10, and 0.15, results in peak force reductions of 4.08%, 10.56%, and 15.73%, respectively. Correspondingly, displacement at peak force decreases by 4.84%, 9.68%, and 12.91% for the same defect volume fractions. Decrease in peak load can be attributed to the decrease in bonded area. Heidarpour et al. [8] also reported a strength reduction in SLJ with the rise of 2D/3D defect size. Furthermore, according to Kumar [30], the interlaminar tensile (ILT) strength and mode-I delamination fracture energy show a linear correlation with the flaw area fraction on a critical fracture plane.

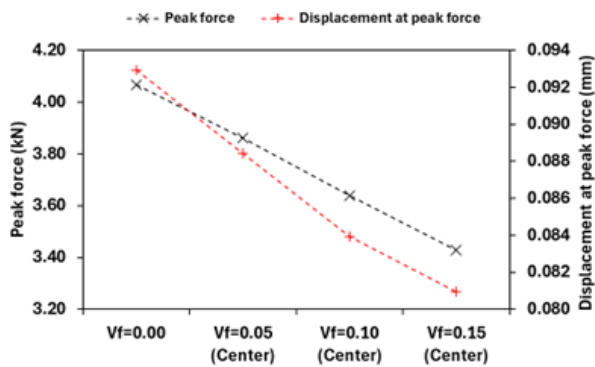


Figure 6 Variation of peak force and displacement at peak force with the change of defect volume fraction

Fig. 7 illustrates the von Mises stress distribution along the A-B route for various defect volume fractions within the adhesive layer under a 3 kN load. Overall, there's a nonlinear increase in von Mises stress as the defect edge is approached, particularly with a sharper rise near the defect edge. The existence of a defect at the center of the adhesive layer results in approximately 31% rise in the maximum von Mises stress. Moreover, the von Mises stress at the defect edges, where the largest von Mises stress occurs, is unaffected by changes in the defect volume fractions. However, the rise of defect volume fraction results in an increase in von Mises stress at the bonding layer edges. Fig. 8 depicts the contour of von Mises stress distribution on the adhesive layer for various defect volume fractions. It is evident that as the defect volume fraction increases, the stress concentration near the defect edges becomes more severe and spreads over a larger area. Hence, the early failure of the adhesive is concentrated near the edges of the flaw as seen in Fig. 8. Conversely, in the absence of defects in the bonding layer, the initial degradation of the adhesive occurs abruptly and uniformly throughout the whole adhesive layer. Therefore, failure of adhesive layer without defect cannot be illustrated in Fig. 8.

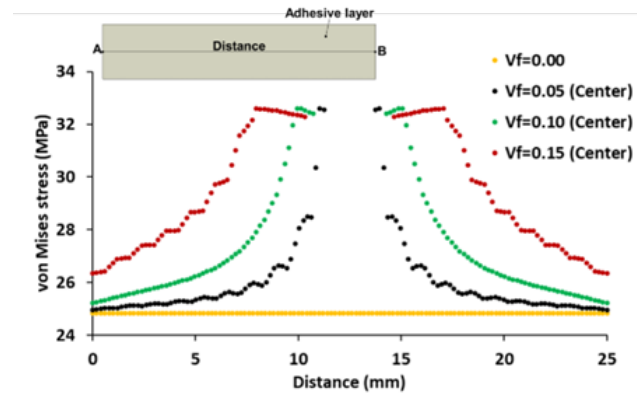


Figure 7 von Mises stress distribution along the path A-B for various defect volume fractions in the adhesive layer

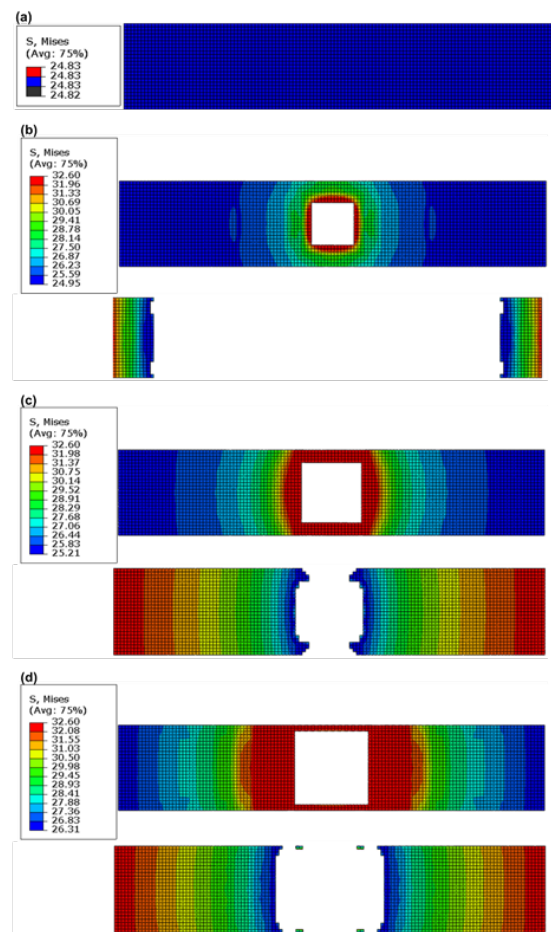


Figure 8 Contour of von Mises stress distribution on the bonding layer and adhesive layer initial failure for (a) Vf=0.00, (b) Vf=0.05, (c) Vf=0.10, and (d) Vf=0.15

Effect of Defect Location

Force-displacement curves for the butt joints with a square defect positioned at various locations within the adhesive layer are illustrated in Fig. 9. Defect location is plays crucial role in the damage evolution and softening characteristics of the adhesive. Relocating the defect from the center to the left

side of the bonding layer causes a drop in the slope of the second section of the curve, indicating nearly constant-force damage evolution. However, repositioning the defect towards the upper side of the adhesive layer has little to no discernible effect on the force-displacement curve. This is probably due to the limited upward shifting capacity of the defect owing to the geometry of the butt joint.

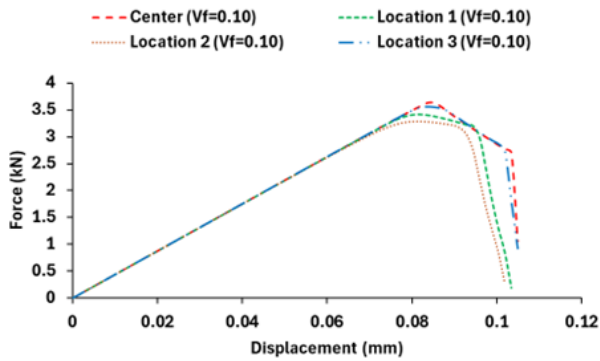


Figure 9 Force-displacement curves for various defect locations

The change of peak load and displacement at peak load depending on defect location are shown in Fig. 10. Moving the defect from the center to the left side of the bonding layer causes a drop in peak force. Specifically, shifting the defect from the center to Location 1 and Location 2 results in reductions of 6.00% and 9.79% at peak force, respectively. It is evident that defects positioned near the edges of the adhesive layer present a greater risk to the durability of butt joints. Moreover, relocating the flaw from the center to Location 3 leads to a decrease of 2.27% in the load-bearing capacity of the butt joint. These changes in the load-bearing capacity of butt joints can be attributed to the disruption of the symmetry of the bonding layer with the shifting of the flaw. Ribeiro et al. [31] carried out a numerical work to assess the influence of defects on SLJ strength. Their findings indicated that flaws close to the joint end result in a more pronounced strength drop compared to defects at the center of the joint. Chu et al. [5] similarly observed this trend, aligning with Ribeiro et al. [31], particularly for balanced SLJs constructed with identical adherends. However, it's noteworthy that the location of defects on each side of the center has different impacts on the durability of unbalanced SLJs constructed with different adherends. On the other hand, repositioning the defect from the center to Location 1 results in a 3.75% decrease in displacement at peak force, while moving it from Location 1 to Location 3 shows no impact on displacement at peak force. Furthermore, displacement at peak force remains unchanged when the defect is shifted from the center to Location 3.

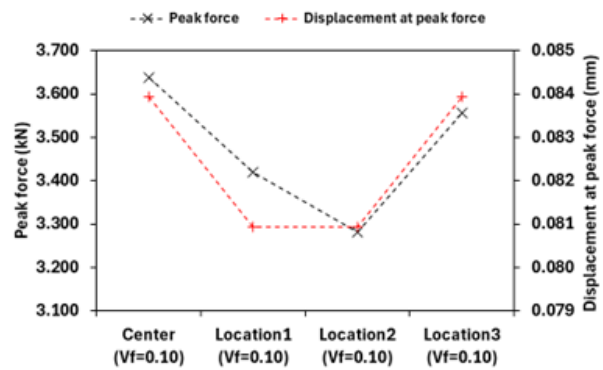


Figure 10 Variation of peak load and displacement at peak load with the change of defect location

Fig. 11 depicts the von Mises stress distribution along the A-B route for various defect positions within the adhesive layer for the case of 3 kN loading. There is no change in the von Mises stress distribution when the defect is moved to upper side of the bonding layer. However, as the defect is shifted from the center to the left side, von Mises stress at the left side of the bonding layer rises whereas von Mises stress at the right side of the bonding layer drops. At the left edge of the adhesive, there is an increase of 11.81% and 25.19% for Location 1 and Location 2, respectively, while experiencing a decrease of 4.56% and 20.64%, respectively, at the right edge. Regarding the maximum von Mises stress, altering the defect location does not affect its value. Von Mises stress fields on the adhesive layer for various defect positions are illustrated in Fig. 12. Stress concentrations occur at the edges of the defects, as evidenced by Fig. 12. Moreover, as the flaw is moved from the center to the left side, the stress concentration near the defect edges becomes more severe and spreads over a larger area. The adhesive failure starts at the left edge of the bonding layer, correlating with repositioning the defect towards the left side, as depicted in Fig. 12. Similarly, relocating the defect to the upper side leads to the onset of adhesive failure at the upper edge of the bonding layer.

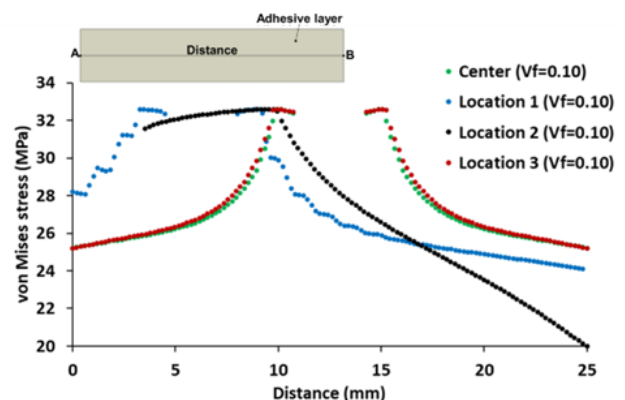


Figure 11 von Mises stress distribution along the path A-B for various defect locations in the adhesive layer

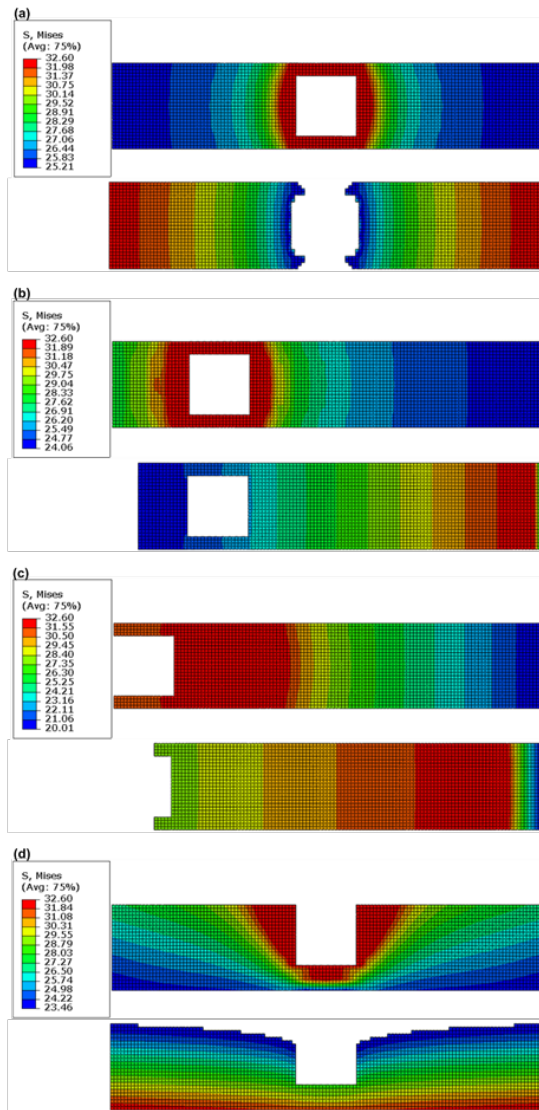


Figure 12 Contour of von Mises stress distribution and adhesive failure on the bonding layer for various defect locations (a) Center ($V_f=0.10$), (b) Location 1 ($V_f=0.10$), (c) Location 2 ($V_f=0.10$), and (d) Location 3 ($V_f=0.10$)

Effect of Defect Random Distribution

Fig. 13 displays the force-displacement curves and peak load and displacement at peak load for the butt joints with a defect located at the center of the bonding layer and defects randomly distributed in the adhesive layer. It is evident that the random distribution of defects does not exert any discernible influence on the durability of butt joints. The random distribution of flaws creates approximately equal defect areas on both sides of the symmetry planes (XY and XZ planes). Consequently, an adhesive layer with an almost symmetrical structure is formed. This roughly symmetrical structure explains why the load-bearing capacity remains unchanged.

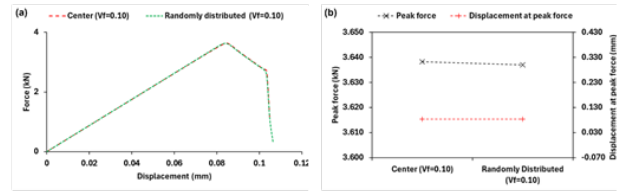


Figure 13 (a) Force-displacement curves and (b) peak load and displacement at peak load for the butt joints containing a defect at the center of the bonding layer and defects randomly distributed in the bonding layer

Fig. 14 depicts the von Mises stress distribution on the bonding layer under a 3 kN loading condition, considering the presence of randomly distributed defects. Localized stress concentrations arise at the edges of defects, and adhesive damage begins in the area where the defects are concentrated.

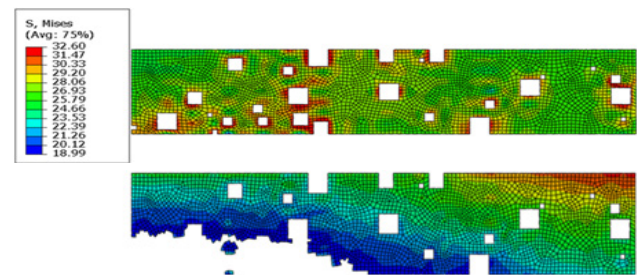


Figure 14 Contour of von Mises stress distribution and adhesive failure on the bonding layer with randomly distributed defects

CONCLUSION

This study scrutinizes the influence of defect presence, defect volume fraction, defect location, and random distribution of defects in the bonding layer on the load-carrying capacity of the butt joint. A FE model in Abaqus/Standard was created and the butt joint was exposed to uniaxial tensile load while exclusively considering only cohesive failure. Defect presence has a great effect on the durability of the butt joint. Increasing the defect volume fraction within the adhesive layer causes a reduction in both peak force and displacement at peak force. Every 5% increment in defect volume fraction in adhesive layer causes a 5% drop in load-bearing capacity of the butt joint. As the defect volume fraction increases, stress concentration near the defect edges becomes more pronounced and extends over a wider region. Therefore, adhesive failure first initiates at the defect edges. Regarding the defect location, shifting the defect from the center to the left side of the bonding layer causes a reduction in peak load and displacement at peak load and the onset of the adhesive failure at the left edge of the adhesive. However, both peak force and displacement at peak force do not alter as the defect is moved to the upper side of the adhesive. The load-carrying capability of butt joints remains unaffected by the random distribution of flaws in the adhesive layer. Considering the widespread use of adhesively bonded joints, the findings of this study significantly contribute to the current knowledge. The results obtained can be utilized by researchers and industry professionals across a broad range of sectors, from automotive to aerospace.

Acknowledgement

The author received no financial support for the research, authorship, and/or publication of this article.

References

- Moya-Sanz EM, Ivañez I, Garcia-Castillo SK. Effect of the geometry in the strength of single-lap adhesive joints of composite laminates under uniaxial tensile load. *Int J Adhes Adhes*. 2017;72:23–9.
- Shishesaz M, Hosseini M. Effects of joint geometry and material on stress distribution, strength and failure of bonded composite joints: an overview. *J Adhes*. 2020;96:1053–121.
- Geleta TN, Woo K, Cairns DS, Samborsky D. Failure behavior of inclined thick adhesive joints with manufacturing defect. *J Mech Sci Technol*. 2018;32:2173–82.
- Sadeghi MZ, Gabener A, Zimmermann J, Saravana K, Weiland J, Reisinger U, et al. Failure load prediction of adhesively bonded single lap joints by using various FEM techniques. *Int J Adhes Adhes*. 2020;97:102493.
- Chu Y, Sun L, Zhan B, Yang X, Zhang C, Huang W. Static and dynamic behavior of unbalanced bonded joints with adhesion defects in automotive structures. *Compos Struct*. 2019;226:111234.
- Shang X, Marques EAS, Machado JJM, Carbas RJC, Jiang D, da Silva LFM. Review on techniques to improve the strength of adhesive joints with composite adherends. *Compos Part B Eng*. 2019;177:107363.
- Rocha RJB, Campilho RDSG. Detailed investigation of the analysis conditions in the evaluation of bonded joints by cohesive zone models. *J Phys Conf Ser*. 2017;843:012002.
- Heidarpour F, Farahani M, Ghabazi P. Experimental investigation of the effects of adhesive defects on the single lap joint strength. *Int J Adhes Adhes*. 2018;80:128–32.
- Guo W, Chen P, Yu L, Peng G, Zhao Y, Gao F. Numerical analysis of the strength and interfacial behaviour of adhesively bonded joints with varying bondline thicknesses. *Int J Adhes Adhes*. 2020;98:102553.
- Kanani AY, Hou X, Laidlaw R, Ye J. The effect of joint configuration on the strength and stress distributions of dissimilar adhesively bonded joints. *Eng Struct*. 2021;226:111322.
- Elhannani M, Madani K, Chama Z, Legrand E, Touzain S, Feaugas X. Influence of the presence of defects on the adhesive layer for the single-lap bonded joint—Part II: Probabilistic assessment of the critical state. *Aerosp Sci Technol*. 2017;63:372–86.
- Majid J-O, Mohammad Reza MS. Investigation of Defect Effects on Adhesively Bonded Joint Strength Using Cohesive Zone Modeling. *Strojnícky Cas – J Mech Eng*. 2018;68:5–24.
- Luo G, Chai C, Liu J, Xiao Y, Chen Y, Xu F. Investigations on the Mechanical Properties of Composite T-Joints with Defects under Bending Loading. *Sustainability*. 2022;14:16609.
- Xu W, Wei Y. Strength analysis of metallic bonded joints containing defects. *Comput Mater Sci*. 2012;53:444–50.
- Elhannani M, Madani K, Legrand E, Touzain S, Feaugas X. Numerical analysis of the effect of the presence, number and shape of bonding defect on the shear stresses distribution in an adhesive layer for the single-lap bonded joint; Part I. *Aerosp Sci Technol*. 2017;62:122–35.
- Dai T, Yang Y, Dai H-L, Hu Z. Interfacial stress analysis of a CFRR-metal adhesively bonded joint with/without defect under hygrothermal environment. *Appl Math Model*. 2019;67:357–77.
- Fame CM, Wu C, Feng P, Tam L. Numerical investigations on the damage tolerance of adhesively bonded pultruded GFRP joints with adhesion defects. *Compos Struct*. 2022;301:116223.
- Kumar RS. Mode-II interlaminar fracture of composite materials in the presence of randomly distributed defects. *Int J Fract*. 2021;231:201–21.
- Ribeiro FMF, Campilho RDSG, Carbas RJC, da Silva LFM. Strength and damage growth in composite bonded joints with defects. *Compos Part B Eng*. 2016;100:91–100.
- Sahin R, Akpınar S. The effects of adherend thickness on the fatigue strength of adhesively bonded single-lap joints. *Int J Adhes Adhes*. 2021;107:102845.
- Çalık A, Yıldırım S. An investigation on the effect of parallel slot in bi-adhesive single lap joints with spew fillet. *J Eng Res*. 2015;3:36.
- Çalık A, Akpınar S. Dört Nokta Eğme Yüküne Maruz Yapıştırma Bağlantılarında İç Kademenin Bağlantı Hasar Yüküne Etkisi: Deneysel ve Sayısal Analiz. *Osman Korkut Ata Üniversitesi Fen Bilim Enstitüsü Derg*. 2022;5:1128–40.
- Liao L, Huang C, Sawa T. Effect of adhesive thickness, adhesive type and scarf angle on the mechanical properties of scarf adhesive joints. *Int J Solids Struct*. 2013;50:4333–40.
- Chen P, Guo W, Zhao Y, Li E, Yang Y, Liu H. Numerical analysis of the strength and interfacial properties of adhesive joints with graded adherends. *Int J Adhes Adhes*. 2019;90:88–96.
- Liao L, Huang C. Numerical analysis of effects of adhesive type and geometry on mixed-mode failure of adhesive joint. *Int J Adhes Adhes*. 2016;68:389–96.
- Benzeggagh ML, Kenane M. Measurement of mixed-mode delamination fracture toughness of unidirectional glass/epoxy composites with mixed-mode bending apparatus. *Compos Sci Technol*. 1996;56:439–49.
- Kanar B, Akpınar S, Avinc Akpınar I, Akbulut H, Ozel A. The fracture behaviour of nanostructure added adhesives under ambient temperature and thermal cyclic conditions. *Theor Appl Fract Mech*. 2018;97:120–30.
- Kazaz I, Akpınar S, Ozel A. The effects of thermal cycle and nanostructure reinforcement on the shear load in adhesively bonded joints. *Mech Adv Mater Struct*. 2020;27:1627–38.
- Akpınar S, Çalık A. Dört Noktalı Eğme Testi Altında Yapıştırıcı ile Birleştirilmiş Bindirme Bağlantısının Deneysel ve Sonlu Elemanlar Analizi. *Çukurova Üniversitesi Mühendis Fakültesi Derg*. 2021;36:649–57.
- Kumar RS. Effects of randomly distributed defects on Mode-I interlaminar fracture of composite materials. *Eng Fract Mech*. 2021;248:107699.
- Ribeiro FL, Borges L, d'Almeida JRM. Numerical stress analysis of carbon-fibre-reinforced epoxy composite single-lap joints. *Int J Adhes Adhes*. 2011;31:331–7.

HITTITE JOURNAL OF SCIENCE AND ENGINEERING

e-ISSN: 2148-4171
Volume: 11 • Number: 3
September 2024

Preliminary Results on Deformations of the Central North Anatolian Fault Zone

Kayhan Aladoğan¹ | Mehmet Nurullah Alkan¹ | İbrahim Tiryakioğlu²
Hasan Hakan Yavaşoğlu³ | Halil İbrahim Solak⁴ | Cemil Gezgin⁵ | Ali Özkan⁶
Eda Esmâ Eyübagil² | Furkan Şahiner² | Ece Bengünaz Çakanşimşek² | Zafer Köse⁷

¹Hitit University, Osmaniye Ömer Derindere Vocational High School, 19500, Osmaniye, Çorum, Türkiye.

²Afyon Kocatepe University, Department of Geomatics Engineering, 03200, Afyonkarahisar, Türkiye.

³Istanbul Technical University, Department of Geomatics Engineering, 34467, Istanbul, Türkiye.

⁴Afyon Kocatepe University, Distance Education Vocational School, 03200, Afyonkarahisar, Türkiye.

⁵Aksaray University, Department of Geomatics Engineering, 68100, Aksaray, Türkiye.

⁶Osmaniye Korkut Ata University, Osmaniye Vocational High School, 80000, Osmaniye, Türkiye.

⁷Burdur Mehmet Akif Ersoy University, Gölhisar Vocational High School, 15400, Gölhisar, Burdur, Türkiye.

Corresponding Author

Mehmet Nurullah Alkan

E-mail: nurullahalkan@hitit.edu.tr Phone: +90 530 511 56 69

RORID¹: <https://ror.org/01x8m3269> RORID²: <https://ror.org/03a1crh56> RORID³: <https://ror.org/059636586>

RORID⁴: <https://ror.org/03a1crh56> RORID⁵: <https://ror.org/026db3d50> RORID⁶: <https://ror.org/03h8sa373>

Article Information

Article Type: Research Article

Doi: <https://doi.org/10.17350/HJSE19030000338>

Received: 01.04.2024

Accepted: 13.07.2024

Published: 30.09.2024

Cite As

Aladoğan, K., et al. Preliminary Results on Deformations of the Central North Anatolian Fault Zone. Hittite J Sci Eng. 2024;11(3):115-122.

Peer Review: Evaluated by independent reviewers working in at least two different institutions appointed by the field editor.

Ethical Statement: Not available.

Plagiarism Checks: Yes - iThenticate

Conflict of Interest: Authors approve that to the best of their knowledge, there is not any conflict of interest or common interest with an institution/organization or a person that may affect the review process of the paper.

CRedit AUTHOR STATEMENT

Kayhan Aladoğan: Conceptualization, Methodology, Software, Validation, Writing- original draft. **Mehmet Nurullah Alkan:** Data curation, Visualization, Investigation. **İbrahim Tiryakioğlu:** Supervision, Data curation, Writing- review and editing, Investigation. **Other Authors:** Data curation, Investigation.

Copyright & License: Authors publishing with the journal retain the copyright of their work licensed under CC BY-NC 4.

Preliminary Results on Deformations of the Central North Anatolian Fault Zone

Kayhan Aladoğan¹ | Mehmet Nurullah Alkan¹ | İbrahim Tiryakioğlu² | Hasan Hakan Yavaşoğlu³ | Halil İbrahim Solak⁴ | Cemil Gezgin⁵ | Ali Özkan⁶ | Eda Esma Eyübagil² | Furkan Şahiner² | Ece Bengünaz Çakanşimşek² | Zafer Köse⁷

¹Hittit University, Osmancık Ömer Derindere Vocational High School, 19500, Osmancık, Çorum, Türkiye.

²Afyon Kocatepe University, Department of Geomatics Engineering, 03200, Afyonkarahisar, Türkiye.

³Istanbul Technical University, Department of Geomatics Engineering, 34467, Istanbul, Türkiye.

⁴Afyon Kocatepe University, Distance Education Vocational School, 03200, Afyonkarahisar, Türkiye.

⁵Aksaray University, Department of Geomatics Engineering, 68100, Aksaray, Türkiye.

⁶Osmaniye Korkut Ata University, Osmaniye Vocational High School, 80000, Osmaniye, Türkiye.

⁷Burdur Mehmet Akif Ersoy University, Gölhisar Vocational High School, 15400, Gölhisar, Burdur, Türkiye.

Abstract

The North Anatolian Fault Zone (NAFZ) in the north of Türkiye is considered one of the most active faults on earth and have caused many major earthquakes in the last century. Surface ruptures by those earthquakes indicate that this tectonic feature consists of many segments, which reveal different characteristics in terms of geometry and mechanism. NAFZ lies along between Bingöl in the eastern Turkey and Saros Gulf in the west. This study focuses on the central part of the NAFZ between Niksar and Iğaz provinces. In addition to the main branch, the central section of the NAFZ also contains two sub-branches extending southward: Merzifon-Esençay and Sungurlu Faults. In the literature, there are several studies for the region, however a comprehensive study mainly focusing on the main branch of the NAFZ and its sub-branches along the central NAFZ has not been conducted yet, which would fully reveal the fault mechanism and seismic potential in the region. The aim of this study is to derive an up-to-date high-spa-tial-resolution Global Navigation Satellite Systems (GNSS) velocity field for the central NAFZ and to correlate with the strain accumulations along the faults. Based on this, a high-spatial-resolution GNSS network consisting of 60 sites was established enclosing the central NAFZ. The previously archived GNSS data for the same observation sites were collected from the different studies in the region and a new GNSS campaign measurement was conducted between October 2023 and February 2024. All GNSS data were processed using GAMIT/GLOBK software, and the results indicate the GNSS velocities ranging from 3-30 mm/year and their associated uncertainties of maximum ± 1.5 mm/year with respect to the Eurasian tectonic plate.

Keywords: NAFZ, earthquake, GNSS velocity field, GAMIT/GLOBK, Sungurlu Fault, Merzifon-Esençay Fault.

INTRODUCTION

Türkiye is a part of highly active seismic region, which extends from Gibraltar to Indonesia and is referred as “Alpine-Himalayan Belt” (Jackson and McKenzie, 1984). So as, the potential seismic hazard in Türkiye revealed recently in the districts of Kahramanmaraş (Pazarcık and Elbistan) with the earthquakes of their magnitude Mw 7.8 (01.17 UTC) and Mw 7.6 (10.24 UTC Time) on February 06, 2023, respectively (AFAD 2023, KOERİ 2023).

The tectonic motion in Türkiye is mainly accommodated along the major active faults by three tectonic plates namely Eurasia, Arabia and Anatolia. Specifically, the Anatolian plate is located among the Arabian and African plates at the south and Eurasian plate at the north. Due to the northward motion of the southern plates towards to the relatively stable Eurasia plate, the Anatolian plate hosts a westward movement and substantial fault systems with different regimes (Figure 1) (Emre et al.2018). These fault systems have witnessed many major earthquakes in the recent past, and the North Anatolian Fault Zone (NAFZ) have made its mark at most among of the active faults in the region in terms of seismic events. The NAFZ extends from Karlıova, Bingöl at the eastern edge to the Saroz Gulf, Aegean Sea at the western terminal, passing through many provinces between Erzincan and Kocaeli, and continues beneath the Marmara Sea to Şarköy, Tekirdağ (Şengör et al. 2005, Yavaşoğlu et al. 2020). NAFZ has mainly a right-lateral strike-slip fault mechanism ranging between 0.4 mm–1 m with an accompanying dip-slip component (Ketin 1969, Şengör et al. 2005).

The major earthquakes along the NAFZ during the instrumental period, such as 1939 Erzincan (M_s 7.9), 1942 Niksar – Erbaa (M_s 7.0), 1943 Ladik – Tosya (M_s 7.2), 1944 Bolu – Gerede (M_s 7.4), 1999 Izmit (Mw 7.4) and Düzce (Mw 7.2), indicate that this fault mechanism is tectonically active (Barka 1996, Takcı 2015, Bohnhoff et al. 2016). The paleosismological and geological studies have also a consensus about the

same conclusion (Ambraseys and Finkel, 1995). Considering the surface ruptures and distribution of the epicentres of the instrumental earthquakes in the last century, the NAFZ consists of 10 segments, some of which are longer and have different geometry and characteristics (Barka and Kandinsky-Cade 1988, Barka 1992, Barka 1996, Köksal 2011, Emre et al. 2018) (Figure 2). There are three main segments of the NAFZ ranging from 150 to 350 km in length: the Erzincan Segment (ruptured in 1939), the Ladik-Tosya Segment (ruptured in 1943), and the Gerede Segment (ruptured in 1944). There are also minor segments at the eastern and western terminals of those major segments, which are shorter than 10 km (Barka and Kandinsky-Cade 1988, Barka 1996, Şengör et al. 2005, Köksal 2011, Emre et al. 2018).

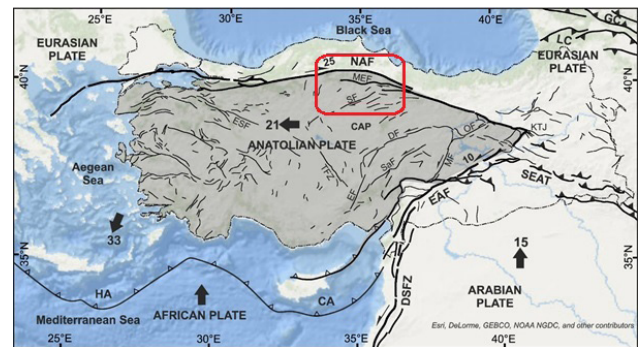


Figure 1 Active fault mapping for the East-Mediterranean (after Emre et al. 2018). (CA) Cyprian Arc, (HA) Hellenic Arc, (EAFZ) East Anatolian Fault Zone, (DSFZ) Dead Sea Fault Zone, (NAFZ) North Anatolian Fault Zone, (SEATZ) Southeast Anatolian Thrust Zone, (LC) Lesser Caucasus, (GC) Great Caucasus, (ESF) Eskişehir Fault, (TFZ) Tuzgölü Fault, (MEF) Merzifon-Esençay Fault, (SF) Sungurlu Fault, (EF) Ecemiş Fault, (DF) Deliler Fault, (SaF) Sarız Fault, (MF) Malatya Fault, (OF) Ovacık Fault. Thick lines within solid triangles indicate contractional tectonic regimes. Thick black arrows show the direction of plate movements and associated plate velocity. Red rectangle represents the study area.

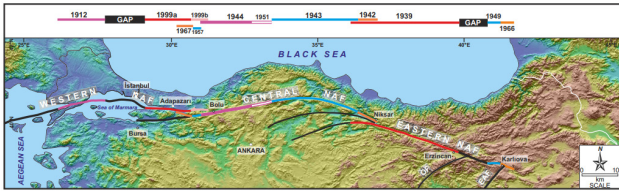


Figure 2 The major segments of the NAFZ and instrumental period earthquakes with $M_s > 6.8$, since 1912 (Emre et al. 2021).

The NAFZ has two sub-branches NE-SW oriented towards to the south at the central section, which these are entitled Ezinepazarı-Sungurlu and Merzifon-Esençay fault segments. The tectonic zone between these fault segments have had significant deformation during the neotectonic period (Erturac M. K. and Tuysuz O., 2012). The southern branch, Ezinepazarı-Sungurlu Fault, stretches out westward while delineating the Amasya-Aydınca Basin and Amasya-Deliçay Valley, and approaches to the south of Sungurlu province and the north of Mecitözü (Gökhöyük Fault) (Yavaşoğlu et al. 2011, Emre et al. 2018) (Figure 3). The geological structures and morphological features on the surface topography exhibit distinct characteristics correlated with the fault extension (Şaroğlu et al. 1987). The most interesting event along the fault zone is the Erzincan earthquake (1939, M_s 7.9). The surface ruptures of the earthquake reveal the potential of the probable activities in the fault system (Ketin 1969, Şaroğlu et al. 1987, Barka 1996), however the seismic data in the instrumental period were limited for the Geldingen Basin and the western parts, which is also known as Sungurlu Fault. The lack of a distinct seismic network and scientific studies in the region leads to a weak understanding about the tectonic mechanism (Amasya İRAP Report, 2021, Çorum İRAP Report, 2021).

The northern branch, called Merzifon - Esençay Fault, is an ESE-WNW oriented right-lateral strike-slip fault that lies almost parallel to the main branch of the NAFZ and extends to the north of the İskilip Province of Çorum (Erturac and Tuysuz 2010). The paleoseismological studies along the fault indicate that the earthquake recurrence interval ranges between 1320 and 2200 years during the Holocene period, with an interseismic cycle about 3700 years (Emre et al. 2020). According to the records about the historical and instrumental events along this fault, which lack seismic data, it is one of the unruptured segments of the NAFZ in the last century (Emre et al. 2020). Empirical evaluations for the region indicate an earthquake with a magnitude of ~7.2 (Wells and Coppersmith, 1994). Additionally, the fault segments surrounding have also been reported about the similar risk of a probable earthquake (Emre et al. 2018). Besides, there are several blocks bounded by the main branch of the NAFZ and its southern branches (Yavaşoğlu et al. 2011) (Figure 3).

Synthetic Aperture Radar-InSAR techniques), geology (field observations and paleoseismology studies), geophysics (gravimetry and seismic refraction techniques), satellite imaging and geographical information systems analyses (Stein and Wyession 2003, Lay and Wallace 1995, Herring 1999, Yavaşoğlu et al. 2011, Massonnet and Feigl 1998, Michetti et al. 2005, , McCalpin and Nelson 1996, Kaiser et al. 2009,

Özalaybey et al. 2009). The geodetic techniques, which are very useful in such cases and economically efficient, serve for precise positioning in a short period of time by terrestrial networks, GNSS, InSAR, Light Detection and Ranging (LIDAR). (Massonnet and Feigl 1998, Herring 1999, Schowengerdt 2007, Yavaşoğlu et al. 2011, Ghilani and Wolf 2012, Solak et al. 2024). The recent geodetic studies focusing on the tectonically active regions demonstrate the power of new generation of geodetic techniques (Yavaşoğlu 2009, Tiryakioğlu 2012, Solak 2020, Özkan 2021). In order to reveal the strain accumulations along the faults, the GNSS networks consisting of periodically observed sites and permanent stations are established considering the fault geometry in the study region. Thanks to velocity field derived from GNSS observations, we are able to estimate the potential magnitude and location of a probable major earthquake and also average recurrence intervals for large earthquakes, apart from the exact time of a seismic event (McClusky et al., 2000; Reilinger et al., 2006; Aktuğ et al., 2009; Yavaşoğlu et al., 2011; Tiryakioğlu 2012; Aktuğ 2017; Poyraz et al., 2018; Tiryakioğlu et al., 2018, 2019; Akyar 2020, Solak 2020, Yıldız et al. 2020; Eyübagil et al. 2021, Gezgin et al. 2022, Özkan et al., 2023).

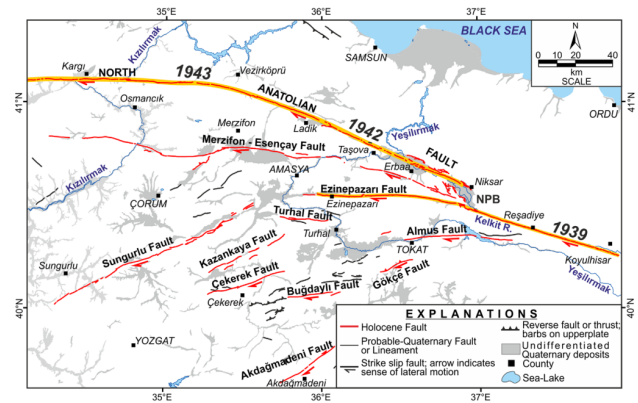


Figure 3 The detailed geological map of the study area (Emre et al. 2021).

The tectonic movements and lithospheric crustal deformations causing earthquakes are studied by different disciplines using several techniques, such as seismology (seismic array networks), geodesy (GNSS and Interferometric

In this study, the interseismic lithospheric deformations are investigated at the central part of the NAFZ (Figure 3). There are several blocks bounded by the main branch of the North Anatolian Fault Zone (NAFZ) and its sub-branches extending southward in the region. In order to model the plate motions and so as minor blocks in the region using a high-spatial-resolution geodetic dataset, a wide GNSS network consisting of 60 sites was established, and the GNSS data for the same observation sites previously archived were obtained from the different studies. In addition to permanent GNSS stations in the study region, the GNSS observations were periodically performed at each survey site in the network during campaign measurement sessions between 2023 and 2024. Thus, the latest velocity field with respect to Eurasian tectonic plate was derived from present-day GNSS observations. Since it is expected to have more comprehensive findings

and conclusions to better understand the complex tectonic mechanism of the mid-section of the NAFZ through our ongoing studies, we initially have the goal to provide the preliminary results of our geodetic observations here in this study.

MATERIAL AND METHODS

The GNSS Network and Observations

Due to complex tectonic structure, scattered topography, and challenges with the observation techniques, there are only few studies for the study region in the literature (Yavařoĝlu et al. 2011, Aktuř et al. 2015, Kurt et al. 2022). The GNSS observation sites used in the Yavařoĝlu et al. (2011) was also integrated into our GNSS network design within the scope of this study. However, the most of the sites from that study have not been observed since 2004. Therefore, the long-term repeatability of the GNSS observations is crucial to derive latest velocity field and so as to precisely constrain the strain accumulations along the faults around the mid-section of the NAFZ. In order to investigate on the geological features and regional tectonic setting, the GNSS network established within this study has fault-perpendicular profiles around the main branch of the NAFZ and its southward sub-branches, including Merzifon–Esençay and Ezinepazarı–Sungurlu fault segments. The GNSS network for this study consists of 45 sites from the study of Yavařoĝlu et al. (2011) and also from the TUTGA network, different institutions and organizations. The remaining 15 sites out of 60 are the permanent stations that belong to the Turkish National Permanent GNSS Network-Active (TUSAGA-Active) (Figure 4).

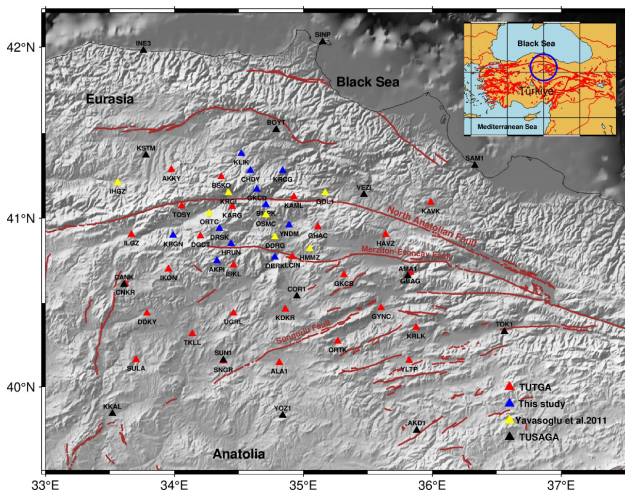


Figure 4 The GNSS observation network established for this study. Red lines represent the fault traces of the main branch of the NAFZ and its sub-branches. New sites represented in blue in this study have archive GNSS data from previous local studies in the region. Stations represented as triangles in the figure (red: Turkish National Fundamental GNSS Network (TUTGA) sites, yellow: sites from Yavařoĝlu et al. 2011, black: TUSAGA-Active stations, blue: this study).

Apart from the permanent stations within our network, the GNSS observations at the survey sites were performed during the campaign measurements between October 2023 and February 2024, having at least 8-h session lengths on two consecutive days and using 15-s measurement interval at

each site. 40 point in the network are selected from pillars and 5 of them are bronze mast on the bedrock. In order to eliminate the deficiencies of observer and minimize the probable meteorological factors disturbing the observations, the fixed-height GNSS masts were used at the sites on the bedrock (Figure 5).



Figure 5 The GNSS sites periodically observed within the network named KAML (left), KARG (center), DRSK (right).

The archived dataset of previously observed TUTGA sites were gathered from the General Directorate of Mapping (HGM) according to the “Inter-institutional Collaboration and Data Distribution Protocol”. Moreover, the GNSS observation files logged in Receiver Independent Exchange (RINEX) data format at the permanent stations belong to TUSAGA-Active network were downloaded from the official website of the General Directorate of Land Registry and Cadastre (TKGM).

GNSS Data Processing

In this study, the GAMIT/GLOBK software developed by the Massachusetts Institute of Technology (MIT) was used for GNSS data processing (Herring et al. 2018). The GAMIT module is capable of parameter estimations such as station coordinates, satellite orbits, Earth Orientation Parameters (EOPs) and atmospheric delays using ionosphere-free linear combination of GNSS phase observables with the help of double-differencing technique. This module also can eliminate cycle slips for the GNSS observations at each site. In the second stage, the GLOBK module combines all the loosely-constrained daily GAMIT solutions using Kalman-Filtering approach and estimates the velocities and positions of the observation sites defined in a terrestrial reference frame (Herring et al. 2018). The short-term (daily) position repeatability plots were generated using the GNSS data from the consecutive days to reveal the possible centering errors, and the long-term (annual) position time series were produced to determine the trend of the motion for all the sites in the network (Figure 6, 7).

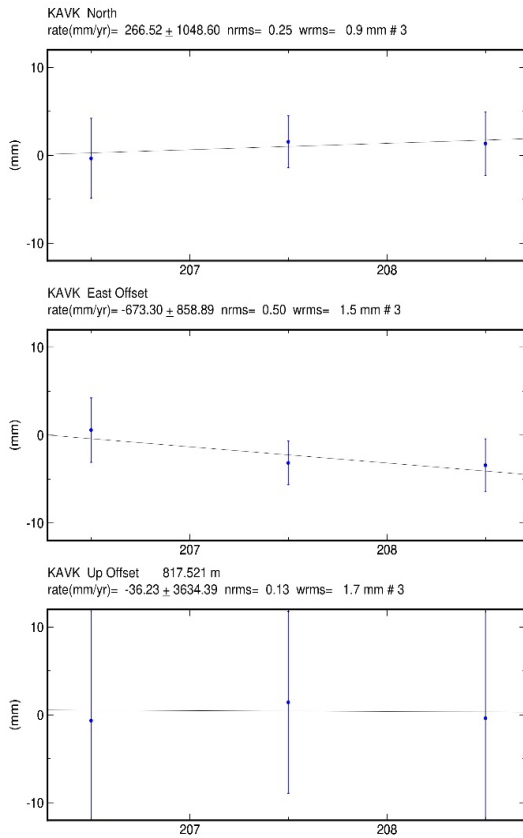


Figure 6 The plot of short-term (daily) position repeatability for the KAVK station (the north, east and up components are in order from top to bottom, respectively).

Table 1 The list of IGS stations used in the stabilization process.

S.N.	Station Name	Longitude	Latitude	S.N.	Station Name	Longitude	Latitude
1	ADIS	38.77	9.04	14	MATE	16.70	40.65
2	ANKR	32.76	39.89	15	NICO	33.40	35.14
3	BAHR	50.61	26.21	16	NOT1	14.99	36.88
4	BAKU	49.81	40.37	17	NSSP	44.50	40.23
5	BOR1	17.07	52.28	18	ONSA	11.93	57.40
6	BUCU	26.13	44.46	19	POLV	34.54	49.60
7	CRAO	33.99	44.41	20	POTS	13.07	52.38
8	DRAG	35.39	31.59	21	RAMO	34.76	30.60
9	GLSV	30.50	50.36	22	SOFI	23.39	42.56
10	GRAS	6.92	43.75	23	TELA	34.78	32.07
11	GRAZ	15.49	47.07	24	VILL	356.05	40.44
12	KOSG	5.81	52.18	25	WTZR	12.88	49.14
13	KUWT	47.97	29.33	26	ZECK	41.57	43.79

Following the generation of the position time series, the next step includes the stabilization of the network and the estimation site velocities using the 26 selected International GNSS Service (IGS) stations having stable long-term data and distributed along the relevant tectonic plates (Table 1). All the site velocities are derived in a Eurasia-fixed reference frame.

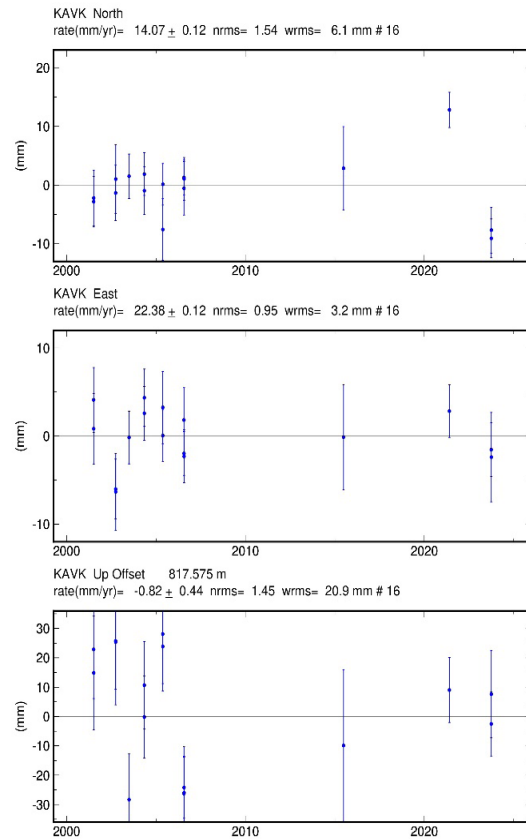


Figure 7 The plot of long-term (annual) position repeatability for the KAVK station (the north, east and up components are in order from top to bottom, respectively).

RESULTS AND DISCUSSION

The general pattern of the tectonic mechanism in the mid-section of the NAFZ, which is derived using GNSS sites with varying velocities in N-S direction, validates the rotational westward migration of the Anatolian plate. The site velocities on the Eurasian plate are estimated in a range of 2-3 mm/year, where the northern block bounding the main branch of the NAFZ is relatively stable. On the other hand, some of the sites having anomalous velocities does not reflect the characteristic features of the velocity field and discriminate from the regional trend (AKPI, SUN1, SNGR). It is argued that the discrimination of the site velocities is possibly caused by the local deformations and relatively short observation spans. The velocity solution confirms the estimation of the site velocities ranging 3-30 mm/year with their associated uncertainties of maximum ±1.5 mm/year (Figure 8). Considering the relatively stable Eurasia plate, some of the sites located at the north of the main branch of the NAFZ (KRG1, GKCD, KAML, GOL5) have inconsistent velocities in a

range of 5-10 mm/year unlikely their local characteristics.

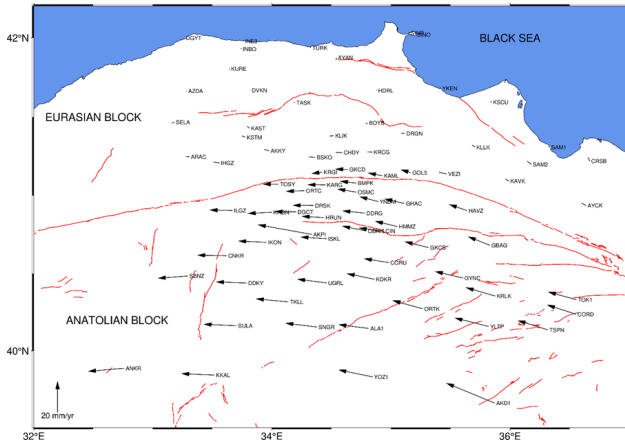


Figure 8 The velocity field referenced to ITRF2014 datum and derived with respect to the Eurasia-fixed reference plate in this study.

In order to provide the latest velocity field for the mid-section of the NAFZ, a GNSS network consisting of 60 sites was established, which also contains 15 permanent stations from TUSAGA-Active network. There are a number of 10 sites, in which the site velocities have been estimated for the first time. The uncertainty of our velocity estimation for the same sites used also in Yavařođlu et al. (2011) is less than 0.5 mm/year. On the other hand, the velocity field solution derived has some statistically poor estimation with 1 mm/year uncertainty for the sites namely KVAK, YLTP, INE3, SAM2 and OBRK compared to the others. This might be caused from the short time span between the first and last observations of these sites.

The velocity field derived in this study confirms the anti-clockwise rotation of the Anatolian plate reported in the previous studies (Hubert-Ferrari et al., 2002; Hartleb et al., 2003; Kozacı et al., 2007; Yavařođlu et al., 2011; Aladođan et al., 2017, 2020; Aktuđ et al., 2015; Yavařođlu et al., 2020; Kurt et al., 2022).

The most important result of this study is that some sites at the north of the main branch of the NAFZ, specifically the sites around the Çorum-Kargı province, have larger velocities than 5 mm/year not alike the local trend. Accordingly, this study suggests that the deformation zone along the NAFZ in this region is wider than 10-15 km.

Although there are evident preliminary results based on the latest velocity field solution in this study, the regional strain accumulations and seismic potential of the fault segments at the mid-section of the NAFZ are planned to investigate further in details.

CONCLUSION

This study focused on the mid-section of the NAFZ, where a comprehensive GNSS network comprising of 60 sites with the permanent stations from TUSAGA-Active network and survey sites to be observed periodically, was established to precisely constrain the fault slip rates and plate motions. The initial results clearly confirm the westward migration of the

Anatolian plate, on which site velocities range of 3-30 mm/year and are in consistent with the previously published studies (Hubert-Ferrari et al., 2002; Yavařođlu et al., 2020).

The one of the most important conclusions of this study is that the sites at the north of the main branch of the NAFZ, particularly the ones close to Çorum-Kargı province, have velocities larger than 5 mm/year indicating a significant deformation in this region. This suggests that the deformation zone of the NAFZ in this area may extend beyond 10-15 km.

While these preliminary results regarding the velocity field provide notable insights, ongoing geodetic studies are quite crucial to better understand the present-day deformations and seismic potential of the region. It is expected that the continuous monitoring and analyses will help us to refine our understanding of seismic hazards and to contribute more on effective earthquake risk mitigation strategies.

Acknowledgement

This study was supported by TÜBİTAK (project number 123Y293) and Hitit University Scientific Research Unit (project number ODMYO19001.23.001). We would like to thank the General Directorate of Land Registry and Cadastre (TKGM) and the General Directorate of Mapping for the TUSAGA-ACTIVE data used in the study. Figure 4 and 8 are produced by the Generic Mapping Tools software (Wessel et al. 2019).

References

1. AFAD, 06 Şubat 2023 Pazarcık (Kahramanmaraş) Mw 7.7 ve Elbistan (Kahramanmaraş) Mw 7.6 Depremlerine İlişkin Ön Deđerlendirme Raporu. The Disaster and Emergency Management Presidency, March, İstanbul. 2023
2. Aktuđ B, Dođru A, Özener H, Peyret M. Slip rates and locking depth variation along central and easternmost segments of North Anatolian Fault. *Geophys J Int.* 2015; 202(3), 2133-2149.
3. Akyar BE. Deprem tekrar lama periyotlarının jeodezik verilerle belirlenmesi: Banaz ve Elvanpařa segmenti, Yüksek Lisans Tezi, Afyon Kocatepe Üniversitesi, Fen Bilimleri Enstitüsü, Afyonkarahisar, 86; 2020.
4. Aladođan K, Tiryakiođlu İ, Yavařođlu H, Alkan RM. Kuzey Anadolu Fayı Bolu-Çorum Segmenti Boyunca Yer Kabuđu Hareketlerinin GNSS Yöntemiyle İzlenmesi. *Afyon Kocatepe Üniversitesi Fen Ve Mühendislik Bilimleri Dergisi.* 2017; 17(3), 998-1003.
5. Ambraseys, NN and Finkel, CF. The Seismicity of Turkey and Adjacent Areas-a Historical Review, 1500-1800. Eren, İstanbul, 240; 1995.
6. Barka AA, Kadinsky CK. Strike-slip fault geometry in Turkey and its influence on earthquake activity. 1988; *Tectonics*, 7: 663-684.
7. Barka AA. Slip distribution along the North Anatolian Fault associated with large earthquakes of period 1939 to 1967. *Bulletin of the Seismological Society of America.* 1996; 86, 5, 1238-1254
8. Barka AA. The north anatolian fault zone. *Annales Tectonicae.* 1992; 164-195.
9. Bohnhoff M, Martínez-Garzón P, Bulut F, Stierle E, Ben-Zion Y. Maximum earthquake magnitudes along different sections of the North Anatolian fault zone. *Tectonophysics.* 2016; 674, 147-165.
10. Emre Ö, Duman TY, Özalp S, Şarođlu F, Olgun S, Elmacı H, Çan T. Active fault database of Turkey. *Bull Earthquake Eng.* 2018; 16,

- 3229–3275.
11. Emre Ö, Elmacı H, Özalp S. Correction to: Merzifon–Esençay splay fault within the North Anatolian Fault system: segmentation and timing of the last two surface faulting events on Esençay segment. *Med. Geosc. Rev.* 2020; 2, 383.
 12. Emre Ö, Kondo H, Özalp S, Elmacı H. “Fault geometry, segmentation and slip distribution associated with the 1939 Erzincan earthquake rupture along the North Anatolian fault, Turkey”, *Characterization of Modern and Historical Seismic-Tsunamic Events, and Their Global-Societal Impacts*, Y. Dilek, Y. Ogawa, Y. Okubo, 2021.
 13. Erturac MK, Tuysuz O. Amasya ve çevresinin depremselliği ve deterministik deprem tehlike analizi. *itüdergisi/d mühendislik.* 2010; 9. 121-132.
 14. Erturac MK, Tüysüz O. Kinematics and basin formation along the Ezinepazar–Sungurlu fault zone, NE Anatolia, *Turkish Journal of Earth Sciences.* 2012; 497 - 520.
 15. Eyübağil EE, Solak H, Kavak US, Tiryakioğlu İ, Sözbilir H, Aktuğ B, Özkaymak Ç. PresentDay Strike-Slip Deformation Within The Southern Part Of Izmir Balıkesir Transfer Zone Based On GNSS Data And Implications For Seismic Hazard Assessment, Western Anatolia. *Turkish Journal of Earth Sciences.* 2021; 30, 143-160.
 16. Gezgin C, Ekerin S, Tiryakioğlu I, Aktuğ B, Erdoğan H, Gürbüz E, Osman O, Bilgilioglu SS, Torun AT, Gündüz Hİ. Oktar O, Türkmen C, Kaya E. Determination of recent tectonic deformations along the Tuz Gölü Fault Zone in Central Anatolia (Turkey) with GNSS observations. *Turkish Journal of Earth Sciences.* 2022; 31(1), 20-33.
 17. Ghilani, CD., and Wolf, PR., *Elementary Surveying: An Introduction to Geomatics.* Pearson, 2012.
 18. Hartleb RD, Dolan JF, Akyüz HS, Yerli B. A 2000 year-long paleoseismologic record of earthquakes along the central North Anatolian Fault, from trenches at Alayurt, Turkey. *Seismological Society of America Bulletin.* 2003; 93, 1935-1954.
 19. Herring TA. *Geodetic Applications of GPS*, *Proceedings of the IEEE*, 87, 1, 92-110, 1999.
 20. Herring TA, King RW, Floyd MA, McClusky SC. *Introduction to GAMIT/GLOBK*, Release 10.7, Department of Earth, Atmospheric and Planetary Sciences, Mass. Inst. of Technol; 2018.
 21. Hubert-Ferrari A, Armijo R, King G, Meyer B, Barka AA. Morphology, displacement, and slip rates along the North Anatolian Fault, Turkey. *Journal of Geophysical Research.* 2002; 107 (B10), 9/1-9/33.
 22. İRAP İl Afet Risk Azaltma Planı, Amasya Valiliği İl Afet ve Acil Durum Müdürlüğü; (2021). <https://amasya.afad.gov.tr/kurumlar/amasya.afad/planlar/AMASYAIRAP.pdf>
 23. İRAP İl Afet Risk Azaltma Planı, Çorum Valiliği İl Afet ve Acil Durum Müdürlüğü, (2021). https://corum.afad.gov.tr/kurumlar/corum.afad/Haberler/2022/nisan/Corum_1%CC%87RAP_SON.pdf
 24. Jackson J. and McKenzie D., Active tectonics of the Alpine–Himalayan Belt between western Turkey and Pakistan, *Geophysical Journal International*, Volume 77, Issue 1, April 1984, Pages 185–264, <https://doi.org/10.1111/j.1365-246X.1984.tb01931.x>
 25. Kaiser AE, Green AG, Campbell FM, Horstmeyer H, Manukyan E, Langridge RM, McClymont AF, Mancktelow N, Finnemore M, Nobes DC. Ultrahigh-resolution seismic reflection imaging of the Alpine Fault, New Zealand. *Journal of Geophysical Research*, 2009.
 26. Ketin İ. Kuzey anadolu fayı Hakkında. *Maden Tetkik ve Arama Dergisi.* 1969; 72, 1-27.
 27. KOERI, 06 Şubat 2023 Gaziantep-Kahramanmaraş ve 20 Şubat 2023 Hatay Depremleri Ön Değerlendirme Raporu, Kandilli Observatory and Earthquake Research Institute, İstanbul, 2023
 28. Kozacı O, Dolan JF, Finkel R, Hartleb R. Late Holocene slip rate for the North Anatolian Fault, Turkey, from cosmogenic ³⁶Cl geochronology: Implications for the constancy of fault loading and strain release rates. *Geology.* 2007; 35, 867– 870.
 29. Köksal E. *Yüzey Deformasyonlarının Diferansiyel İnsar Tekniği İle Belirlenmesi: İsmetpaşa Örneği.* Doktora Tezi, ZKÜ, Fen Bilimleri Ens. Zonguldak; 2011.
 30. Kurt A, Özbakır A, Cingöz A, Ergintav S, Dogan U, Özarpacı S. Contemporary velocity field for Turkey inferred from combination of a dense network of long term GNSS observations. *Turkish Journal Of Earth Sciences.* 2022; 31. 10.55730/yer-2203-13.
 31. Lay T, Wallace LM. *Modern global seismology.* Elsevier. 1995
 32. Massonnet D, Feigl KL. Radar interferometry and its application to changes in the Earth's surface. *Rev. Geophys.*, 36(4), 441-500, 1998
 33. McCalpin JP, Nelson AR. *Introduction to Paleoseismology.* In: McCalpin, J.P. (Ed.), *Paleoseismology.* Academic Press, London, 1996, pp. 1–32.
 34. McClusky S, Balassanian S, Barka A, Demir C, Georgiev I, Hamburger M, Hurst K, Kahle H, Kastens K, Kekelidze G, King R, Kotzev V, Lenk O, Mahmoud S, Mishin A, Nadariya M, Ouzounis A, Paradisis D, Peter Y, Prilepi M, Reilinger R, Sanli I, Seeger H, Tealeb A, Toksoz M N, Veis G. GPS Constraints on Crustal Movements and Deformations in the Eastern Mediterranean (1988-1997): Implications for Plate Dynamics. *JGR.* 2000; 105(B3), 5695-5719
 35. Michetti AM, Audemard FA, Marco S. (2005). Future trends in paleoseismology: integrated study of the seismic landscape as a vital tool in seismic hazard analyses. *Tectonophysics*, 408, 3-21.
 36. Okay AI, Demirbağ E, Kurt H, Okay N, Kuşçu I. An active, deep marine strikeslip basin along the North Anatolian Fault in Turkey. *Tectonics.* 1999; 18, 129-148.
 37. Özalaybey S, Zor E, Ergintav S, Tapırdamaz MC. Investigation of 3-D basin structures in the Izmit Bay area (Turkey) by single-station microtremor and gravimetric methods. *Geophysical Journal International*, 2011, 186(2): 883-894
 38. Özkan A. Kuzeydoğu Akdeniz Bölgesindeki Diri Fayların Kinematığının GPS Gözlemleri ve Elastik Yarı Uzaysal Yer Değiştirme Modeli ile Belirlenmesi, Doktora Tezi, İstanbul Teknik Üniversitesi, Lisansüstü Eğitim Enstitüsü, İstanbul, 2021.
 39. Özkan A, Yavaşoğlu HH, Masson F. Present-day strain accumulations and fault kinematics at the Hatay Triple Junction using new geodetic constraints. *Tectonophysics*, 2023, 854, 229819.
 40. Poyraz F, Hastaoglu KO, Kocbulut F, Tiryakioğlu I, Tatar O, Demirel M, Duman H, Aydın C, Ciger AF, Gürsoy Ö, Türk T, Sıgırcı R. Determination of the block movements in the eastern section of the Gediz Graben (Turkey) from GNSS measurements. *Journal of Geodynamics, Special issue: Tethyan Evolution, Anatolia.* 2018; 123(2), 117-135.
 41. Reilinger R, McClusky S, Vernant P, Lawrance S, Ergintav S, Cakmak R, Ozener H, Kadirov F, Guliev I, Stepanyan R, Nadariya M, Hahubia G, Mahmoud S, Sakr K, ArRajehi A, Par adissis D, AlAydrus A, Prilepin M, Guseva T, Evr en E, Dmitrotsa A, Filikov S, V, Gomez F, AlGhazzi R, Karam G. GPS Constraints on Continental Deformation in the Africa Arabia Eurasia Continental Collision Zone and Implications for the Dynamics of Plate Interactions. *J*

- Geophys. Res. 2006; 111, B05411
42. Schowengerdt RA., Remote Sensing: Models and Methods for Image Processing. Academic Press. 2007.
 43. Solak Hİ. İzmir-Balıkesir Transfer Zonu ve Çevresindeki Güncel Deformasyonların GNSS Yöntemi ile İncelenmesi, Doktora Tezi, A.K.Ü., Fen Bilimleri Enstitüsü, Afyonkarahisar; 2020.
 44. Solak Hİ, Tiryakiođlu İ., Özkaymak Ç., Sözbilir H., Aktuđ B., Yavařođlu HH., and Özkan A., Recent tectonic features of Western Anatolia based on halfspace modeling of GNSS Data. Tectonophysics, 2024, 230194, <https://doi.org/10.1016/j.tecto.2023.23.0194>
 45. Stein S and Wysession M. An Introduction to Seismology, Earthquakes, and Earth Structure. Wiley-Blackwell. 2003.
 46. řarođlu F, Emre Ö, Boray A. Türkiye'nin Diri Fayları ve Depremsellikleri, Maden Tetkik ve Arama Genel Müdürlüğü. 1987; Rapor No:8174, 394 s.
 47. řengör AMC, Tüysüz O, İmren C, Sakınç M, Eyidođan H, Görür N, Le Pichon X, Claude Rangin C. The North Anatolian Fault: A new look. Ann. Rev. Earth Planet. Sci. 2005; 33: 37-112.
 48. Takcı V. 1943 Tosya-Ladık Deprem Kırığı'nın Ladık Kuzeyindeki Bölümünün Paleosismik İncelenmesi, Yüksek Lisans Tezi, Cumhuriyet Üniversitesi, Fen Bilimleri Enstitüsü, Sivas, 2015.
 49. Tiryakiođlu İ. GNSS Ölçüleri ile Güneybatı Anadolu'daki Blok Hareketleri ve Gerilim Alanlarının Belirlenmesi, Yıldız Teknik Üniversitesi, Fen Bilimleri Enstitüsü, Doktora Tezi, 155s, İstanbul, 2012.
 50. Tiryakiođlu İ, Aktuđ B, Yiđit C Ö, Yavařođlu H. H, Sözbilir H, Özkaymak Ç, Poyraz F, Taneli E, Bulut F, Dođru A, Özener H. Slip distribution and source parameters of the 20 July (2017) Bodrum-Kos earthquake (Mw6.6) from GPS observations, Geodinamica Acta. 2018; 30:1, 1-14.
 51. Wells DL, Coppersmith KJ. New empirical relationships among magnitude, rupture length, rupture width, rupture area, and surface displacement. Bulletin of the seismological Society of America. 1994; 84(4), 974-1002.
 52. Yavařođlu H. Kuzey Anadolu Fayının Orta Anadolu Bölümündeki Güncel Tektonik Aktivitenin Jeodezik Yöntemler Ve Elastik Yarı Uzay Modelleme ile Belirlenmesi, Doktora Tezi, İstanbul Teknik Üniversitesi, Fen Bilimleri Enstitüsü, İstanbul, 2009.
 53. Yavasoglu H, Tari E, Tuysuz O, Cakir Z, Ergintav S. Determining and modelling tectonic movements along the central part of the North Anatolian Fault (Turkey) using geodetic measurements. Journal of Geophysical Research. 2011; 51(5): 339-343.
 54. Yavařođlu HH, Alkan MN, Bilgi S, Alkan Ö. Monitoring aseismic creep trends in the İsmetpařa and Destek segments throughout the North Anatolian Fault (NAF) with a large-scale GPS network, Geosci. Instrum. Method. Data Syst. 2020; 9, 25-40, <https://doi.org/10.5194/gi-9-25-2020>.
 55. Yıldız SS, Özkan A, Yavařođlu HH, Masson F, Tiryakiođlu İ, Alkan MN, Bilgi S. Determination of recent tectonic deformations in the vicinity of Adana-Osmaniye-Hatay-Gaziantep triple junction region by half-space modeling. Comptes Rendus. Géoscience, 2021, 352, 225-234.

HITTITE JOURNAL OF SCIENCE AND ENGINEERING

e-ISSN: 2148-4171
Volume: 11 • Number: 3
September 2024

Comparison of Geological Structures and Satellite-based Tectonic Lineaments in Gülağaç (Aksaray) and its Surroundings

Ramazan Demircioğlu 

Aksaray University, Department of Emergency Aid and Disaster Management, 68100, Aksaray, Türkiye.

Corresponding Author

Ramazan Demircioğlu

E-mail: ra.demircioglu@gmail.com Phone: +90 542 597 9432

RORID: <https://ror.org/026db3d50>

Article Information

Article Type: Research Article

Doi: <https://doi.org/10.17350/HJSE19030000339>

Received: 25.05.2024

Accepted: 27.07.2024

Published: 30.09.2024

Cite As

Demircioğlu, R. Comparison of Geological Structures and Satellite-based Tectonic Lineaments in Gülağaç (Aksaray) and its Surroundings. Hittite J Sci Eng. 2024;11(3):123-129.

Peer Review: Evaluated by independent reviewers working in at least two different institutions appointed by the field editor.

Ethical Statement: Not available.

Plagiarism Checks: Yes - iThenticate

Conflict of Interest: The author declares no conflict of interest

CRedit AUTHOR STATEMENT

Razaman Demircioğlu: Conceptualization, Methodology, Software, Validation, Writing- original draft. Writing- review and editing.

Copyright & License: Authors publishing with the journal retain the copyright of their work licensed under CC BY-NC 4.

Comparison of Geological Structures and Satellite-based Tectonic Lineaments in Gülağaç (Aksaray) and its Surroundings

Ramazan Demircioğlu

Aksaray University, Department of Emergency Aid and Disaster Management, 68100, Aksaray, Türkiye

Abstract

The study area covers the Gülağaç district of Aksaray and its surroundings in the Central Anatolia region of Turkey. The basement of the study area consists of metamorphic rocks belonging to the Paleozoic–Mesozoic-aged Kaman Group. Mesozoic-aged ophiolites overlie these rocks, and both are cut by Late Cretaceous-aged igneous rocks. These units were then overlain by Palaeocene-Quaternary-aged volcanic and sedimentary units. The region has important geological structures that have undergone polyphase deformation, especially in the Eocene units. As a result of these deformations, faults, fractures, folds and linearities were formed. These structures were compared with satellite-based tectonic lineaments, and it was observed that the general orientations of the lines determined in the field and the satellite-based lineaments were largely compatible. The results of this study can make an important contribution to the exploration of mineral and geothermal resources in the region.

Keywords: Türkiye, Central Anatolia, Aksaray, Gülağaç, tectonic lineaments.

INTRODUCTION

The research focuses on Gülağaç and its surrounding regions located in the Aksaray province of the Central Anatolia region in Türkiye (Figure 1).

The study area is located within the Cappadocia Volcanic Province, where young volcanism is particularly intense. The region is particularly rich in geothermal resources. Currently, geothermal resource exploration continues in different parts of the region. This study will be a data source for the determination of geothermal areas. There are many studies on geothermal areas and tectonic lineaments in different parts of the world.

Previous investigations conducted in and around the study area have included sedimentological, petrographic, and structural geological studies.

Some of the sedimentological studies were carried out by [2-13]. Some of the petrographic studies in the study area were carried out by [14-21].

[22-27] conducted studies on the tectonic-neotectonic features of the study area. Similarly, [28-31] conducted studies on the Tuzgölü fault zone within this tectonic area.

The study area is of great importance in terms of natural disasters, especially earthquakes, due to its proximity to the Tuzgölü fault zone. In addition, the geological structure of the rocks in the region increases the possibility of landslides and poses a potential danger. Geophysical and geological studies are very important in engineering studies in order to deepen the emergence of geological structures [32-35].

In recent years, lineament studies obtained by remote sensing have been frequently used in different fields of geology. Some of the studies on mineral deposits and their relationship with linearity are [36-39]. Linearity studies are available for the determination of geothermal areas. Some of them are [40-41]. There are also studies on the relationship between tectonics and linearity. Some of them are [42-45].

This study aims to compare the structures showing tectonic lineaments (fault, fracture, fold axis) observed in the Eocene-aged units in Demirci and its vicinity with the satellite-based lineaments.

MATERIAL AND METHODS

A geological map of the study area was completed during the fieldwork. The planes of the faults and fractures, which exhibited linearity, were measured and assessed.

The study area underwent a thorough evaluation by analysing the prior research and comparing it with the findings of this study. A meticulous review and assessment of both field observations and computer analyses were conducted to arrive at a comprehensive conclusion. For the computer analysis, a flowchart was created (Figure 2). The image is first analysed in Envi, Geomatica, and ArcGIS before being turned into a lineament map (Figure 5b). The generated maps do not contain any artificially constructed structures—only naturally occurring lines. During the field studies, structures such as

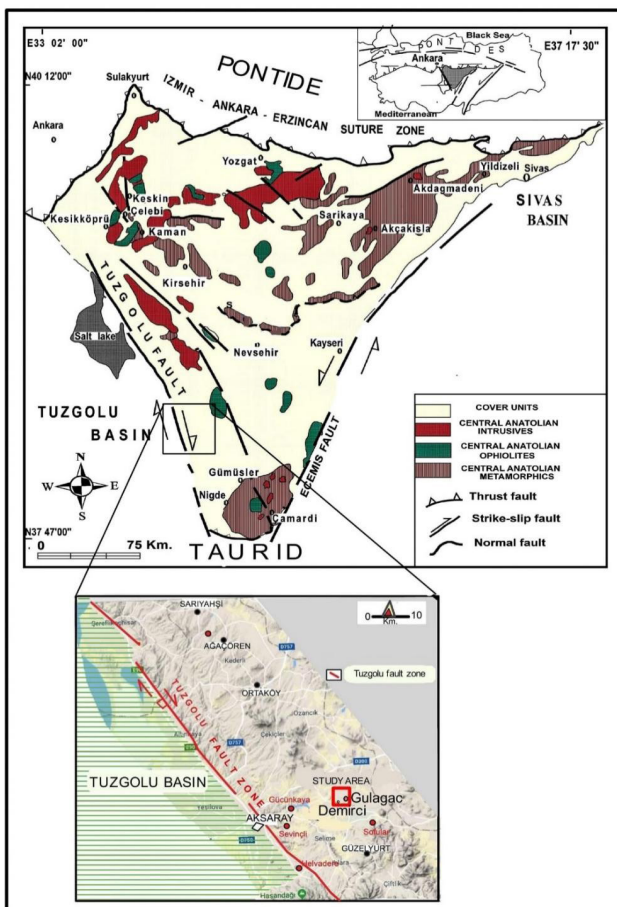


Figure 1 Central Anatolian Crystalline complex and study area (Modified from, [1]).

field boundaries, roads, etc. that create lineaments in satellite images were identified, and these lineaments were excluded.

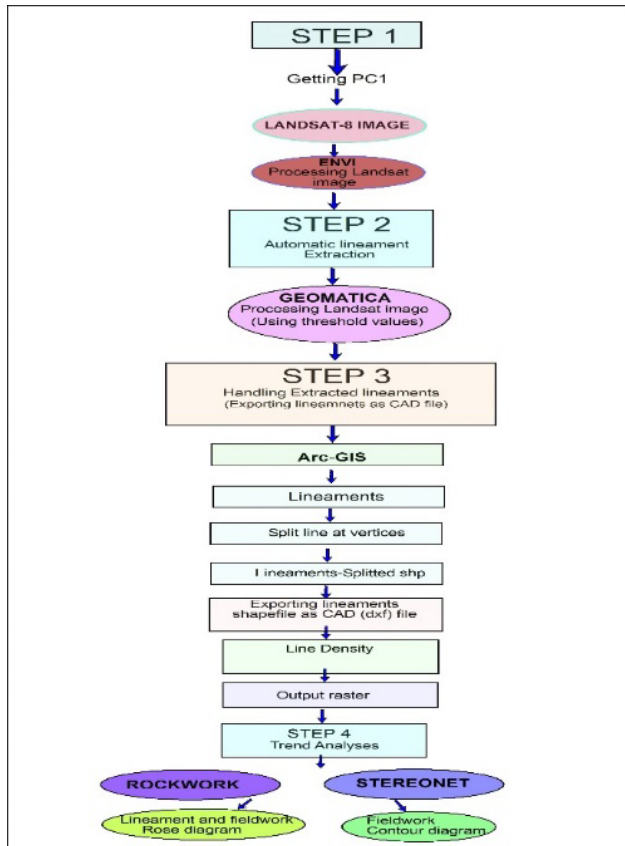


Figure 2 Flowchart of lineament maps and diagram preparation.

A thorough assessment was carried out by combining on-site observations with computerised analysis of satellite imagery. Figure 2 illustrates the lineaments obtained through computer programs. These results facilitated a comparison between the geological structures such as faults, fractures, and fold hinge lines in the Gülağaç area and the lineaments extracted from the satellite images.

GEOLOGY Stratigraphy

This study is focused on the Gülağaç district and Gülağaç town in the Aksaray province, along with its surrounding areas. The Tamadağ and Bozçaldağ metamorphics, which belong to the Kaman Group of the Kırşehir Massif, are crucial in the basement rocks of the study area. The Tamadağ metamorphites are mainly composed of gneisses and quartzites (Figure 3).

Bozçaldağ metamorphites are composed of marbles and amphibolites in interbeds with them. Central Anatolian ophiolites are thrust on these units. These units were cut by Late Cretaceous aged Central Anatolian igneous rocks such as granite, granodiorite and syenite (Figure 4). [46].

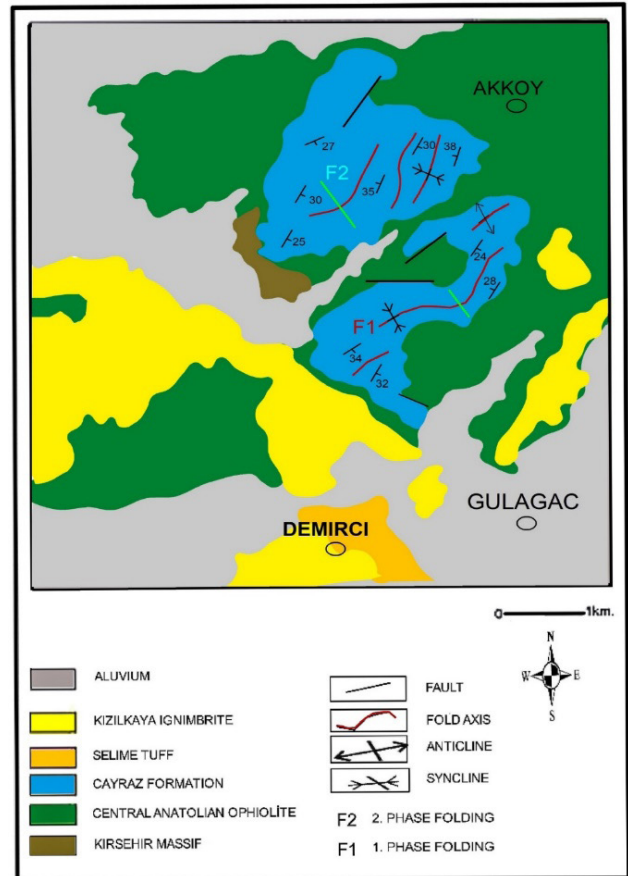


Figure 3 Geological map of the study area and its surroundings.

The Kızıltepe Formation, which consists of loosely consolidated, purple-coloured conglomerate, sandstone, claystone, and mudstone, is a Late Cretaceous-Paleocene-aged terrestrial formation.

Overlying these units is the Cayraz Formation, which consists of marine sandstone, marl, and limestone and is of the Lower Eocene age. These units are unconformably overlain by the Oligo-Miocene-aged Mezgit Formation, consisting of shales, sandstones, mudstones, and evaporites.

The Gostuk Ignimbrite, Uzunkaya Formation, Melendiz Volcanite, Selime Tuff, Kızilkaya Ignimbrite, and Gosterli Volcanite are all units composed mainly of Pliocene-Pleistocene volcanic material. These units are unconformably overlain by recent slope debris, travertine, and alluvium (Figure 4).

ERA	PERIOD	FORMATION	THICKNESS(m)	LITOLGY	EXPLANATIONS	
CENOZOIC	QUATERNARY	ALLUVION	5	Gravel, sand, clay.		
		TRAVERTINE	30	Yellow, beige coloured travertine.	Disconformity	
	PLEISTOCENE	GOSTERLI VOLCANICS	100	Black-coloured lava fragments, ash.		
		KIZILKAYA IGNIMBRITE	400	Yellow, red coloured ignimbrite.		
	PLIOCENE	SELIME TUFF	100	Yellow, white coloured tuff.		
		MELENDIZ VOLCANICS	200	Dark coloured basalt, andesite, pyroclastics.		
		UZUNKAYA	150-200	Volcanic fragmented, laterally-vertically transgressive tuff, conglomerate, sandstone, siltstone.	Disconformity	
		GOSTUK IGNIMBRITE	60	Grey, brown coloured ignimbrite.		
		MEZGIT		Yellow, brown coloured, conglomerate, sandstone siltstone, claystone.	Disconformity	
	EOCENE	CAYRAZ		Sandstone, limestone, marn.	Disconformity	
	PALAEOCENE	KIZILTEPE		Red, burgundy coloured conglomerate, sandstone.	Disconformity	
	PALAEZOIC MESOZOIC	Kaman Group	CENTRAL ANATOLIAN MAGMATICS		CENTRAL ANATOLIA OPHIOLITE	TECTONIC CONTACT
			BOZCALDAG		Marble, amphibolite.	
			TAMADAG	100-200	Gneiss, quartzite, amphibolite.	

Figure 4 Stratigraphic columnar section of the study area and its surroundings (modified from [47]).

Structural Geology

In the area we studied, the metamorphic rocks of the Kaman Group, which are of the Palaeozoic-Mesozoic age, went through polyphase deformation and created folded and fractured structures. Additionally, the Lower Eocene-aged units of the Cayraz formation in the same area underwent at least two stages of folding. These changes are believed to be connected to the closure of the Inner Taurus Ocean. In the study area, the Palaeozoic-Mesozoic-aged metamorphic rocks belonging to the Kaman Group underwent polyphase deformation and formed folded-fractured structures. In the study area, the Eocene-aged units belonging to the Cayraz formation also underwent at least two stages of folding. These deformations are thought to be related to the closure of the Inner Taurus Ocean.

RESULTS AND DISCUSSION

Lineament Maps

Satellite imagery and software tools such as Envi, Geomatica, and ArcGIS were utilized to create automatic lineament maps in the Gülağaç area [48-52].

These maps were generated by using Landsat-8 images obtained from a website (earthexplorer.usgs.gov) (Figure 5a). Landsat-8 pictures of Gülağaç and its surroundings were obtained and an automatic lineament map was produced

using suitable filters and threshold values as described in [53] (Figure 5b).

To create a lineament map, the image is first processed in Envi, Geomatica, and ArcGIS (Figure 5b). The resulting maps include only natural lines and exclude artificially created structures.

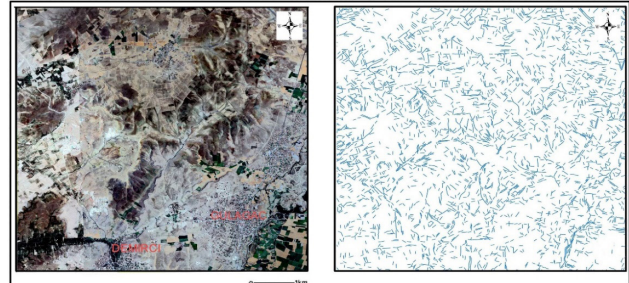


Figure 5 a- Satellite image of the Gülağaç and its surroundings b- Lineament map of the study area.

The lineament map was determined by superimposing the satellite image and the obtained lineament images (Figure 6).

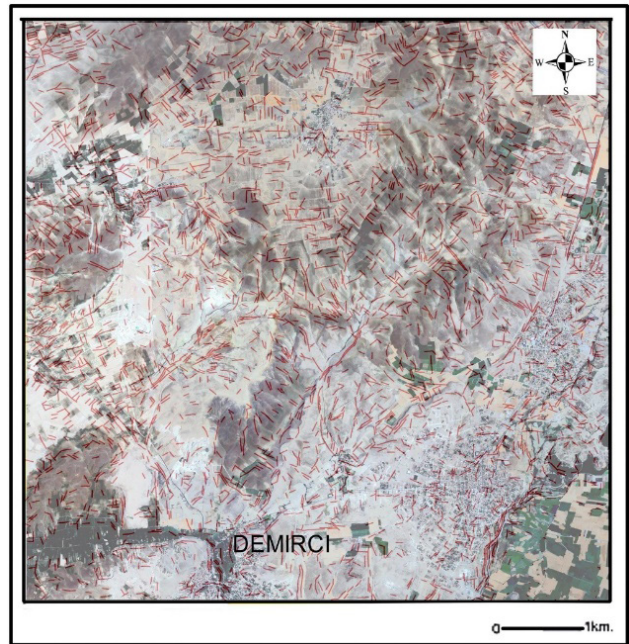


Figure 6 Landsat-8 image and lineaments of the area.

The generated lineament map was converted into a density map (Figure 7a). A density map and automatic lineaments map were also made (Figure 7b).

Tectonic lineaments are represented in the terrain by fault, fracture, and fold hinge line trends (Figure 7). In the terrain, morphological structures are sometimes in the form of lines formed by erosion surfaces. Although such lines are seen as tectonic lineaments, they are not related to tectonism but to erosion. Such morphological lines are kept separate from tectonic lineaments.

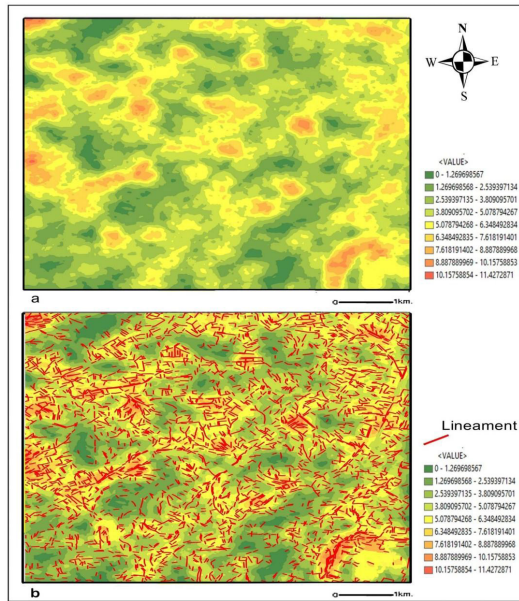


Figure 7 (a) Density map of study area (b) lineament and lineament density map.

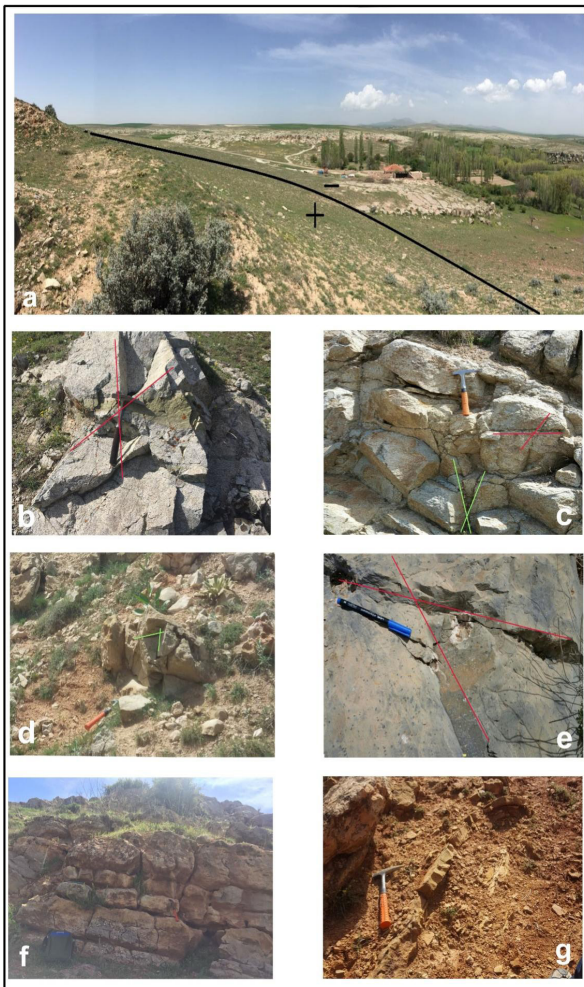


Figure 8 (a) Normal fault in the study area (b-c) Fractures in the ophiolites (d-e) Fractures in the Cayraz formation (f, g) Inclined, folded strata in the Cayraz formation.

Evaluation of Satellite and Fieldwork Lineaments

Rose diagrams were created to analyse the distribution of lineations in the study area based on automatic lineaments. In the study area, fault, fracture, and fold axis measurements, which constitute the lineaments, were evaluated in the Stereonet software (Fig. 9).

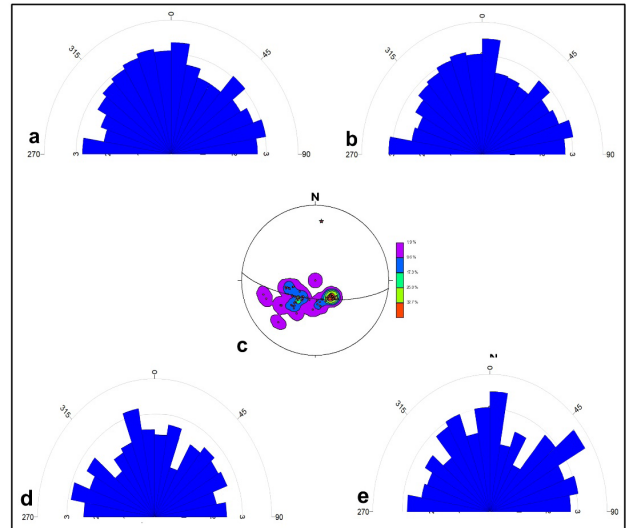


Figure 9 a- Rose diagram of %L: Length as a percentage of the total linear length. b- Rose diagram of %N: Length as a percentage of total lineation population. c- Point-contour diagram of Cayraz formation (65 bedding measurements) d- Contour diagram of 1st phase shear fracture in ophiolites (41 fracture measurements) e- Contour diagram of 2nd phase shear fracture in ophiolites (44 fracture measurements).

Results showed that lineaments were present in all orientations, with the most intense orientations being, N0-10°E, N40-50°E, N70-80°E, and N80-90°W, N20-30°W, and N30-40°W (Figure 9a,b). Additionally, fracture systems were studied and mapped, with diagrams prepared specifically for sedimentary rocks (Figures 9c, d, and e). The results were generally compatible when comparing strike-rose and automatic lineament diagrams based on field measurements. Based on measurements of the layers of the Cayraz Formation (65 bedding measurements), the general fold hinge line orientation was determined to be N8°E/14°NE (Figure 9c). This orientation aligns well with the dominant orientation found in the rose diagrams of satellite-based lineaments. Additionally, phase 1 shear fracture (41 measurements) in ophiolites showed shear fracture planes of N10-20°W and N70-80°W, while phase 2 shear fracture (44 measurements) in ophiolites revealed shear fracture planes of N0-10°W and N50-60°E (Figure 9d,e).

CONCLUSIONS

The region being studied has undergone significant structural changes due to the effects of the tectonic regime that emerged, particularly between the Middle-Late Eocene-Upper Miocene period, which was characterized by compressive forces. These deformations have resulted in the formation of various types of faults and fractures with different orientations. By using automatic lineament analysis to examine the lineations in the study area, rose diagrams were produced that indicated the presence of lineations in all directions. The most intense

orientations were N0-10°E, N40-50°E, N70-80°E, N80-90°W, N20-30°W, and N30-40°W. When the Cayraz Formation beds were measured, the general orientation of the fold hinge line was found to be N8°E/14°NE. The ophiolites have undergone phase 1 and phase 2 shear fractures, with N10-20°W, N70-80°W, N0-10°W, and N50-60°E being the identified shear fracture planes. This observation is consistent with the lineaments detected by satellite imagery.

The study compared data collected from field studies with that obtained from satellite-based studies. The findings reveal that the data from both sources are compatible. This study has generated valuable data that can be helpful for future exploration of minerals and geothermal resources. Geophysical and geological parameters can additionally support this study to obtain more realistic supporting results. The study area, situated within the Cappadocia Volcanic Province, possesses significant geothermal energy potential. The identified lineations in this study and their concentrated areas may indicate potential geothermal sites

Acknowledgement

The author would like to thank the editors and reviewers of the journal for their efforts and interest.

References

- Kuşcu I. Geochemistry and mineralogy of the skarns in the Celebi district, Kırıkkale, Turkey. *Turkish Journal of Earth Sciences*. 2001;10:121-132.
- Rigo de Righi M, Cortesini A. Regional studies of the Central Anatolian basins progress report. PDR Turkish Gulf Oil Co. Report No. II; 1960.
- Beekman PH. The Pliocene and Quaternary volcanism in the Hasan Dağ-Melendiz Dağ region, MTA Bulletin. 1966;2:90-105.
- Arıkan Y. Tuz Gölü havzasının jeolojisi ve petrol imkanları, M.T.A. Dergisi. 1975;3: 17-37.
- Görür N, Derman AS. Tuzgölü-Haymana havzasının stratigrafik ve tektonik analizi, TPAO Rapor no: 1514;1978.
- Uygun A. Tuzgölü havzasının jeolojisi, evaporit oluşumları ve hidrokarbon olanakları, TJK İç Anadolu'nun Jeolojisi Sempozyumu. 1981; 66-71.
- Görür N, Oktay FY, Seymen İ, Şengör AMC. Paleotectonic evolution of the Tuzgölü basin complex, Central Turkey. Sedimentary record of a Neo-Tethyan closure, The Geological Evolution of the Eastern Mediterranean. *Geology Society Special Publication*, 17, In J.E. Dixon, and A.H.F. Robertson (eds.). Oxford. 1984;17: 467-482.
- Atabey E, Tarhan N, Akarsu B, Taşkıran A. Şereflikoçhisar, Panlı (Ankara) Acıpınar (Niğde) Yöresinin Jeolojisi, Maden Tetkik ve Arama Genel Müdürlüğü Raporu no: 8155;1987.
- Dellaloğlu A. Ankara ili-Tuz Gölü arasındaki Neotetis'in kuzey kolunun evrimi (Haymana-Tuzgölü Basenlerinin stratigrafileri ve jeoteknik evrimleri, Ph.D. Thesis, Çukurova University, Adana;1997.
- Çemen İ, Göncüoğlu MC, Dirik K. Structural evolution of the Tuzgölü basin in Central Anatolia.Turkey, *Journal of Geology*. 1999. p. 693-706.
- Dirik K, Erol O. Tuzgölü ve çevresinin tektonomorfolojik evrimi, Orta Anadolu-Türkiye. TPJD Özel sayı. 2003.p. 27-46.
- Uçar L. Hanobası-Karapınar (KB Aksaray) alanının stratigrafik incelenmesi. *Geosound* 2008;52:185-212.
- Lahn NE. Türkiye Deprem Haritası Hakkında Muhtıra. M.T.A.Dergisi. 1944. p. 364-371.
- Pasquare G. Geology of the Cenozoic Volcanic area of Central Anatolia, Atti Della Accad. Nazio. Dei. Lincei, Memorie, ser. 1968.p. 55- 204.
- Innocenti F, Mazzuoli R, Pasquare G, Radicati F, Villari L. Neogene calc-alkaline volcanism of Central Anatolia: geochronological data on Kayseri-Niğde area, *Geological Magazine*. 1975. p. 349-360.
- Ercan T, Fujitani T, Matsuda JI, Tokel S, Notsu K, Ul T, Can B, Selvi Y, Yıldırım, T, Fisekei A, Ölmez M, Akbaşlı A. The origin and evolution of the Cenozoic volcanism of Hasandağı Karacadağ area (Central Anatolia). *Jeomorfoloji Dergisi* 1990.p. 39- 54.
- Türel TK. Geology, Petrology and Geochemistry of Ekecikdağ Plutonic Rocks (Aksaray Region-Central Anatolia). ODTÜ, Doktora tezi;1991.
- Güleç N. Rb-Sr isotope data from the Ağaçören granitoid (East of Tuz Gölü): Geochronological and genetical implications, Tr. J. of Earth Sciences. 1994. p. 39-43.
- Güleç N, and Kadioğlu YK. Relative Involvement of Mantle and Crustal Components in the Ağaçören Granitoid (Central Anatolia-Turkey): Estimates from Trace Element and Sr-Isotope Data. *Chemie der Erde*. 1998. p. 23-37.
- Göncüoğlu MC, Dirik K, Eriş A, Yalınız K, Özgül L, Çemen İ. Tuzgölü havzası batı kısmının temel jeolojik sorunları TPAO Rapor No: 3753;1996.
- Güllü B, Yıldız M. Mamasun (Aksaray) Gabroyidlerinin Petrojenetik Karakteristiği, KSÜ Mühendislik Bilimleri Dergisi. 2012. p.28-42.
- Şaroğlu F, Emre Ö, Boray A. Türkiye Diri Fayları ve Depremsellikleri, Maden Tetkik ve Arama Genel Müdürlüğü Jeoloji Etütleri Dairesi,Rapor No:8174; 1987.
- Dirik K, Göncüoğlu MC. Neotectonic characteristics of Central Anatolia, *International Geology Review*. 1996. p. 807-817.
- Koçyiğit A, Beyhan A. A new intracontinental transcurrent structure; the Central Anatolian Fault Zone, Turkey. *Tectonophysics*. 1998. p. 317-336.
- Koçyiğit A. Orta Anadolunun Sismisitesi ve Neotektonik Özellikleri, Türkiye Petrol Jeologları Derneği, Özel Sayı. 2003. p. 1-26.
- Koçyiğit A., Özacar, A. Extensional neotectonic regime through the NE edge of the Outer Isparta Angle, SW Turkey: New Field and Seismic Data, *Turkish Journal of Earth Sciences*. 2003;12: 67-90.
- Şaroğlu F, Emre Ö, Boray A. Türkiye Diri Fay Haritası, Maden Tetkik Arama Genel Müdürlüğü.1992.
- Emre Ö. Hasandağı-Keçiboyduran dağı yöresi volkanizmasının jeomorfolojisi, Tuz Gölü Fay Zonunun Neotektonik Özellikleri, İstanbul Üniversitesi, Deniz bilimleri ve Coğrafya Enstitüsü Doktora tezi; 1991.
- Koçyiğit A. General neotectonic characteristics and seismicity of Central Anatolia, Haymana-Tuzgölü-Ulukışla basenlerinin uygulamalı çalışması (workshop). Abstracts. 2000. p. 1-26.
- Kürçer A. Tuz Gölü Fay Zonu'nun Neotektonik Özellikleri ve Paleosismolojisi, Orta Anadolu, Türkiye, Ankara Üniversitesi, Fen Bilimleri Enstitüsü Doktora Tezi; 2012.
- Kürçer A, Gökten YE. Paleosismolojik Üç Boyutlu Sanal Fotoğraflama Yöntemi, Örnek Çalışma: Duru-2011 Hendeği, Tuz Gölü Fay Zonu, Orta Anadolu, Türkiye. *Türkiye Jeoloji Bülteni*. 2014 Jan 57(1):45-72.

32. Sari, M., Seren, A., Alemdag, S. Determination of geological structures by geophysical and geotechnical techniques in Kırklartepe Dam Site (Turkey). *Journal of Applied Geophysics*. 2020;182:104174.
33. Sari, M. Geophysical and numerical approaches to solving the mechanisms of landslides triggered by earthquakes: A case study of Kahramanmaraş (6 February, 2023). *Engineering Science and Technology*. 2024;55:101758.
34. Öztürk, S., Beker, Y., Sari, M., Pehlivan, L. Estimation of ground types in different districts of Gümüşhane province based on the ambient vibrations H/V measurements. *Sigma Journal of Engineering and Natural Sciences*. 2021;39(4):374-391.
35. Junaid, M., Abdullah, R. A., Saari, R., Ali, W., Islam, A., Sari, M. 3D modelling and feasibility assessment of granite deposit using 2D electrical resistivity tomography, borehole, and unmanned aerial vehicle survey. *Journal of Mining and Environment*. 2022; 13(4):929-942.
36. Shirazi A, Hezarkhani A, Pour AB. Fusion of lineament factor (Lf) map analysis and multifractal technique for massive sulfide copper exploration: The Sahlabad area, East Iran. *Minerals*. 2022;12(5):549.
37. Nouri R, Arian M. Multifractal modelling of gold mineralization and lineaments in the 1: 100,000 Chaapaan sheet (NW IRAN). *Journal of Mining and Environment*. 2023. p. 973-980.
38. Sassioui S, Lakhloufi A, Arab A, Zouggarh A, El Hilali M, Courba S, Larabi A. Contribution of Remote Sensing to the Mapping of Lineaments and Ore-Mineral Occurrences in the Taghbalt Region, Moroccan Eastern Anti-Atlas. *The Iraqi Geological Journal*. 2023. p. 307-323.
39. Dutra LF, Louro VHA, Monteiro LVS. The southern IOCG and hydrothermal nickel mineralization trend of the Carajás Mineral Province: Airborne geophysical and remote sensing evidence for structural controls and hydrothermal signature. *Journal of Applied Geophysics*. 2023;213:105016.
40. Arrofi D, Abu-Mahfouz IS, Prayudi SD. Investigating high permeable zones in non- volcanic geothermal systems using lineament analysis and fault fracture density (FFD): northern Konawe Regency, Indonesia. *Geothermal Energy*. 2022. p. 1-17.
41. Heriawan MN, Hafizsyah RA, Hanunah JS, Hede ANH, Malik D. Surface and Subsurface Fracture Zones Modeling Using Automatic Lineament Analysis and Geostatistical Method, with Case Study of Wayang Windu Geothermal Field, West Java, Indonesia. In *IOP Conference Series: Earth and Environmental Science*. IOP Publishing; 2020.
42. Solomon S, Ghebream W. Lineament characterization and their tectonic significance using Landsat TM data and field studies in the central highlands of Eritrea. *Journal of African Earth Sciences*. 2006. p. 371-378.
43. Benaafi M, Hariri M, Abdullatif O, Makkawi M, Al-Shaibani A. Analysis of lineaments within the Wajid Group, SW Saudi Arabia, and their tectonic significance. *Arabian Journal of Geosciences*. 2017. p. 1-17.
44. Akram MS, Mirza K, Zeeshan M, Ali I. Correlation of tectonics with geologic lineaments interpreted from remote sensing data for Kandiah Valley, Khyber-Pakhtunkhwa, Pakistan. *Journal of the Geological Society of India* 2019. p. 607-613.
45. Baruah MP, Goswami TK, Bezbaruah D. Understanding the tectonics of the Mikir massif, northeast India: insights from lineament analysis. *Arabian Journal of Geosciences*. 2023;16(10):545.
46. Seymen İ. Kaman (Kırşehir) dolayında Kırşehir Masifi'nin stratigrafisi ve metamorfizması. *Türkiye Jeoloji Kurumu Bülteni*. 1981. p. 7-14.
47. Göçmez G. Aksaray Sıcak ve Mineralli Su Kaynaklarının Hidrojeolojik İncelemesi, Aksaray Valiliği, Yeni Aksaray Ofset Tesisleri, Aksaray.1997.
48. Envi, ENVI, Harris Geospatial Solutions; 2018.
49. Esri, USA; 2020.
50. Geomatica, PCI Geomatics, Canada; 2018.
51. Rockwork (RockWare Inc., Golden, USA; 2019.
52. Stereonet, W. Allmendinger; 2016.
53. Sedrette S, Rebai N. Automatic extraction of lineaments from Landsat Etm+ images and their structural interpretation: Case Study in Nefza region (North West of Tunisia). *Journal of Research in Environmental and Earth Sciences*. 2016. p. 139-145.

HITTITE JOURNAL OF SCIENCE AND ENGINEERING

e-ISSN: 2148-4171
Volume: 11 • Number: 3
September 2024

Assessment of Human Sperm Kinematic Parameters Using Computer-Assisted Semen Analysis

Nazlı Irmak Karaark  | Huseyin Kurtuldu* 

Başkent University, Department of Biomedical Engineering, 06790, Ankara, Türkiye

Corresponding Author

Huseyin Kurtuldu

E-mail: hkurtuldu@baskent.edu.tr Phone: +90 541 571 3194

RORID: <https://ror.org/02v9bqx10>

Article Information

Article Type: Research Article

Doi: <https://doi.org/10.17350/HJSE19030000340>

Received: 09.08.2022

Accepted: 29.08.2024

Published: 30.09.2024

Cite As

Karaark, N. I. & Kurtuldu, H. Assessment of Human Sperm Kinematic Parameters Using Computer-Assisted Semen Analysis. Hittite J Sci Eng. 2024;11(3):131-137.

Peer Review: Evaluated by independent reviewers working in at least two different institutions appointed by the field editor.

Ethical Statement: Not available.

Plagiarism Checks: Yes - iThenticate

Conflict of Interest: The author declares that there is no conflicts of interest concerning the content of this article

CRedit AUTHOR STATEMENT

Huseyin Kurtuldu: Conception, Design, Supervision, Providing, Materials, Data Collection or Processing, Analysis or Interpretation, Article Writing, Critical Review. **Nazlı Irmak Karaark:** Conception, Design, Supervision, Materials, Data Collection or Processing, Analysis or Interpretation, Literature Review, Article Writing, Critical Review.

Copyright & License: Authors publishing with the journal retain the copyright of their work licensed under CC BY-NC 4.

Assessment of Human Sperm Kinematic Parameters Using Computer-Assisted Semen Analysis

Nazlı Irmak Karaark | Huseyin Kurtuldu*

Başkent University, Department of Biomedical Engineering, 06790, Ankara, Türkiye

Abstract

Infertility affects approximately 15% of couples trying to conceive, as reported by the World Health Organization. It is diagnosed when conception does not occur despite unprotected intercourse over the course of at least one year. The spermogram test is a fundamental tool for identifying whether infertility originates from the male or female partner. Traditionally, sperm analysis is performed manually in reproductive clinics and laboratories, which may lead to variability in results due to subjective technician evaluations. Recent advancements have introduced computer-assisted systems with image processing capabilities to enhance sperm quality analysis. This study presents a novel computer-assisted sperm analysis (CASA) system designed to evaluate sperm motility through digital micrographs, utilizing 14 distinct kinematic parameters. The algorithms and parameters developed offer a quantitative approach to characterizing infertility.

Keywords: CASA, sperm analysis, kinematics, infertility, spermogram, semen

INTRODUCTION

Infertility is defined as the inability of couples to conceive after one year of unprotected intercourse [1]. Factors such as poor diet, stress, insomnia, smoking, and alcohol consumption can impair reproductive health, contributing to infertility. According to the World Health Organization (WHO), approximately 15% of couples seeking to conceive are affected by infertility [2]. With male reproductive issues accounting for about 50% of infertility cases [1], assessing male reproductive health is crucial in infertility diagnostics. Basic indicators of male fertility include the percentage of motile sperm and their velocity. Conventional sperm analysis, performed microscopically in clinical settings, often suffers from variability due to subjective evaluation [3]. Consequently, there is a need for fully automated systems that provide objective, standardized results.

Sperm imaging and motility studies have evolved over the past 300 years. Recent advancements focus on high-accuracy imaging techniques to improve treatment methods for reproductive disorders. The development of computer-assisted sperm analysis (CASA) began in the 1950s, enhancing classical microscopic imaging techniques. The introduction of phase contrast microscopy in andrology studies allowed better detection of sperm viability [4]. Automated sperm analysis methods date back to the early 1970s [4], with Katz et al. [5] pioneering the first CASA system in 1985, which assessed sperm motility from sequential microscopic images.

Abbiramy et al. [6] developed an algorithm in 2010 that could detect, count, and track sperm cells in video streams, achieving a 93% accuracy in tracking. Leung et al. [7] introduced algorithms to monitor sperm tail movement, improving Euclidean distance calculations. Ravanfar and Moradi [8] utilized Watershed segmentation and particle filter algorithms to address challenges in sperm tracking due to their similar size and shape. Di Caprio et al. [9] analyzed sperm motility by solving focal amplitude and phase maps from holographic images. Elsayed et al. [10] enhanced CASA systems in 2015 for better sperm detection in microfluidic systems using low-frame-rate cameras. Urbano et al. [11] employed the joint probabilistic data association filter in 2016 to simultaneously detect sperm movement and measure parameters without sample dilution. Boumazza and Loukil [12] developed an algorithm that enhances sperm analysis

by improving image quality and using hybrid segmentation techniques. Their method shows promising results for measuring sperm concentration and motility compared to traditional methods. Hernández-Ferrándiz, Pantrigo, and Cabido [13] introduced a method using synthetic semen samples to address the lack of labeled data in sperm analysis. Their approach demonstrates that models trained on synthetic data can be effectively applied to real images without additional fine-tuning.

This study introduces a CASA system incorporating sperm detection and tracking algorithms to provide quantitative measurements of human sperm kinematic parameters. The system was tested using samples from an 18-year-old subject, enabling numerical evaluation of male infertility and comparison with WHO and other institutional reference values.

MATERIAL AND METHODS

The study, approved by the Ankara City Hospital No. 2 Clinical Research Ethics Committee (Protocol No. E2-21-930) on October 13, 2021, utilized a sample obtained from the Andrology-Urology Clinic of Ankara City Hospital. The sample, from an 18-year-old subject referred to as Subject A, was a gray opaque, homogeneously distributed fluid with a volume of 3 ml and a pH of 7.5.

A 50 μm thick double-sided tape was placed between a microscope slide and coverslip, allowing sperm cells to move freely within a 50 μm depth. Sperm images were captured using a 2-megapixel camera mounted on an Olympus CX21 microscope at 10X magnification [14], covering a measurement area of 165.054 μm^2 and a volume of 8.252.749 μm^3 . Four series of images were captured at three-minute intervals, with each dataset comprising 130 images recorded at 30 fps, resulting in a measurement time of 4.3 seconds per set. To address local pixel density variations due to inhomogeneous illumination, background images were generated by averaging 130 images per set and subtracted from each individual image. Figure 1 illustrates background-subtracted images taken at 0.5-second intervals.

Each image was first converted to grayscale and then to binary using the Otsu method [16] for automatic thresholding

to distinguish sperm cells from the background. The contours of sperm heads were identified using the Python OpenCV library, which implements border-following algorithms for the topological analysis of digitized binary images [17]. These algorithms determine the surroundness relations among the borders of a binary image and can be effectively used in component counting, shrinking, and topological structural analysis. The algorithms facilitated the accurate identification of sperm head contours by following the outermost borders, ensuring precise detection of the sperm cells. The center positions of the sperm heads were determined by averaging the x and y coordinates of the contours. Figure 2 illustrates the detected sperm cells, with their centers marked in blue and contours in red.

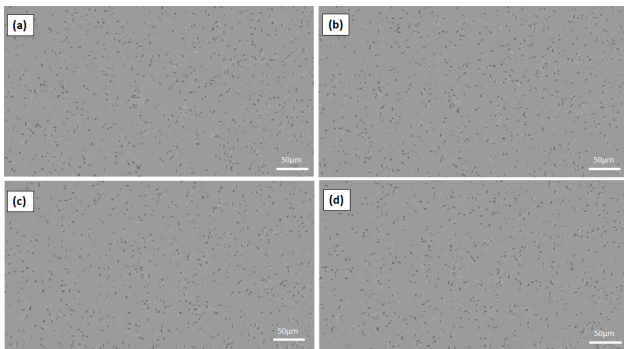


Figure 1 Background subtracted images taken at 0.5 second intervals at 10X magnification. (a) 0.5 sec, (b) 1.0 sec, (c) 1.5 sec, (d) 2.0 sec.

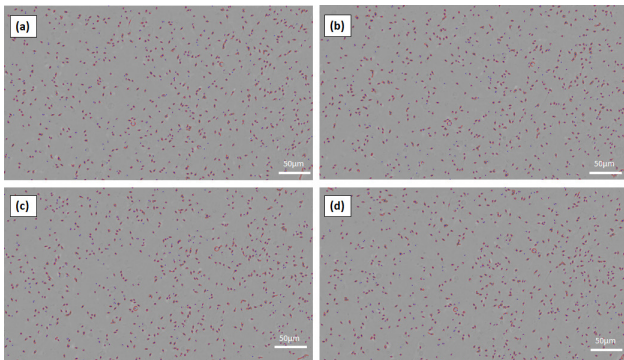


Figure 2 Sperms detected at 0.5 second intervals at 10X magnification. The centers of the sperms are shown as blue dots and the head region is shown as red lines. (a) 0.5 sec, (b) 1.0 sec, (c) 1.5 sec, (d) 2.0 sec.

Sperm traces in consecutive images were obtained by tracking center points assigned according to different acquisition times [15]. Figure 3 illustrates the tracking process on three consecutive images (j, j+1, j+2). At time j, the center position of a sperm cell is detected. This position is then compared with all sperm centers in the j+1 frame, and the closest match is recorded as the new center of that sperm in the j+1 image. This process is repeated for each sperm detected in the j image. Similarly, the process is carried out between images j+1 and j+2, and across other consecutive images to calculate the trajectory of each sperm head over time. In Figure 3,

the tracking process is depicted for sperm cells detected in equal numbers across consecutive images. However, if fewer sperm cells are detected in the subsequent image, it indicates that M sperm tracks were terminated in the previous image. Conversely, if more sperm cells are detected in the next image, it suggests that M new sperm tracks were initiated. Consequently, the initial and final frames of sperm traces may differ, leading to variations in track lengths among sperm.

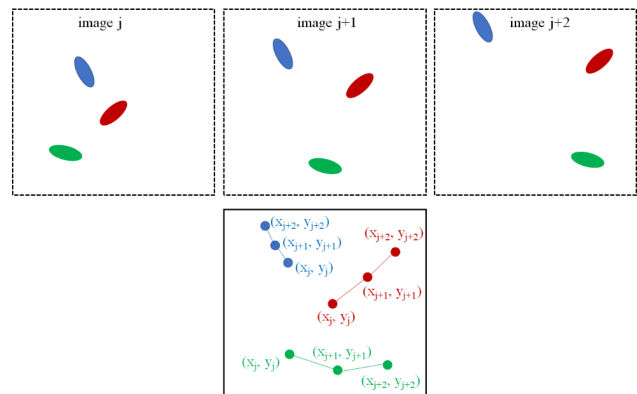


Figure 3 Sperm track illustration using sperm center points on 3 consecutive images.

In Figure 4, sperm tracks at different times are displayed in different colors, with traces of the same sperm coded with the same color. It is evident that some tracks continued across all images, while some traces were terminated, and new ones were created. For kinematic parameter measurements, only sperm tracks that were observed in at least 5 consecutive images were considered.

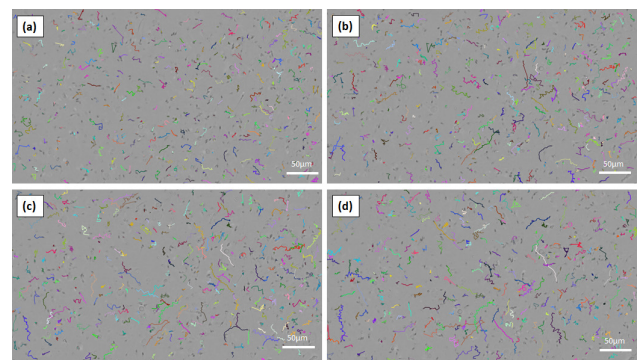


Figure 4 Tracks of sperms in different images at 10x magnification. Each sperm tracked is shown with a different color. (a) 0.5 sec, (b) 1.0 sec, (c) 1.5 sec, (d) 2.0 sec.

The metrics, developed in Python, measured six essential kinematic parameters [10]. The curvilinear velocity (VCL) of a sperm was calculated using the distance between center points of the cell in consecutive images. For instance, the VCL at position j, with coordinates (x_j, y_j) in image j and (x_{j+1}, y_{j+1}) in image j+1, is computed using Equation 1, where $\Delta t = 1/\text{fps}$ represents the time difference between consecutive images.

The linear velocity (VSL) was determined using the distance between the sperm's initial position (x_0, y_0) and final position (x_M, y_M) over time, as given by Equation 2. The average path velocity (VAP) was calculated using a moving average of the sperm's track with a value set to 5 frames (0.17 sec). For example, the VAP between averaged positions (x_j, y_j) in image j and (x_{j+1}, y_{j+1}) in image $j+1$ is given by Equation 3. The amplitude of lateral head (ALH) represents the amplitude difference between the VCL and VAP curves, with maximum and average ALH values calculated for each sperm. Beat cross frequency (BCF) was determined from the intersection points of the VCL and VAP curves, with the time difference between these points used in the analysis. The mean angular displacement (MAD) for each sperm in successive images was calculated using Equation 4. The VCL, VAP, BCF, and MAD values were computed for each sperm track, and their average values were recorded.

$$VCL_j = \frac{\sqrt{(x_{j+1} - x_j)^2 + (y_{j+1} - y_j)^2}}{\Delta t} \quad (1)$$

$$VSL = \frac{\sqrt{(x_M - x_0)^2 + (y_M - y_0)^2}}{\Delta t} \quad (2)$$

$$VAP_j = \frac{\sqrt{(x_{j+1} - x_j)^2 + (y_{j+1} - y_j)^2}}{\Delta t} \quad (3)$$

$$MAD_j = \cos^{-1} \left(\frac{x_j x_{j+1} + y_j y_{j+1}}{\sqrt{x_j^2 + y_j^2} \sqrt{x_{j+1}^2 + y_{j+1}^2}} \right) \quad (4)$$

Figure 5 shows examples of sperm tracks with different lengths in time. In the left column, black dots represent the positions of tracked sperm across different images, showing the VCL curve. The VAP curve, calculated by averaging VCL points, is shown with a red line. Blue dots indicate the starting and ending positions used for VSL analysis. In the right column, green dots mark the intersections of the VCL and VAP curves for BCF analysis, and the blue line indicates the maximum ALH distance between the VCL and VAP curves. These calculations were performed separately for each sperm track in four datasets.

The kinematic parameter LIN, which expresses the linearity of the curvilinear path, was determined by the percentage ratio of the mean VSL to VCL values. WOB, measuring the amount of wobbling in the sperm cell's movement path compared to the average path, was calculated by the ratio of VAP to VCL values. The STR parameter, reflecting the degree of straightness of the sperm's mean movement path, was calculated as the percentage ratio of VSL to VAP values. The motility parameter MOT was determined by the ratio of sperm with a mean VCL value greater than $5 \mu\text{m/s}$ to the total sperm count. The immobility parameter IM was calculated by the ratio of sperm with a velocity less than $5 \mu\text{m/s}$ to the total sperm count. Additionally, sperm with a VCL velocity greater than $25 \mu\text{m/s}$ were classified as progressive motility, while those with a velocity less than $25 \mu\text{m/s}$ were categorized

as non-progressive motility. The percentage of progressive sperm (PR) to total sperm count and the percentage of non-progressive sperm (NP) to total sperm count were calculated. Figure 6 summarizes the key stages in detecting and tracking sperm cells, from image acquisition to preprocessing, detection, tracking, and post-processing, highlighting the methods and techniques used at each step for precise analysis. Table 1 provides an overview of the parameters measured in the study, along with brief descriptions of each.

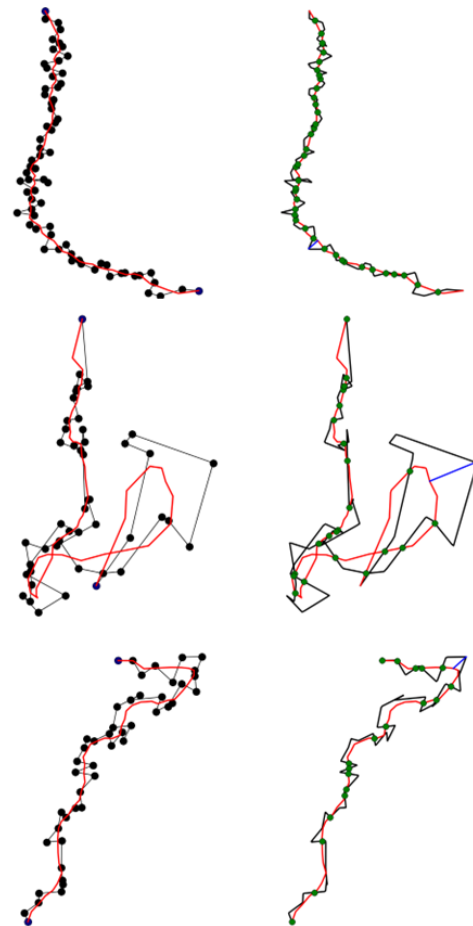


Figure 5 Examples of sperm tracks with different lengths.

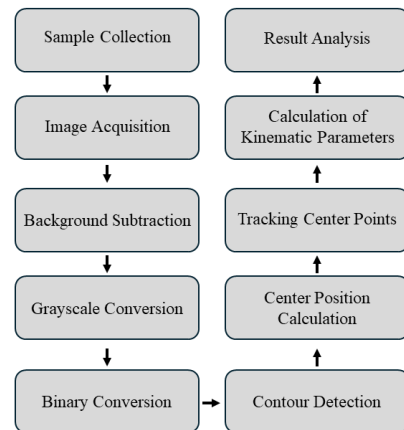


Figure 6 Workflow for detecting and tracking sperm cells.

Table 1 Summary of the parameters used in the study with brief descriptions.

Parameter	Description
VCL (Curvilinear Velocity)	Distance traveled by sperm between consecutive images.
VSL (Straight-Line Velocity)	Distance between the sperm's initial and final positions over time.
VAP (Average Path Velocity)	Moving average velocity along the sperm's track.
ALH (Amplitude of Lateral Head)	Amplitude difference between VCL and VAP curves.
BCF (Beat Cross Frequency)	Frequency of intersections between VCL and VAP curves.
MAD (Mean Angular Displacement)	Angular displacement of the sperm in successive images.
LIN (Linearity)	Ratio of VSL to VCL, indicating the straightness of the path.
WOB (Wobble)	Ratio of VAP to VCL, measuring the path wobble.
STR (Straightness)	Ratio of VSL to VAP, indicating the straightness of the average path.
MOT (Motility)	Ratio of sperm with VCL > 5 $\mu\text{m/s}$ to total sperm count.
IM (Immobility)	Ratio of sperm with VCL < 5 $\mu\text{m/s}$ to total sperm count.
PR (Progressive Motility)	Percentage of sperm with VCL > 25 $\mu\text{m/s}$.
NP (Non-Progressive Motility)	Percentage of sperm with VCL < 25 $\mu\text{m/s}$.

RESULTS AND DISCUSSION

Sperm count was calculated over approximately 4.3 seconds, with cells detected in 130 images per dataset. Figure 7(a) illustrates the variation in sperm count over time for the second dataset, demonstrating low variation around the mean value. Figure 7(b) shows the variation in sperm count per micrometer cubed over time, with red dashed lines indicating the mean value and green dashed lines representing WHO reference values. These analyses were repeated for each dataset, and the average sperm count, and sperm count per micrometer cubed were computed for four datasets captured three minutes apart. Table 2 presents the mean values for each dataset along with interquartile ranges (25th–75th percentile), indicating that 50% of the data falls within these ranges. The lowest average sperm count, and sperm count per cubic micrometer were 557 and 82.2×10^{-6} , respectively. The mean sperm count across all datasets was 609.1 ± 60.3 , and the sperm count per cubic micrometer was $89.9 \times 10^{-6} \pm 8.9 \times 10^{-6}$, which falls within the WHO reference values (15×10^6 – 259×10^6) [18].

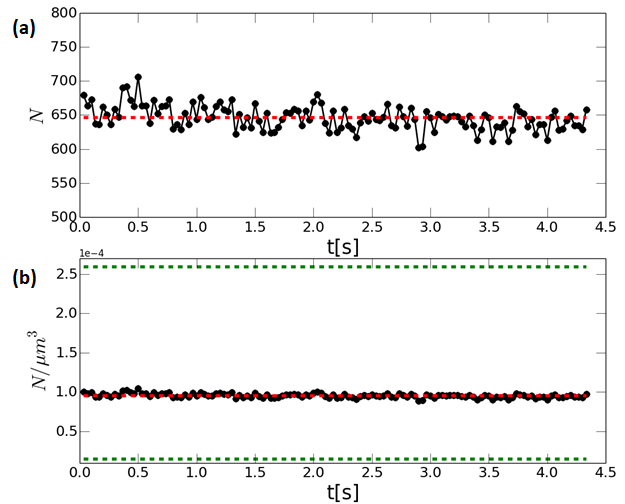


Figure 7 Average number of sperms in data set 2 and the number of sperms per micrometer cubed. The red dashed lines represent the mean value, and the green dashed lines represent the WHO reference limits.

Table 2 Average sperm count (N), and sperm count per cubic micrometer obtained in the four datasets. Values in parentheses indicate interquartile ranges (25th–75th percentile). The mean sperm count across all datasets is 609.1 (standard deviation 60.3), and the sperm count per cubic micrometer is 89.9×10^{-6} (standard deviation 8.9×10^{-6}).

DATA SET	N	$N/\mu\text{m}^3 \times 10^{-6}$
1	557.3 (547.0, 567.5)	82.2 (80.7, 83.8)
2	646.1 (634.5, 657.0)	95.4 (93.6, 97.0)
3	674.7 (662.5, 687.0)	99.6 (97.8, 101.4)
4	558.4 (535.5, 580.5)	82.4 (79.0, 85.7)

Table 3 presents the mean kinematic parameters obtained from all sperm in the four datasets. The total number of sperm tracked and analyzed ranged from 1178 to 1399. Values in parentheses represent interquartile ranges (25th and 75th percentiles). The VCL across all datasets was found to be greater than 70 $\mu\text{m/s}$, while the VAP and VSL values were greater than 45 $\mu\text{m/s}$ and 36 $\mu\text{m/s}$, respectively. As expected, VCL was greater than VAP, and VAP was greater than VSL. The average ALH was approximately 1 μm , with a maximum ALH around 3 μm . The BCF was approximately 15 Hz across all datasets. LIN was approximately 50% in all datasets, indicating sperm tracks were mostly straight. WOB was approximately 55% for all datasets, and STR values ranged from 63% to 75%. The motility (MOT) parameter was around 90%, indicating high sperm motility, while the immobility (IM) parameter was approximately 10%. Progressive motility (PR) was found to be 80%, and non-progressive motility (NP) was around 20%.

Table 3 Mean kinematic parameters for sperm from four datasets. Values in parentheses indicate interquartile ranges (25th-75th percentile).

DATASET	1	2	3	4
N	1254	1317	1399	1178
VCL [$\mu\text{m/s}$]	73.8 (46.0, 97.8)	72.7 (43.2, 97.8)	73.8 (47.5, 96.7)	76.3 (47.0, 103.2)
VAP [$\mu\text{m/s}$]	45.8 (26.2, 62.3)	45.6 (24.5, 63.5)	46.6 (27.0, 63.4)	49.5 (27.2, 68.3)
VSL [$\mu\text{m/s}$]	36.5 (16.5, 53.5)	36.1 (14.9, 53.5)	37.0 (16.3, 54.2)	40.4 (15.3, 60.2)
ALH max. [μm]	2.8 (1.6, 3.8)	2.9 (1.5, 3.8)	2.8 (1.7, 3.6)	2.8 (1.6, 3.8)
ALH mean [μm]	1.1 (0.6, 1.5)	1.0 (0.6, 1.4)	1.0 (0.6, 1.4)	1.0 (0.6, 1.4)
BCF [Hz]	15.2 (11.7, 18.4)	15.3 (12.0, 18.3)	15.3 (11.7, 18.5)	15.6 (12.5, 18.8)
MAD [$^\circ$]	30.2 (18.2, 39.0)	31.3 (18.4, 40.5)	31.0 (17.9, 39.7)	29.5 (17.5, 37.2)
LIN [%]	49.5	49.6	50.1	52.9
STR [%]	79.7	78.8	79.3	81.7
WOB [%]	62.1	63	63.2	64.8
MOT [%]	95.7	96.2	95.2	98.9
PR [%]	76.3	74.8	76.6	76.2
NP [%]	19.4	21.4	18.6	22.7
IM [%]	4.3	3.8	4.8	1.1

The mean kinematic parameters across all datasets are presented in Table 4. The standard deviation values indicate that the variation between datasets is low. It was estimated that $VCL = 1.58 \times VAP$ and $VAP = 1.25 \times VSL$, with VCL being approximately twice as great as VSL. This indicates that the wobbling is 63%, the straightness is 80%, and the linearity is around 50%. The maximum distance between the VCL and VAP curves is $2.8 \mu\text{m}$, while the average distance is $1 \mu\text{m}$. The BCF was approximately 15 Hz (fps/2), indicating that the VCL and VAP curves intersected every two frames. Additionally, sperm samples from Subject A, which exhibited high motility (96%), also showed a high progressive sperm count (76%).

Table 4 Mean and standard deviation of kinematic parameters from 4 data sets.

	MEAN	SD
VCL [$\mu\text{m/s}$]	74.2	1.5
VAP [$\mu\text{m/s}$]	46.9	1.8
VSL [$\mu\text{m/s}$]	37.5	2.0
ALH maks. [μm]	2.8	0.1
ALH ort. [μm]	1.0	0.1
BCF [Hz]	15.4	0.2
MAD [$^\circ$]	30.5	0.8
LIN [%]	50.5	1.6
STR [%]	79.9	1.3
WOB [%]	63.3	1.1
MOT [%]	96.5	1.7
PR [%]	76.0	0.8
NP [%]	24.0	0.8
IM [%]	3.5	1.7

Some of the measured parameters in this study were compared with those previously reported for human sperm in the literature. Notably, no study has been found that reports all 14 parameters simultaneously. Table 5 demonstrates that the VCL, VAP, VSL, ALH, and BCF values from this study fall within the ranges found in the literature. We emphasize methodological differences and performance metrics rather than direct comparisons, given that the datasets are not identical.

Table 5 Comparison of some of the kinematic parameters measured in the study with values found in the literature.

	VCL	VAP	VSL	ALH max.	ALH mean	BCF
Current Study	74.2	46.9	37.5	2.8	1.0	15.4
Sloter et al. [14]	80.7	55.8	49.1	3.7	-	25.2
Kraemer et al. [19]	119	-	54	7.5	-	-
Di Caprio et al. [9]	69.5	67.7	22.4	-	-	-
Hirano et al. [20]	82.5	46.1	56.1	4	-	23.6
Akashi et al. [21]	57.4	-	-	-	1.4	10
Mortimer et al. [22]	83.5	-	-	3.8	2.4	-
Davis et al. [23]	52	-	32.3	2.99	-	-

CONCLUSION

This study introduces a novel CASA system capable of quantitatively evaluating human sperm kinematic parameters through digital image processing. The system's performance was validated against WHO reference values, demonstrating its potential for clinical application in male infertility diagnostics. Continued development and optimization of the system will further enhance its utility in reproductive health assessments.

The kinematic parameters reported in this study may provide quantitative evaluations for male infertility, although no definitive conclusions can be drawn about human infertility. It is also believed that the current system will contribute to the literature by examining parameters that affect reproduction positively or negatively. In such studies, the number and motility of human sperm, directly impacting infertility, would be more accurately studied, allowing for comprehensive evaluation of the CASA method as a reliable diagnostic tool. Additionally, this technique could enable the diagnosis of specific diseases based solely on sperm kinematics in future disease-based studies. Future work will focus on enhancing the algorithms for real-time analysis and incorporating additional parameters for a comprehensive assessment of sperm quality.

Acknowledgement

The authors wish to thank Prof. Dr. Öner Odabaş for his assistance in patient sample collection and ethical approval.

References

- Erdemir F, Firat F, Gençten Y. The evaluation and clinical significance of sperm morphology. *Turk Urol Sem.* 2011 Jan;2:11-7.
- Cui W. Mother or nothing: the agony of infertility. *World Health Organization. Bulletin of the World Health Organization.* 2010 Dec 1;88(12):881.
- Gökçe A. Standard Semen Analysis Criteria of World Health Organization. *Turk Urol Sem.* 2011 Jan;2:1-7.
- Amann RP, Katz DF. Andrology lab corner*: Reflections on casa after 25 years. *Journal of andrology.* 2004 May 6;25(3):317-25.
- Katz DF, Davis RO, Delandmeter BA, Overstreet JW. Real-time analysis of sperm motion using automatic video image digitization. *Computer methods and programs in biomedicine.* 1985 Dec 1;21(3):173-82.
- Abbiramy VS, Shanthi V, Allidurai C. Spermatozoa detection, counting and tracking in video streams to detect asthenozoospermia. In 2010 International Conference on Signal and Image Processing 2010 Dec 15 (pp. 265-270). IEEE.
- Leung C, Lu Z, Esfandiari N, Casper RF, Sun Y. Detection and tracking of low contrast human sperm tail. In 2010 IEEE International Conference on Automation Science and Engineering 2010 Aug 21 (pp. 263-268). IEEE.
- Ravanfar MR, Moradi MH. Low contrast sperm detection and tracking by watershed algorithm and particle filter. In 2011 18th Iranian Conference of Biomedical Engineering (ICBME) 2011 Dec 14 (pp. 260-263). IEEE.
- Di Caprio G, El Mallahi A, Ferraro P, Dale R, Coppola G, Dale B, Coppola G, Dubois F. 4D tracking of clinical seminal samples for quantitative characterization of motility parameters. *Biomedical optics express.* 2014 Mar 1;5(3):690-700.
- Elsayed M, El-Sherry TM, Abdelgawad M. Development of computer-assisted sperm analysis plugin for analyzing sperm motion in microfluidic environments using Image-J. *Theriogenology.* 2015 Nov 1;84(8):1367-77.
- Urbano LF, Masson P, VerMilyea M, Kam M. Automatic tracking and motility analysis of human sperm in time-lapse images. *IEEE transactions on medical imaging.* 2016 Nov 18;36(3):792-801.
- Boumaza K, Loukil A. Computer-Assisted Analysis of Human Semen Concentration and Motility. *International Journal of E-Health and Medical Communications (IJEHMC).* 2020 Oct 1;11(4):17-33.
- Hernández-Ferrándiz D, Pantrigo JJ, Cabido R. SCASA: From synthetic to real computer-aided sperm analysis. In *International Work-Conference on the Interplay Between Natural and Artificial Computation 2022 May 24* (pp. 233-242). Cham: Springer International Publishing.
- Sloter E, Schmid TE, Marchetti F, Eskenazi B, Nath J, Wyrobek AJ. Quantitative effects of male age on sperm motion. *Human Reproduction.* 2006 Nov 1;21(11):2868-75.
- Chenouard N, Smal I, De Chaumont F, Maška M, Sbalzarini IF, Gong Y, Cardinale J, Carthel C, Coraluppi S, Winter M, Cohen AR. Objective comparison of particle tracking methods. *Nature methods.* 2014 Mar;11(3):281-9.
- Yousefi J. Image binarization using Otsu thresholding algorithm. Ontario, Canada: University of Guelph. 2011 Apr 18;10.
- Suzuki S. Topological structural analysis of digitized binary images by border following. *Computer vision, graphics, and image processing.* 1985 Apr 1;30(1):32-46.
- World Health Organization. WHO laboratory manual for the examination and processing of human semen. World Health Organization; 2010.
- Kraemer M, Fillion C, Martin-Pont B, Auger J. Factors influencing human sperm kinematic measurements by the Celltrak computer-assisted sperm analysis system. *Human reproduction (Oxford, England).* 1998 Mar 1;13(3):611-9.
- Hirano Y, Shibahara H, Shimada K, Yamanaka S, Suzuki T, Takamizawa S, Motoyama M, Suzuki M. Accuracy of sperm velocity assessment using the Sperm Quality Analyzer V. *Reproductive medicine and biology.* 2003 Dec;2:151-7.
- Akashi T, Watanabe A, Komiya A, Fuse H. Evaluation of the sperm motility analyzer system (SMAS) for the assessment of sperm quality in infertile men. *Systems biology in reproductive medicine.* 2010 Dec 1;56(6):473-7.
- Mortimer ST, Swan MA. Variable kinematics of capacitating human spermatozoa. *Human reproduction.* 1995 Dec 1;10(12):3178-82.
- Davis RO, Katz DF. Standardization and comparability of CASA instruments. *Journal of Andrology.* 1992 Jan 2;13(1):81-6.



HITIT
UNIVERSITY
PRESS